7

BEAM DYNAMICS

R. H. Helm, G. A. Loew, and W. K. H. Panofsky, Editor

This chapter deals with the general features of particle motion[1] through the standard sectors of the two-mile accelerator. The special problems associated with the injector and positron source are described in Chapters 8 and 16, respectively. The approach in this chapter is to identify those general features of particle motion which do not depend on details of design of the disk-loaded waveguide configuration. Emphasis is, therefore, placed on general formulation rather than detailed computation.

The first portion of the chapter deals with vacuum trajectories of single particles and thus ignores any effects that depend on beam intensity. The analysis is first made assuming no external focusing. Then the magnetic lens system now employed in the accelerator is taken into account. For this purpose the matrix formalism applying to beam transport problems is briefly reviewed; not only are orbits for the ideal accelerator derived, but the effects of misalignments and other perturbations are also studied.

The second part of the chapter deals with those phenomena resulting from the influence of the electron current upon individual particle behavior. The dominant item in this category is the beam breakup phenomenon which is discussed first in terms of a general asymptotic theory identifying the phenomena involved and is then examined through more detailed numerical computations. The chapter concludes with a summary of experimental observations taken to date on the beam breakup phenomena.

7-1 The "ideal" linear accelerator (WKHP)

Consider an ideal accelerator having cylindrical symmetry about the z axis. Let total differentiation with respect to z and referred to the moving electron be denoted by a prime ($'$); let γ be the energy of the electron in units of the rest energy m. Equating the velocity of light c to unity yields

$$\gamma' = \frac{eE_z}{m} \tag{7-1}$$

where E_z is the axial component of the electric field. In this chapter, $\beta = (1 - 1/\gamma^2)^{1/2}$ will be used for the velocity and the usual notation will be adopted for the components of electric and magnetic fields. It will be assumed that γ and γ' are given functions of z, resulting from the integration of Eq. (7-1) in a given accelerating field E_z.

The radial equation of motion is[2,3]

$$(\beta\gamma r')' = \frac{e(\mathbf{E} + \boldsymbol{\beta} \times \mathbf{B})_r}{m\beta} \tag{7-2}$$

In the absence of external focusing, the electric and magnetic terms in Eq. (7-2) almost cancel for a traveling-wave accelerator in which the phase velocity of the wave matches the particle velocity; in the relativistic limit ($\beta \approx 1$) the right-hand side of Eq. (7.2) becomes small. Thus in the usual description all radial forces are neglected and the integral of Eq. (7-2) becomes

$$r = r_0 + \theta_0(\beta\gamma)_0 \int_{z_0}^{z} \frac{dz}{\beta\gamma} \tag{7-3}$$

where θ_0 is the slope dr/dz at an arbitrary starting point and the subscript zero identifies the values of the other variables at that point. If the energy gain is uniform, $\gamma = \gamma' z$, where γ' is constant; furthermore if the energy is sufficient to make $\beta \approx 1$, Eq. (7-3) becomes

$$r = r_0 + (\theta_0 z_0) \ln \left(\frac{z}{z_0}\right) \tag{7-4}$$

where z_0 is defined by $\gamma' z_0 = \gamma_0$. These logarithmic orbits are a simple consequence of the transverse momentum being a constant while the longitudinal momentum increases linearly; such a momentum relationship implies $r' = \theta_0 z_0/z$ from which Eq. (7-4) follows. Equation (7-4) can be interpreted in terms of an "effective length" L given by

$$L = z_0 \ln \left(\frac{z}{z_0}\right) \tag{7-5}$$

which would be the length given by $r = r_0 + \theta_0 L$, i.e., the length over which a corresponding radial excursion in the absence of acceleration would occur (Fig. 7-1). The quantity L will also be recognized as the "contracted" length of the accelerator as seen from a frame of reference moving with the electron.

The right-hand side of Eq. (7-2) does not vanish exactly in the relativistic limit. To illustrate this, the "paraxial" equation will be formed, carrying terms linear in r only. With this approximation, the transverse field components can be expressed in terms of the longitudinal electric field as follows.

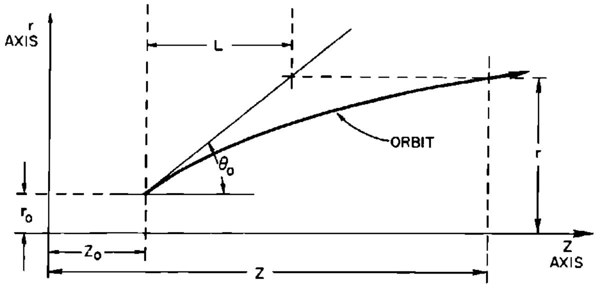

Figure 7-1 Orbit geometry.

In the absence of space-charge effects,

$$0 = \nabla \cdot \mathbf{E} = \frac{1}{r}\frac{\partial}{\partial r}(rE_r) + \frac{\partial E_z}{\partial z}$$

Therefore, remembering that E_z is circularly symmetric and thus has no first-order dependence on r, one obtains

$$-eE_r = \frac{er}{2}\frac{\partial E_z}{\partial z} = \frac{mr}{2}\frac{\partial \gamma'}{\partial z} \tag{7-6}$$

Similarly,

$$\frac{\partial E_z}{\partial t} = (\nabla \times \mathbf{B})_z = \frac{1}{r}\frac{\partial (rB_\phi)}{\partial r}$$

from which it follows that

$$eB_\phi = \frac{er}{2}\frac{\partial E_z}{\partial t} = \frac{mr}{2}\frac{\partial \gamma'}{\partial t} \tag{7-7}$$

Hence the general first-order paraxial equation of motions is*:

$$\begin{aligned}(\beta\gamma r')' &= -\frac{r}{2\beta}\left(\frac{\partial \gamma'}{\partial z} + \beta\frac{\partial \gamma'}{\partial t}\right) \\ &= -\frac{r}{2\beta}\left(\gamma'' - \beta^{-1}\gamma^{-2}\frac{\partial \gamma'}{\partial t}\right)\end{aligned} \tag{7-8}$$

since

$$\frac{d}{dz} \equiv {}' = \frac{\partial}{\partial z} + \frac{1}{\beta}\frac{\partial}{\partial t}$$

is the total derivative with respect to z. As γ becomes large the last term

---

* Note that $(\mathbf{E} + \boldsymbol{\beta} \times \mathbf{B})_\phi = 0$, i.e., the Lorentz force has no azimuthal component.

vanishes (corresponding to cancelation of electric and magnetic forces in the relativistitic limit); the differential equation then becomes, with $\beta = 1$,

$$(\gamma r')' + \frac{r}{2}\gamma'' = 0 = \left(\gamma r' + \frac{r}{2}\gamma'\right)' - \frac{r'\gamma'}{2} \tag{7-9}$$

Integrating from a point denoted by the subscript zero to a final point, where the initial point is assumed to be in field-free space, one finds

$$\gamma r' - (\gamma r')_0 = \frac{1}{2}\int_{r_0}^{r} \gamma'\, dr - \frac{r}{2}\gamma'$$

or

$$\gamma r' - (\gamma r')_0 = \tfrac{1}{2}\{-r_0\overline{\gamma'} + r(\overline{\gamma'} - \gamma')\} \tag{7-10}$$

where $\overline{\gamma'}$ is a mean value of the rate of energy gain γ'. Hence the radial momentum differs from being a constant of the motion by the two terms on the right-hand side of Eq. (7-10). The first term $-\frac{1}{2}r_0\overline{\gamma'}$ represents the converging lens effect at the beginning of the accelerating region. The effective thin-lens focal length f_0 at entry is simply

$$\frac{1}{f_0} = +\frac{1}{2}\frac{\overline{\gamma'}}{\gamma} \tag{7-11}$$

The second term gives an alternating focusing–defocusing action due to the fluctuations in γ' about the mean value of $\overline{\gamma'}$. The result is a net "strong focusing" action the strength of which can easily be computed by conventional strong focusing theory. Note that even if the term in $\overline{\gamma'} - \gamma'$ is negligible within the accelerator section, the exit fringe field still contributes a radial impulse $+\frac{1}{2}r\overline{\gamma'}$ and is thus equivalent to a diverging lens of focal length

$$\frac{1}{f} = -\frac{1}{2}\frac{\overline{\gamma'}}{\gamma} \tag{7-12}$$

Thus the field-free gaps between sections are equivalent to weak, alternating gradient doublets. These effects will not be analyzed further here, since the strength of the radial forces discussed in this section for the parameters of the SLAC accelerator is small compared with the action of the external lenses which will be discussed in the next section.

7-2 External focusing (RHH)

In real accelerators the transverse position and quality of the beam are affected by numerous small perturbations, such as stray magnetic fields, misalignments, RF asymmetry effects, scattering by residual gas, and in some cases a transverse instability ("beam breakup") resulting from electromagnetic interaction with the accelerator structure. In addition, the finite phase space volume of the injected beam imposes limits on the distance the beam can be transported before filling the entire radial aperture, even in an ideal accelerator.

External focusing is a practical means of containing the initial phase space which has the additional advantage of suppressing the various perturbing effects to a considerable extent. A major disadvantage arises from the beam deflection caused by misalignment of focusing lenses, which, therefore, must be aligned to very tight tolerances.

In the present section the principles of linac focusing are discussed, with special emphasis being given to problems affecting very long accelerators, and to the design of the focusing system for SLAC.

Phase space

The general definition of phase space volume which will be employed in this chapter is

$$U_6 = \iiiint\!\!\iint dx\, dp_x\, dy\, dp_y\, dt\, d\gamma \tag{7-13}$$

where (x, p_x), (y, p_y), and (t, γ) are the conjugate coordinate pairs appropriate to a Hamiltonian system in which the independent variable is the longitudinal coordinate, z, and in which there is no scalar potential.* According to Liouville's theorem, the coordinates of a given set of particles are contained in a volume which is invariant provided that only nondissipative forces act on the particles.

In beam transport (i.e., the motion of streams of charged particles through a complex accelerating, steering, and focusing system) it often happens that one or more components of the motion are decoupled from other motions, so that phase volumes are conserved in certain subspaces; e.g., the projected phase plane areas

$$u_x = \iint dx\, dp_x \qquad u_y = \iint dy\, dp_y \qquad u_t = \iint dt\, d\gamma \tag{7-14}$$

might each be conserved. Frequently the coupling between different components is weak enough to permit the use of perturbation calculations in which such subspace projections of the phase volume are conserved as a first approximation.

Because of the conservation, whether exact or approximate, the concept of phase space *emittance* of a beam source is useful as a figure of merit. For example, a small transverse emittance implies that the beam may be focused in such a way as to have simultaneously a moderate size and a very small transverse momentum, so that it may consequently be transmitted for long distances without further focusing. Small transverse emittance also implies

---

* If a scalar electric potential were present, the longitudinal canonical momentum could not be equated with the energy γ.

that the beam may be focused to very small size without excessive angular spread—a desirable property for allowing a small target size for physics experiments.

The concept of phase space is also useful in specifying the properties of a beam transport system. Here the *admittance*, the maximum phase space which can be transmitted through the system, serves as a figure of merit. Clearly, the emittance of the beam to be transmitted imposes a lower limit on the required transport system admittance.

The transverse emittance of the SLAC injector (described in Chapter 8) has been measured. It is found that 90% of the beam, in a projection of the phase volume on the x, p_x plane, is contained within an ellipse of area

$$u = 3.6\pi \times 10^{-3}\,(\text{MeV}/c)(\text{cm}) \tag{7-15}$$

To illustrate the effect of the initial phase space, suppose that the beam is injected as an erect ellipse in the x, p_x plane (solid curve in Fig. 7-2). Then if all transverse forces can be neglected, the transformation to a later point in the machine is given by

$$p_x = \text{constant} \qquad \text{and} \qquad x = x_0 + \zeta p_{x_0}$$

where

$$\zeta(z, z_0) = \int_{z_0}^{z} dz'/P(z') \tag{7-16}$$

and $P(z)$ is the longitudinal momentum.

It is then readily shown that the maximum size of the transformed ellipse is given by

$$x_{\max} = [(x_0)^2_{\max} + \zeta^2 (p_0)^2_{\max})]^{1/2} = \left((x_0)^2_{\max} + \zeta^2 \left[\frac{u}{\pi (x_0)_{\max}}\right]^2\right)^{1/2} \tag{7-17}$$

As an example, consider uniformly accelerated relativistic electrons, for which $P/m = \beta\gamma \cong \gamma$, $\gamma' = d\gamma/dz = \text{constant}$, and $\zeta = (1/m\gamma') \ln (\gamma/\gamma_0)$. Taking

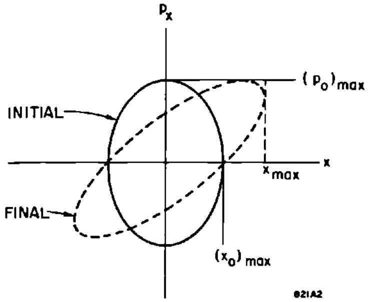

Figure 7-2 Injection of initial phase space as erect ellipse.

$my' = 0.06$ MeV/cm, $m\gamma_0 = 35$ MeV, $m\gamma = 18$ GeV, $u = 3.6\pi \times 10^{-3}$ (MeV/c)(cm), and the initial beam size $(x_0)_{\max} = 0.5$ cm, it is found from Eq. (7-17) that

$$x_{\max} = 0.81 \text{ cm}$$

On the other hand, if the beam were initially accelerated to 2 GeV and allowed to coast the rest of the way through the machine, the result would be

$$x_{\max} = 1.63 \text{ cm}$$

It is evident that very little focusing along the machine would suffice to contain the small emittance of the injector. However, the positron system (Chapter 16), with a design admittance of 0.15π (MeV/c)(cm), imposes a much stronger focusing requirement. Further, as will be seen, a rather large admittance is also desirable for transport of the normal electron beam because of the various perturbing effects.

Formulation of the ideal accelerator focusing and transport system

THE EQUATION OF MOTION. Consider first an ideal system in which there are no misalignments or other perturbing effects. It will be assumed that the x and y motions are decoupled, e.g., any focusing elements presumably would be magnetic quadrupoles of which the symmetry planes include the x and y axes. The first-order paraxial equation of motion for a typical transverse coordinate, x, is of the form

$$p_x' = (Px')' = xC(z) \tag{7-18}$$

where

$$C \approx 0 (\text{in a drift section or an accelerator section}) \tag{7.19}$$

or

$$C = e\frac{\partial B_y}{\partial x}\left(\text{in a quadrupole field of transverse gradient } \frac{\partial B_y}{\partial x}\right) \tag{7-20}$$

THE MATRIX FORMULATION.[4,5,6,7,8] Because the differential equation (7-18) is linear and homogeneous, its solution may always be written as a linear transformation

$$\begin{aligned} x(z) &= a_{11}(z)x_0 + a_{12}(z)p_{x_0} \\ p_x(z) &= a_{21}(z)x_0 + a_{22}(z)p_{x_0} \end{aligned} \tag{7-21}$$

or in matrix notation

$$\begin{bmatrix} x \\ p_x \end{bmatrix} = \begin{bmatrix} a_{11} & a_{12} \\ a_{21} & a_{22} \end{bmatrix} \begin{bmatrix} x_0 \\ p_{x0} \end{bmatrix} \tag{7-22}$$

which may be written schematically as

$$\mathbf{x} = \mathbf{A}\mathbf{x}_0 \tag{7-23}$$

The determinant of any transport matrix is unity; e.g., in the present 2 × 2 representation

$$|\mathbf{A}| = a_{11}a_{22} - a_{12}a_{21} = 1 \tag{7-24}$$

Combinations of transport elements then are generated by the usual rules of matrix multiplication.

THE PERIODIC SYSTEM. If the elements of a transport system repeat periodically, then

$$\mathbf{A}(n, 0) = \mathbf{A}^n \tag{7-25}$$

where $\mathbf{A}(n, m)$ is the transformation from the mth to the nth reference plane, and $\mathbf{A}$ is the transformation for one period. The resulting well-known eigenvector problem for a 2 × 2 matrix has the solution

$$\tilde{x}_n = \tilde{x}_0 e^{in\theta} \tag{7-26}$$

where the eigenvalues $e^{\pm i\theta}$ are given by*

$$\cos\theta = \tfrac{1}{2}(a_{11} + a_{22}) \tag{7-27}$$

and a suitable representation of the eigenvector, if θ is real, is

$$\tilde{x}_n = x_n - \frac{i}{\sin\theta}[\tfrac{1}{2}(a_{11} - a_{22})x_n + a_{12}p_{xn}] \tag{7-28}$$

The betatron phase shift is invariant under translation of the reference planes; in fact, for any nonsingular transformation $\mathbf{T}$ it is easy to show that the trace of the transformed matrix is conserved. Thus

$$b_{11} + b_{22} = a_{11} + a_{22} \tag{7-29}$$

where

$$\mathbf{B} = \mathbf{T}^{-1}\mathbf{A}\mathbf{T} \tag{7-30}$$

Two conclusions may be drawn from Eqs. (7-26) through (7-28): (1) The condition for stable orbits is that θ be real, i.e.,

$$\begin{aligned} |a_{11} + a_{22}| &< 2 \text{ means stable orbits} \\ |a_{11} + a_{22}| &> 2 \text{ means divergent orbits} \end{aligned} \tag{7-31}$$

(2) The quantity

$$\begin{aligned} |\tilde{x}_0|^2 = |\tilde{x}_n|^2 &= x_n^2 + \frac{a_{12}^2}{\sin^2\theta}\left[p_{xn} + \frac{a_{11} - a_{22}}{2a_{12}}x_n\right]^2 \\ &= \frac{a_{12}}{\sin^2\theta}[-a_{21}x_n^2 + (a_{11} - a_{22})x_n p_{xn} + a_{12}p_{xn}^2] \end{aligned} \tag{7-32}$$

is invariant as a function of n.[9]

---

* In the accelerator literature, the parameter θ is commonly called the *betatron phase shift.*

Now in the case of stable orbits it is evident that the curve $|\tilde{x}_n|^2 =$ constant represents an ellipse in the (x_n, p_{xn}) phase plane. The area of this ellipse is[†]

$$u = \frac{\pi \sin\theta}{a_{12}} |\tilde{x}_n|^2 \tag{7-33}$$

From Liouville's theorem we conclude that the phase plane area u is invariant, so that

$$u = \frac{\pi \sin\theta}{a_{12}} |\tilde{x}|^2 = \frac{\pi}{\sin\theta} [-a_{21}x^2 + (a_{11} - a_{22})xp_x + a_{12}p_x^2] \tag{7-34}$$

may be considered to remain invariant under an arbitrary translation of the periodic reference planes.

The maximum amplitude of a given orbit is thus

$$x_{\max}^2 = \frac{a_{12}^*}{\sin\theta} \frac{u}{\pi} \tag{7-35}$$

where $|a_{12}^*|$ is the value of $|a_{12}|$ maximized with respect to translation of the reference planes. The admittance, U, of the periodic system is designated as the area of the maximum phase ellipse which can be transmitted through the defining aperture; e.g., in a system of constant aperture, a,

$$U = \pi a^2 \frac{\sin\theta}{a_{12}^*} \tag{7-36}$$

Physically, in a transport system consisting of lenses and drift spaces, the maximum orbit size always occurs in a converging lens.

ADIABATICALLY VARYING (ALMOST PERIODIC) SYSTEM. The next case to be considered is a repetitive transport system which is almost periodic in the sense that the matrix elements, dependent on parameters such as lens strengths, beam energy, and spacing of reference planes, vary slowly from period to period. Since the characteristic function u given by Eq. (7-34) is an invariant, the transformation

$$\mathrm{A}(n, 0) = \mathrm{A}(n, n-1)\mathrm{A}(n-1, n-2) \cdots \mathrm{A}(1, 0) \tag{7-37}$$

has an approximate eigenvector solution

$$\tilde{x}_n \cong \tilde{x}_0 \left(\frac{\sin\theta}{a_{12}}\right)_0^{1/2} \left(\frac{a_{12}}{\sin\theta}\right)_n^{1/2} e^{i\mu_n} \tag{7-38}$$

where

$$\mu_n = \sum_{m=1}^{n} \theta_m$$

and θ_n and $\tilde{x}_n$ are defined by Eqs. (7-27) and (7-28) but with the matrix elements now dependent upon the index n.

[†] The sign of $\sin\theta$ is defined to be the same as that of a_{12}.

The function u defined by Eq. (7-34) now becomes an adiabatic invariant. The local maximum orbit size is given by Eq. (7-35). The admittance of the system is defined by

$$U = \pi \left(\frac{a^2 \sin \theta}{a_{12}} \right)_{\min} \tag{7-39}$$

where the minimum value which the function takes anywhere in the system is to be used.

The beam is said to be *optically matched* to the transport system if the beam phase space distribution is matched as nearly as possible to the characteristic admittance ellipse, Eq. (7-34). The transverse fluctuations in beam size then are minimized. The adiabatic invariance of the characteristic admittance ellipse implies that a beam which is initially optically matched to the system will remain matched through an adiabatically varying system.

TYPICAL TRANSPORT ELEMENTS.[10,11] The accelerator transport system elements are accelerator sections and drift sections containing magnetic quadrupoles. In the representation being used, the dynamic vectors are

$$\mathbf{x} = \begin{bmatrix} x \\ p_x \end{bmatrix} \quad \text{and} \quad \mathbf{y} = \begin{bmatrix} y \\ p_y \end{bmatrix} \tag{7-40}$$

Transfer matrices for these basic transport elements will now be given.

DRIFT AND ACCELERATOR SECTIONS. To the approximation that radial forces may be neglected, the transformation from z_1 to z_2 is

$$\begin{bmatrix} 1 & \zeta \\ 0 & 1 \end{bmatrix} \tag{7-41}$$

where ζ is given by Eq. (7-16), i.e.,

$$\zeta = \frac{1}{m\gamma'} \ln \frac{\gamma_2}{\gamma_1} \tag{7-42a}$$

for relativistic electrons accelerated by a uniform energy gradient, and

$$\zeta = \frac{z_2 - z_1}{P} \cong \frac{z_2 - z_1}{m\gamma} \tag{7-42b}$$

for electrons at constant energy.

QUADRUPOLES.[1,12,13] The following definitions are needed:

$$\left.\begin{aligned} &Z = \text{effective length of quadrupole field} \\ &Q = \text{“quadrupole strength”} = e \int \frac{\partial B_y}{\partial x}\, dz \\ &k = \left(\frac{e}{P} \frac{\partial B_y}{\partial x} \right)^{1/2} \end{aligned}\right\} \tag{7-43}$$

The appropriate transformations through the quadrupole are

$$\begin{bmatrix} \cos kZ & \dfrac{\sin kZ}{kP} \\ -kP\sin kZ & \cos kZ \end{bmatrix} \quad \text{(in the focusing plane)} \qquad (7\text{-}44a)$$

and

$$\begin{bmatrix} \cosh kZ & \dfrac{\sinh kZ}{kP} \\ kP\sinh kZ & \cosh kZ \end{bmatrix} \quad \text{(in the defocusing plane)} \qquad (7\text{-}44b)$$

If small-angle expansions ($kZ \ll 1$) are used, the matrix corresponding to two equal drift spaces and one "thin" lens may be written as the product of three matrices, as follows:

$$\begin{bmatrix} 1 & \zeta_2 \\ 0 & 1 \end{bmatrix} \begin{bmatrix} 1 & 0 \\ -P/f & 1 \end{bmatrix} \begin{bmatrix} 1 & \zeta_1 \\ 0 & 1 \end{bmatrix} \qquad (7\text{-}44c)$$

where

$$\zeta_1 = \zeta_2 = \frac{1}{2}\frac{Z}{P}\left(1 + \frac{QZ}{12P}\cdots\right) \qquad (7\text{-}45)$$

and

$$\frac{P}{f} = Q\left(1 - \frac{QZ}{6P}\cdots\right) \qquad (7\text{-}46)$$

with the understanding that $Q > 0$ in the focusing plane and $Q < 0$ in the defocusing plane. In the present discussion it will turn out that the expansion parameter, $QZ/P \approx Z/f$, is always small and the quadrupole is optically equivalent to a thin lens at its geometric center.

IDEAL PROPERTIES OF ALTERNATIVE ACCELERATOR TRANSPORT SYSTEMS. Three different systems have been analyzed for magnetic focusing in the accelerator at SLAC: (1) the *alternating singlet* system, consisting of alternating gradient quadrupole singlets at the beginning of each 40-ft girder; (2) the *sector doublet* system, a quadrupole doublet in each of the drift sections* at the ends of the 333$\frac{1}{3}$-ft sectors; (3) the *sector triplet* system, a quadrupole triplet in each drift section.

Two variations of each of the sector focusing schemes were studied, one in which the quadrupoles of the multiplet were spread as far apart as possible in the 10-ft drift section and one in which the quadrupoles were placed essentially end-to-end. The latter alternative proved undesirable† not only

---

* See "The 10-ft Girder Components" under Section 7-3.

† An exception occurs in the positron transport system (Chapter 16) where a number of compact multiplets are used in matching the large phase space of the positron beam into the standard accelerator focusing system.

because of greater quadrupole power requirements but also because of tighter alignment tolerances. Consequently, only the widely spaced doublet and triplet cases will be considered here.

ALTERNATING SINGLETS. The basic section is shown in Fig. 7-3. In this discussion, the quadrupoles are treated as thin lenses and the reference planes are placed just ahead* of them. The two types of quadrupoles are assumed to have the same strengths and to be equally spaced along the machine. The relative energy change is assumed to be small so that a parameter l can be defined such that

$$l \cong \int_{z_1}^{z_1+L} \frac{dz}{P} \cong \int_{z_1+L}^{z_2} \frac{dz}{P} \cong \frac{L}{P} \cong \frac{L}{m\gamma} \tag{7-47}$$

The transfer matrix for one section is

$$\mathbf{A} = \begin{bmatrix} 1 & l \\ 0 & 1 \end{bmatrix} \begin{bmatrix} 1 & 0 \\ Q & 1 \end{bmatrix} \begin{bmatrix} 1 & l \\ 0 & 1 \end{bmatrix} \begin{bmatrix} 1 & 0 \\ -Q & 1 \end{bmatrix} \tag{7-48}$$

$$= \begin{bmatrix} 1 - Ql - Q^2 l^2 & 2l(1 + \frac{1}{2}Ql) \\ -Q^2 l & 1 + Ql \end{bmatrix} \tag{7-49}$$

where the quadrupole strength Q is defined by Eq. (7-43). The betatron phase shift, by Eq. (7-27), is

$$\cos \theta = 1 - \tfrac{1}{2} Q^2 l^2 \tag{7-50}$$

It may be shown that the present choice of reference planes maximizes the a_{12} matrix element. [Refer to Eq. (7-22).] Therefore, if the amplitude is limited by the system aperture to a value a, the admittance of the system as defined in Eq. (7-39) is given by

$$U = \frac{\pi}{2} Q a^2 \left(\frac{1 - \frac{1}{2}Ql}{1 + \frac{1}{2}Ql} \right)^{1/2} \tag{7-51}$$

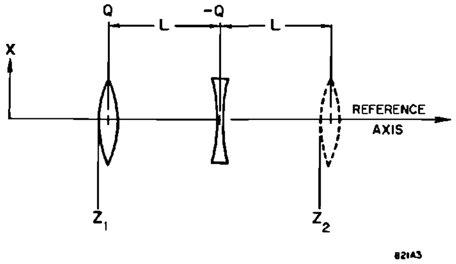

Figure 7-3 Typical period of alternating singlet system.

---

* The expression "just ahead," as used here and subsequently, should be interpreted to mean at the beginning of the effective length Z [see Eq. (7-43)], i.e., "squaring off" the fringing field.

The admittance as a function of quadrupole strength for a fixed value of the spacing parameter l is maximized for $Ql = \sqrt{5} - 1$. Under this condition, the optimum admittance becomes

$$U_{\text{opt}} = 0.300 \frac{\pi a^2}{l} \tag{7-52}$$

and the betatron phase shift is

$$\theta_{\text{opt}} = \cos^{-1}(\sqrt{5} - 2) = 76.34^\circ \tag{7-53}$$

which implies a wavelength of 9.44 L.

A stop band occurs if $Ql \geq 2$, where the admittance and betatron phase shift become imaginary. Therefore, a *low-energy* cutoff occurs at

$$m\gamma_{\text{co}} \approx P_{\text{co}} \approx \tfrac{1}{2}QL \tag{7-54}$$

In the high-energy limit, $Ql \rightarrow 0$ and the asymptotic admittance U_∞ becomes, from Eq. (7-51)

$$U_\infty = \lim_{Ql \to 0} U = \frac{\pi}{2} Qa^2 \tag{7-55}$$

SECTOR DOUBLETS. Figure 7-4 shows the basic section in the plane of initial focusing (the x plane). The transfer matrix per sector in this case is

$$\mathbf{A} = \begin{bmatrix} 1 - Qd - Q^2\lambda\, d & \lambda + d + Q\lambda\, d \\ -Q^2\, d & 1 + Q\, d \end{bmatrix} \tag{7-56}$$

where

$$d = \frac{D}{P} \quad \text{and} \quad \lambda = \int_{z_1 + D}^{z_2} \frac{dz}{P} \approx \frac{\Lambda}{P} \tag{7-57}$$

As noted above, the present choice of reference planes maximizes the a_{12} matrix element. The matrix from z_1 to z_2 in the initially defocusing (y) plane results from Eq. (7-56) by changing the sign of Q. The maximum value of the

Figure 7-4 Typical period of sector doublet system; the period $(\Lambda + D)$ = total length of one sector.

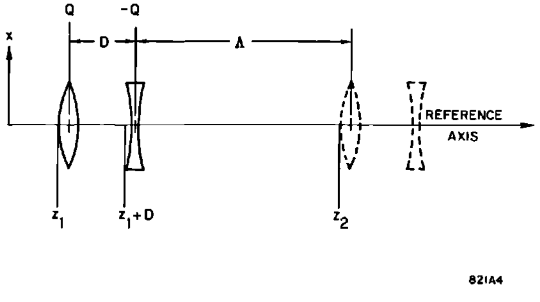

a_{12} matrix element is the same in the **y** plane as in the **x** plane, but occurs when the basic period is defined so that the doublet is located at the end of it rather than at the beginning. In either case, the sector doublet has the following properties:

Betatron phase angle,

$$\cos\theta = 1 - \tfrac{1}{2}Q^2\lambda\, d \tag{7-58}$$

Admittance,

$$U = \pi Q a^2 \frac{[(d/\lambda)(1 - \frac{1}{4}Q^2\lambda\, d)]^{1/2}}{1 + d/\lambda + Q\, d} \tag{7-59}$$

Low-energy cutoff,

$$(Q^2\lambda\, d)_{\mathrm{co}} = 4$$

or

$$m\gamma_{\mathrm{co}} \approx P_{\mathrm{co}} \approx \tfrac{1}{2}Q(\Lambda D)^{1/2} \tag{7-60}$$

Asymptotic admittance as $\gamma \to \infty$,

$$U_\infty = \frac{\pi Q a^2}{1 + D/\Lambda}\left(\frac{D}{\Lambda}\right)^{1/2} \tag{7-61}$$

If the doublet is treated as a thin lens, i.e., if

$$D \ll \Lambda \qquad \text{and} \qquad Qd \ll 1$$

the admittance is optimized with respect to quadrupole strength when $(Q^2\lambda\, d)_{\mathrm{opt}} \approx 2$. It follows that

$$\begin{aligned} U_{\mathrm{opt}} &\approx \frac{\pi a^2/\lambda}{1 + (2D/\Lambda)^{1/2}} \\ &\approx \pi Q a^2\left(\frac{D}{2\Lambda}\right)^{1/2} \cong \left(\frac{1}{2}\right)^{1/2} U_\infty \end{aligned} \tag{7-62}$$

and $\theta_{\mathrm{opt}} \approx \pi/2$ (betatron wavelength = 4 sectors).

SECTOR TRIPLETS. The sector triplet period is shown in Fig. 7-5 in the plane of initial focusing (the **x** plane). The transfer matrix is

$$\mathbf{A} = \begin{bmatrix} 1 - Q^2\lambda\, d\left(1 + \dfrac{1}{2}\dfrac{d}{\lambda} - \dfrac{1}{2}Q\, d\right) & \lambda + d + \frac{1}{2}Q\, d^2 - \frac{1}{2}Q^2\lambda\, d^2 \\ -Q^2\, d(1 - \frac{1}{2}Q\, d) & 1 - \frac{1}{2}Q^2\, d^2 \end{bmatrix} \tag{7-63}$$

where λ and d are defined as in the doublet case. The reference planes have again been chosen to maximize the a_{12} matrix element.

In the **y** plane (initially defocusing), the orbit maxima would occur at the center of the triplet rather than at the ends; however, in the present application, it is assumed that the quadrupole has sufficiently larger aperture than

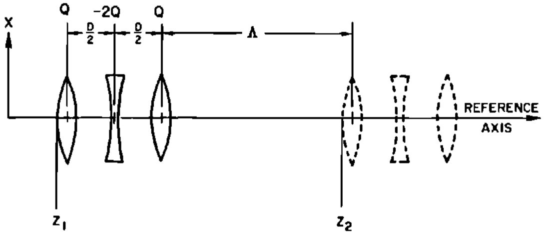

821A5

Figure 7-5 Typical period of sector triplet system; the period $(\Lambda + D)$ = total length of one sector.

the accelerator so that the ends of the triplet essentially define the limiting aperture. Hence, the above matrix with reversed sign of the quadrupole strength Q is appropriate for calculating the y plane properties.

The properties of the sector triplet are

Betatron phase shift,

$$\cos \theta_{x,y} = 1 - \frac{1}{2} Q^2 \lambda\, d \left(1 + \frac{d}{\lambda} \mp \frac{1}{2} Q\, d\right) \tag{7-64}$$

Admittance,

$$U_{x,y} = \pi Q a^2 \left(\frac{d}{\lambda}\right)^{1/2} \frac{\{(1 + d/\lambda \mp \frac{1}{2}Q\, d)[1 - \frac{1}{4}Q^2 \lambda\, d(1 + d/\lambda \mp \frac{1}{2}Q\, d)]\}^{1/2}}{1 + d/\lambda \pm \frac{1}{2}Q\, d^2/\lambda - \frac{1}{2}Q^2\, d^2} \tag{7-65}$$

Asymptotic admittance as $\gamma \to \infty$,

$$U_\infty = \pi Q a^2 \left(\frac{D}{\Lambda}\right)^{1/2} \tag{7-66}$$

Assuming that the lenses are thin, so that $d/\lambda \ll 1$ and $Q\, d \ll 1$, the following approximate results may be derived:

Low-energy cutoff,

$$m\gamma_{\text{co}} \approx P_{\text{co}} \approx \tfrac{1}{2} Q (\Lambda D)^{1/2} \tag{7-67}$$

Optimum quadrupole strength,

$$(Q^2 \lambda\, d)_{\text{opt}} \approx 2 \tag{7-68}$$

$$(U_{x,y})_{\text{opt}} \approx \frac{\pi a^2}{\lambda}$$

$$\approx \pi Q a^2 \left(\frac{D}{2\Lambda}\right)^{1/2} \approx \left(\frac{1}{2}\right)^{1/2} U_\infty \tag{7-69}$$

$$\theta_{\text{opt}} = \pi/2 \text{ (betatron wavelength = 4 sectors)}$$

NUMERICAL COMPARISON OF FOCUSING SYSTEMS. Some typical numerical properties of the three systems discussed above are listed in Table 7-1. The following parameters are assumed:

L = spacing of alternating singlets = 12 meters
D = center-to-center length of multiplets = 2 meters
$\Lambda \approx$ sector length = 100 meters
a = radius of defining aperture = 0.85 cm

A typical asymptotic admittance of 0.3π (MeV/c)(cm) has been chosen to be compatible with the positron transport system (Chapter 16) for which the design admittance is 0.15π (MeV/c)(cm).

Another comparison is seen in Table 7-2, in which the locations of the *equivalent planes* of the system are shown. Employing the well-known equivalent-plane expansion yields

$$\begin{bmatrix} a_{11} & a_{12} \\ a_{21} & a_{22} \end{bmatrix} = \begin{bmatrix} 1 & -\zeta_2 \\ 0 & 1 \end{bmatrix} \begin{bmatrix} 1 & 0 \\ -P/F & 1 \end{bmatrix} \begin{bmatrix} 1 & \zeta_1 \\ 0 & 1 \end{bmatrix} \tag{7-70}$$

where $P/F = -a_{21}$, $\zeta_1 = (a_{22} - 1)/a_{21}$, and $\zeta_2 = (1 - a_{11})/a_{21}$. Here ζ_1 and ζ_2 are measures of the distances to the equivalent plane from the respective ends of the system.

A number of conclusions may be drawn from the comparisons listed in Tables 7-1 and 7-2:

1. All of the three systems considered are capable of adequate asymptotic (high-energy) admittance with quadrupoles of rather trivial size.

Table 7-1 Typical optical properties of alternative transport systems

Properties	*Alternating singlet*	*Sector doublet*[a]	*Sector triplet*[a]
Quadrupole strength[b] for $U_\infty = 0.3\pi$(MeV/c)(cm)			
per quadrupole	2.7 kG	9.7 kG	9.7, 19.4, 9.7 kG
per sector	22 kG	19.4 kG	38.8 kG
gradient[c]	0.68 kG/in.	2.4 kG/in.	2.4 kG/in.
Low-energy cutoff for $U_\infty = 0.3\pi$(MeV/c)(cm)	0.49 GeV	2.1 GeV	2.1 GeV
Beam energy at which $U_{\text{opt}} = 0.15\pi$(MeV/c)(cm)	0.83 GeV	2.1 GeV	2.1 GeV
Quadrupole strength at which $U_{\text{opt}} = 0.15\pi$ (MeV/c)(cm)	2.8 kG	6.8 kG	6.8, 13.6, 6.8 kG
Limiting admittance through Sector 2 ($m\gamma_1 = 0.6$ GeV, $m\gamma_2 = 1.2$ GeV)	0.11π(MeV/c)(cm)	0.05π(MeV/c)(cm)	0.06π(MeV/c)(cm)

[a] Doublet and triplet properties are based on the thin-lens approximation.

[b] Quadrupole strength is defined as gradient times effective length (Eq. 7-43).

[c] It is assumed that the singlet and doublet quadrupoles have effective lengths of 4 in. and that the triplet quadrupole effective lengths are 4, 8, and 4 in.

2. The singlets and doublets require comparable total quadrupole strength per sector and the triplets about twice as much. The singlet system would be considerably more expensive in initial cost because of the larger number of quadrupoles (8 per sector vs 2 or 3 for sector multiplets).
3. The singlets would, however, require considerably less total excitation power because the gradients are smaller.
4. The singlet system is appreciably broader band, i.e., for a given asymptotic admittance, the cutoff energy is lower.
5. The triplet has a rather strong appeal because of the fact that the equivalent planes are located very close to the physical center of the lens; i.e., the triplet acts very much like an ideal thin lens.
6. The triplet also has slightly larger admittance than the doublet [compare Eqs. (7-62) and (7-69)] amounting to a factor of 1.2 in the above example.

The general conclusion from these comparisons is that there is no compelling reason for deciding among the alternative systems on the basis of ideal beam optics alone. The problems of tolerances in magnet construction and alignment will now be considered as a possible basis for a choice.

Effects of quadrupole misalignments[14,15]

GENERAL NOTATION. Misalignments and other extraneous effects will tend to perturb the electrons from their ideal orbits. Using the matrix notation

Table 7-2 Location of equivalent planes relative to initial plane

			Numerical[b]	
	General formula[a]	*Optimal focusing*	*x plane (meters)*	*y plane (meters)*
Alternating singlet				
ΔZ_1[c]	$\mp f$	$\mp \dfrac{L}{\sqrt{5}-1}$	−9.7	9.7
ΔZ_2	$L \mp f$	$L \mp \dfrac{L}{\sqrt{5}-1}$	2.3	21.7
Sector doublet				
ΔZ_1	$\mp f$	$\mp \frac{1}{2}(\Lambda D)^{1/2}$	−7.1	7.1
ΔZ_2	$D \mp f$	$D \mp \frac{1}{2}(\Lambda D)^{1/2}$	−5.1	9.1
Sector triplet				
ΔZ_1	$\dfrac{D}{2 \mp D/f}$	$\dfrac{D/2}{1 \mp (D/\Lambda)^{1/2}}$	(1 + 0.165)	(1 − 0.124)
ΔZ_2	$D - \Delta Z_1$	$D - \Delta Z_1$	(1 − 0.165)	(1 + 0.124)

[a] $f = P/Q =$ quadrupole singlet focal length.

[b] Numerical values are for the optimal focusing case. The parameters as given in the text are $L = 12$ meters, $D = 2$ meters, $\Lambda = 100$ meters.

[c] ΔZ_1 and ΔZ_2 are defined as follows [see Eq. (7-70)]:

$\Delta Z_1 = P\zeta_1$

$\Delta Z_2 = P\zeta_2 + 2L$ (alternating singlets)

$= P\zeta_2 + \Lambda + D$ (sector multiplets) employed previously [Eq. (7-21) ff.], one obtains

$$\mathbf{x}_n = \mathbf{A}(n, n-1)\mathbf{x}_{n-1} + \delta\mathbf{x}_n \tag{7-71}$$

where the perturbation vector,

$$\delta\mathbf{x}_n = \begin{bmatrix} \delta x_n \\ \delta p_{xn} \end{bmatrix} \tag{7-72}$$

depends on the local imperfections in a manner which need not be specified for the moment.

Equation (7-71) is readily expanded to the formal solution

$$\mathbf{x}_n = \mathbf{A}(n, 0)\mathbf{x}_0 + \sum_{m=1}^{n} \mathbf{A}(n, m)\,\delta\mathbf{x}_m \tag{7-73}$$

which may be written alternatively

$$\mathbf{x}_n = \mathbf{X}_n + \boldsymbol{\xi}_n \tag{7-74}$$

where

$$\mathbf{X}_n \equiv \begin{bmatrix} X_n \\ P_{xn} \end{bmatrix} = \mathbf{A}(n, 0)\mathbf{X}_0 \tag{7-75}$$

$$\boldsymbol{\xi}_n \equiv \begin{bmatrix} \xi_n \\ \rho_n \end{bmatrix} = \sum_{m=1}^{n} \mathbf{A}(n, m)\,\delta\mathbf{x}_m \tag{7-76}$$

That is, the perturbed orbit is given by the sum of the unperturbed solution $\mathbf{X}_n$ and a perturbation term $\boldsymbol{\xi}_n$ which is a particular solution of the inhomogeneous difference equation (7-71) under the boundary condition $\mathbf{x}_0 = 0$.

PERIODIC OR ALMOST PERIODIC (ADIABATIC) SYSTEM. For a periodic or adiabatic system, the complex eigenvector solution may be written in terms of equations which are analogous to Eqs. (7-26) through (7-28), (7-37), and (7-38). Thus

$$\tilde{X}_n \approx \tilde{X}_0 \left(\frac{\sin\theta}{a_{12}}\right)_0^{1/2} \left(\frac{a_{12}}{\sin\theta}\right)_n^{1/2} e^{i\mu_n} \tag{7-77}$$

$$\tilde{\xi}_n \approx \left(\frac{a_{12}}{\sin\theta}\right)_n^{1/2} \sum_{m=1}^{n} \left(\frac{\sin\theta}{a_{12}}\right)_m^{1/2} \delta\tilde{x}_m e^{i(\mu_n-\mu_m)} \tag{7-78}$$

where

$$\tilde{X}_n \equiv X_n - i\left[\frac{1}{2}\left(\frac{a_{11}-a_{22}}{\sin\theta}\right)_n X_n + \left(\frac{a_{12}}{\sin\theta}\right)_n P_{xn}\right] \tag{7-79}$$

$$\delta\tilde{x}_n \equiv \delta x_n - i\left[\frac{1}{2}\left(\frac{a_{11}-a_{22}}{\sin\theta}\right)_n \delta x_n + \left(\frac{a_{12}}{\sin\theta}\right)_n \delta p_{xn}\right] \tag{7-80}$$

$$\tilde{\xi}_n \equiv \xi_n - i\left[\frac{1}{2}\left(\frac{a_{11}-a_{22}}{\sin\theta}\right)_n \xi_n + \left(\frac{a_{12}}{\sin\theta}\right)_n \rho_n\right] \tag{7-81}$$

INDEPENDENT RANDOM ERRORS. If the errors in different focusing sections are random and uncorrelated, the mean square amplitude perturbation of the orbit may be estimated as

$$\langle \xi_n^2 \rangle = \tfrac{1}{4}\langle (\tilde{\xi}_n + \tilde{\xi}_n^*)^2 \rangle = \tfrac{1}{2}\langle |\tilde{\xi}_n|^2 + \mathrm{Re}\,\tilde{\xi}_n^2 \rangle \tag{7-82}$$

since, from Eq. (7-81), ξ_n is the real part of $\tilde{\xi}_n$. Then, by Eqs. (7-76) and (7-78),

$$\langle \xi_n^2 \rangle \approx \frac{1}{2}\left(\frac{a_{12}}{\sin\theta}\right)_n \sum_{m=1}^{n} \left(\frac{\sin\theta}{a_{12}}\right)_m \{\langle |\delta\tilde{x}_m|^2 \rangle + \mathrm{Re}\{\langle \delta\tilde{x}_m^2 \rangle \exp[2i(\mu_n - \mu_m]\}\} \tag{7-83}$$

The oscillatory term in Eq. (7-83) makes only a small contribution if the sum is over a number of orbit wavelengths; hence a fair estimate of $\langle \xi_n^2 \rangle$ is

$$\langle \xi_n^2 \rangle \approx \frac{1}{2}\left(\frac{a_{12}}{\sin\theta}\right)_n \frac{1}{\pi} \sum_{m=1}^{n} \langle \delta u_m \rangle \tag{7-84}$$

where the phase space increment $\langle \delta u_n \rangle$ is defined by

$$\langle \delta u_n \rangle = \pi \left(\frac{\sin\theta}{a_{12}}\right)_n \langle |\delta\tilde{x}_n|^2 \rangle \tag{7-85}$$

$$\langle \delta u_n \rangle = \frac{\pi}{\sin\theta_n} \{-a_{21}\langle \delta x^2 \rangle + (a_{11} - a_{22})\langle \delta x\,\delta p_x \rangle + a_{12}\langle \delta p_x^2 \rangle\}_n \tag{7-86}$$

from Eq. (7-32).

Error analysis of alternative transport systems

ELEMENTARY PERTURBATIONS DUE TO ACTUAL QUADRUPOLE ERRORS. The effects of the principal error components in an individual quadrupole are presented below. Application to specific systems will be given in later paragraphs. (See Fig. 7-6 for definition of the misalignment components.)

1. *Transverse displacement.* The perturbation vector (Eq. 7-72) is readily found by a transformation from the symmetry axis of the quadrupole to the reference axis. The result referred to the quadrupole principal plane is

$$\delta\mathbf{x} = \begin{bmatrix} \delta x \\ \delta p_x \end{bmatrix} = \begin{bmatrix} 0 \\ Q \end{bmatrix} \varepsilon \tag{7-87}$$

using the lowest-order thin-lens approximation (Eq. 7-44c). The momentum impulse, $Q\varepsilon$, is of course just the line integral of eB_y at a distance ε from the quadrupole axis.

2. *Skew, or rotation about a transverse axis.* The perturbation is again calculated by a simple coordinate transformation. To the lowest-order lens thickness approximation, the result is

$$\delta\mathbf{x} \approx \frac{Q\,\Delta Z}{12P}\,\varepsilon' \begin{bmatrix} -2 \\ Q \end{bmatrix} \tag{7-88}$$

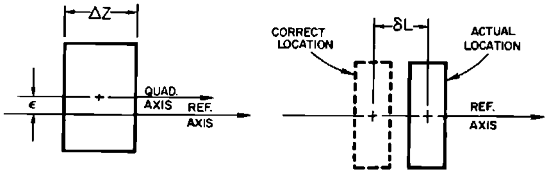

1) TRANSVERSE DISPLACEMENT

3) LONGITUDINAL DISPLACEMENT

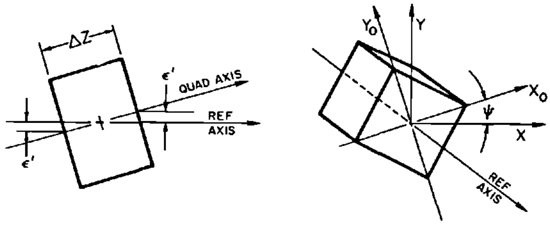

2) SKEWNESS OR TRANSVERSE ROTATION

4) AXIAL ROTATION;
(X_0, Y_0) = QUADRUPOLE SYMMETRY AXES
(X, Y,) = TRANSVERSE REFERENCE AXES

821A6

Figure 7-6 Quadrupole misalignment components.

(Note that ε' is defined as the transverse displacement of the ends of the quadrupole relative to the center.) The effect becomes very small in thin lenses, for which $\Delta Z \ll P/Q$, were P/Q is the quadrupole focal length.

3. *Longitudinal displacement.* By transforming the perturbed orbits to the unperturbed reference plane, it is found to first order that the displacement is

$$\delta \mathrm{x} \approx -\frac{Q\,\delta Z}{P}\mathrm{X} \tag{7-89}$$

where X is the unperturbed orbit just ahead of the quadrupole.

4. *Axial rotation.* In this case the perturbation introduces a coupling between x and y motions. Again, as a first-order approximation, it is found that for an axial rotation ψ,

$$\delta \mathrm{x} \approx -2QY\psi\begin{bmatrix}0\\1\end{bmatrix} \tag{7-90}$$

where Y is the unperturbed orbit amplitude in the y plane.

5. *Quadrupole strength error.* In the thin-lens approximation, the perturbation is

$$\delta \mathrm{x} = -X\,\delta Q\begin{bmatrix}0\\1\end{bmatrix} \tag{7-91}$$

where the quadrupole strength error δQ might result from an error in construction or in excitation current.

SAMPLE CALCULATION FOR RANDOM TRANSVERSE DISPLACEMENTS IN THE ALTERNATING SINGLET SYSTEM. As an illustration of the general method used in calculating orbit perturbations and error tolerances, consider the alternating singlet system with transverse displacement errors as shown schematically in Fig. 7-7.

The unperturbed transformation is given by Eq. (7-48). The net perturbation is found by transforming the effect of the individual impulses, given by Eq. (7-87), to the end of the section:

$$\delta \mathbf{x}_n = \begin{bmatrix} 1 & l_n \\ 0 & 1 \end{bmatrix} \begin{bmatrix} 1 & 0 \\ Q_n & 1 \end{bmatrix} \begin{bmatrix} 1 & l_n \\ 0 & 1 \end{bmatrix} \begin{bmatrix} 0 \\ Q_n \end{bmatrix} \varepsilon_{n_1} + \begin{bmatrix} 1 & l_n \\ 0 & 1 \end{bmatrix} \begin{bmatrix} 0 \\ -Q_n \end{bmatrix} \varepsilon_{n_2}$$

$$= \begin{bmatrix} 2Ql(1 + \frac{1}{2}Ql) \\ Q(1 + Ql) \end{bmatrix}_n \varepsilon_{n_1} - \begin{bmatrix} Ql \\ Q \end{bmatrix}_n \varepsilon_{n_2}$$

Assuming that the errors are random and uncorrelated, i.e.,

$$\langle \varepsilon_{n_1} \rangle^2 = \langle \varepsilon_{n_2} \rangle^2 \qquad \text{and} \qquad \langle \varepsilon_{n_1} \varepsilon_{n_2} \rangle = 0$$

the elementary phase space increment defined by Eq. (7-86) may be calculated; the result is

$$\langle \delta u_n \rangle = \frac{4\pi Q_n \langle \varepsilon^2 \rangle}{(1 - \frac{1}{4}Q_n^2 l_n^2)^{1/2}} \tag{7-92}$$

Hence, the mean-square orbit displacement, by Eq. (7-84), is

$$\langle \xi_n^2 \rangle \approx \frac{4}{Q_n} \left(\frac{1 + \frac{1}{2}Q_n l_n}{1 - \frac{1}{2}Q_n l_n} \right)^{1/2} \sum_{m=1}^{n} \frac{Q_m \langle \varepsilon^2 \rangle}{(1 - \frac{1}{4}Q_m^2 l_m^2)^{1/2}} \tag{7-93}$$

If the beam is coasting at constant energy with equal quadrupole settings, the result is

$$\langle \xi_n^2 \rangle = \frac{4n\langle \varepsilon^2 \rangle}{1 - \dfrac{1}{2}\dfrac{QL}{m\gamma}} \qquad \begin{cases} Q_n = Q = \text{constant} \\ \gamma_n = \gamma = \text{constant} \end{cases} \tag{7-94}$$

Figure 7-7 Alternating singlet system with transverse displacement.

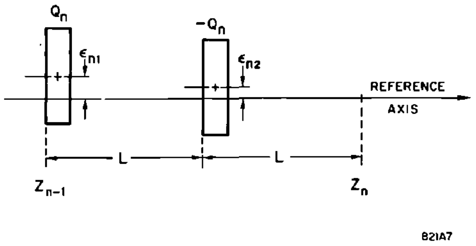

The beam would be very unstable if the beam energy were near the stop band, where $QL/m\gamma \approx 2$, but would be rather insensitive to energy above the optimum condition, i.e., if from Eq. (7-51) $Ql \leq \sqrt{5} - 1$.

SUMMARY OF QUADRUPOLE ERRORS AND ESTIMATE OF TOLERANCES. The basic algebra and the elementary perturbation expressions developed in the preceding paragraphs have been used to analyze the effects of various quadrupole errors for the alternative focusing systems and to assign tolerances to the error components on the basis of allowable beam perturbation.

In the case of doublets and triplets, certain correlations appear among the errors in the elements of a multiplet because of motions of the common supporting member. Figure 7-8 shows some of the error components associated with the multiplet systems, whereas Fig. 7-6 shows the basic components of independent quadrupole misalignment.

The misalignments considered here arise from the essentially random effects of fabrication, mounting, and alignment. Correlated misalignments over large distances, such as might arise from earth motions, tend to produce beam effects depending essentially only on total admittance, the effective average focusing force, and do not form a basis for comparison of alternative systems.

Figure 7-8 Misalignment components associated with common support structure in multiplets.

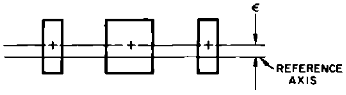

a) PARALLEL DISPLACEMENT
(DOUBLET OR TRIPLET)

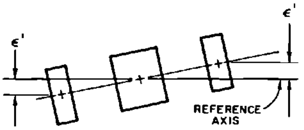

b) SKEWNESS (X OR Y ROTATION)
(DOUBLET OR TRIPLET)

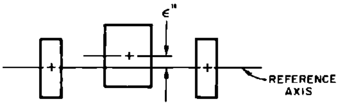

c) NON-COLLINEARITY

821A8

The "worst" conditions are, of course, minimum energy and maximum quadrupole strength. The following set of standard conditions, representing a constant-energy beam coasting through about half the machine, has been chosen for assigning tolerances:

Maximum allowable beam deflections, $|\xi|_{\max} = 0.1$ cm
Beam energy, $m\gamma = 2$ GeV (assumed constant)
Quadrupole strength (optimal)
  for alternating singlets, $Ql = L/f = \sqrt{5} - 1$
  for sector multiplets, $Q^2\lambda\, d \approx \Lambda/F \approx 2$
  (Here f is the singlet focal length, and F is the multiplet focal length.)

The numerical constants, as before, are

Spacing of alternating singlets, $L = 12$ meters
Doublet and triplet length, $D = 2$ meters
Sector length, $\Lambda = 100$ meters
Number of focusing periods in half the machine
  alternating singlets, $N = 60$
  sector multiplets, $N = 15$
Maximum orbit radius, $X_{\max} = Y_{\max} = a = 0.85$ cm

Table 7-3 lists the approximate dependence of mean-square orbit deviation $\langle \xi^2 \rangle$ on system parameters and error components for three systems considered in the coasting beam, constant parameter case. Table 7-4 gives the tolerances derived from these expressions.

The following observations may be made on the data presented in Table 7-4:

1. The most critical *transverse* alignment tolerances—*singlet displacement* (≈ 1.6 mils),* *doublet skew* (≈ 0.7 mil), and *triplet collinearity* (≈ 0.7 mil) —all result primarily from the dipole field component of displaced quadrupoles and, therefore, will be compensated almost completely by the magnetic steering dipoles† along the machine. Thus it may be concluded that these very tight tolerances actually apply only to short-term instability of the support system.
2. The other rather critical transverse tolerance (≈ 7 mils for parallel displacement of the multiplets) probably cannot be maintained in an absolute sense. Magnetic steering solves the problem partially; however, some dispersion between multiple beams at different energies would remain because the energy dependence of deflection by the displaced multiplet differs from that of a dipole. The alignment objective has been to meet the 7-mil figure as nearly as possible in order to facilitate multiple beam operation.

---

* 1 mil = 0.001 in.

† The steering dipoles are described in Section 7-3.

Table 7-3 Mean-square orbit uncertainties $\langle \xi^2 \rangle$ for various quadrupole error components, assuming coasting beam and constant parameters

Error	*Alternating singlet*	*Sector doublet*	*Sector triplet*
Parallel displacement	$\dfrac{4N\langle \varepsilon^2 \rangle}{1-\frac{1}{2}Ql}$	$\dfrac{1}{2}N\dfrac{Q^2\lambda\, d}{1-\frac{1}{4}Q^2\lambda\, d}\langle \varepsilon^2 \rangle$	$\dfrac{1}{2}N\dfrac{Q^2\lambda\, d}{1-\frac{1}{4}Q^2\lambda\, d}\langle \varepsilon^2 \rangle$
Skew (multiplet)	—	$2N\dfrac{\lambda}{d}\dfrac{\langle \varepsilon'^2 \rangle}{1-\frac{1}{4}Q^2\lambda\, d}$	$\frac{1}{2}NQ^2\, d^2\langle \varepsilon'^2 \rangle$
Collinearity (triplet)	—	—	$2N\dfrac{\lambda}{d}\dfrac{\langle \varepsilon''^2 \rangle}{1-\frac{1}{4}Q^2\lambda\, d}$
Longitudinal displacement (independent)	$2NX^2_{\text{max}}Q^2l^2\dfrac{1+\frac{1}{2}Ql}{1-\frac{1}{2}Ql}\dfrac{\langle(\delta L)^2\rangle}{L^2}$	$\dfrac{1}{4}NX^2_{\text{max}}\dfrac{Q^2\lambda\, d}{1-\frac{1}{4}Q^2\lambda\, d}\dfrac{\langle(\delta D)^2\rangle}{D^2}$	$\dfrac{1}{2}NX^2_{\text{max}}\dfrac{Q^2\lambda\, d}{1-\frac{1}{4}Q^2\lambda\, d}\dfrac{\langle(\delta D)^2\rangle}{D^2}$
Longitudinal displacement (multiplet)	—	$\dfrac{1}{2}NX^2_{\text{max}}(Q^2\lambda\, d)^2\dfrac{\langle(\delta\Lambda)^2\rangle}{\Lambda^2}$	$\dfrac{1}{2}NX^2_{\text{max}}(Q^2\lambda\, d)^2\dfrac{\langle(\delta\Lambda)^2\rangle}{\Lambda^2}$
Axial rotation (independent)	$16NY^2_{\text{max}}\langle\psi^2\rangle$	$NY^2_{\text{max}}\dfrac{\lambda}{d}\dfrac{\langle\psi^2\rangle}{1-\frac{1}{4}Q^2\lambda\, d}$	$2NY^2_{\text{max}}\dfrac{\lambda}{d}\dfrac{\langle\psi^2\rangle}{1-\frac{1}{4}Q^2\lambda\, d}$
Axial rotation (common)	—	$2NY^2_{\text{max}}Q^2\, d^2\langle\psi^2\rangle$	(Small)
Quadrupole strength (independent)	$4NX^2_{\text{max}}\dfrac{1+\frac{1}{4}Q^2l^2}{1-\frac{1}{4}Q^2l^2}\dfrac{\langle(\delta Q)^2\rangle}{Q^2}$	$\dfrac{1}{2}NX^2_{\text{max}}\dfrac{\lambda}{d}\dfrac{1}{1-\frac{1}{4}Q^2\lambda\, d}\dfrac{\langle(\delta Q)^2\rangle}{Q^2}$	$\dfrac{3}{2}NX^2_{\text{max}}\dfrac{\lambda}{d}\dfrac{1}{1-\frac{1}{4}Q^2\lambda\, d}\dfrac{\langle(\delta Q)^2\rangle}{Q^2}$
Quadrupole strength (multiplet)	—	$NX^2_{\text{max}}\dfrac{Q^2\lambda\, d}{1-\frac{1}{4}Q^2\lambda\, d}\dfrac{\langle(\delta Q)^2\rangle}{Q^2}$	$NX^2_{\text{max}}\dfrac{1}{1-\frac{1}{4}Q^2\lambda\, d}\dfrac{\langle(\delta Q)^2\rangle}{Q^2}$

Table 7-4 Summary of comparative error tolerances for alternative focusing systems[a]

Error	*Alternating singlet*	*Sector doublet*	*Sector triplet*
Parallel Displacement	1.6 mils[b]	7.3 mils	7.3 mils
Skew			
independent[c]	(Large)	(Large)	(Large)
multiplet	—	0.73 mil	73.0 mils
Collinearity (triplet)	—	—	0.73 mil
Longitudinal displacement			
independent	2.1 in.	2.4 in.	1.7 in.
multiplet	—	7.2 ft	7.2 ft
Axial rotation			
independent	0.21°	0.17°	0.12°
multiplet	—	6.1°	(Large)
Quadrupole strength			
independent	0.51%	0.43%	0.25%
multiplet	—	1.5%	1.5%

[a] See text for numerical values of system parameters appropriate for SLAC.

[b] 1 mil = 0.001 in.

[c] The orbit perturbation due to transverse rotation of an individual quadrupole is negligibly small.

3. The seemingly critical requirements on independent axial rotation and individual quadrupole strength are based on the pessimistic assumption that typical beam orbit amplitudes fill the whole available aperture. If moderately good phase space matching can be maintained along the machine, there should be a reasonable factor of safety beyond the figures given.

CHOICE OF FOCUSING SYSTEM FOR SLAC. Historically, the alternating singlet system was considered first but was rejected as being too complicated and requiring a transverse alignment tolerance of <2 mils on a very large number of independently supported quadrupoles.

The sector multiplet concept had the advantage that the focusing, steering, and beam-sensing instrumentation for each sector could all be contained in a single package; interaction between steering and focusing would be directly correlated, and operating adjustments would be easily understood.

Finally, triplets were initially chosen in preference to doublets primarily on consideration of alignment tolerances. For doublets, the critical tolerance on skewness, 0.7 mil in 40 in., is equivalent to an aiming stability of $\approx 2 \times 10^{-5}$ rad, and there was no certainty that this could be maintained stably with any reasonable support structure. Triplets, on the other hand, are very insensitive to skewness, and it was felt that the critical internal stability tolerances—in particular on the collinearity—could be held by a suitably rigid and thermally stable support structure. The triplet also has greater optical symmetry and slightly larger admittance.

Accordingly, triplets were originally chosen for the transport system and were used during early beam operation beginning in April 1966. Subsequently, the discovery of the beam breakup phenomenon and the resulting need for stronger focusing led to a rearrangement of the existing sector triplet quadrupoles into a combination of the alternating singlet and sector-doublet systems. This changeover is discussed under "The Magnetic Fix Program" in Section 7-5. No serious effects due to singlet and doublet misalignments have been encountered in actual machine operation, indicating great conservatism in the initial design.

Other transverse perturbations

SCATTERING BY RESIDUAL GAS.[16] The residual gas in the accelerator can spread the beam by single and multiple nuclear Coulomb scattering. It is interesting to note that these processes do not conserve beam phase space.

Nuclear form factors and recoil corrections can be neglected because the momentum transfers involved are small. Writing the Coulomb scattering cross section for single scattering in small-angle approximation as[17]

$$\frac{d\sigma}{d\Omega} \approx \frac{4r_0^2 Z^2}{\gamma^2(\theta^2 + \theta_1^2)^2} \tag{7-95}$$

where Z is the atomic number of the residual gas, $r_0 = e^2/m = 2.81 \times 10^{-13}$ cm is the classical electron radius and

$$\theta_1 = \frac{\lambda\!\!\!^{-}}{Z^{-1/3}\hbar^2/(me^2)} \approx \frac{Z^{1/3}}{137\gamma} \tag{7-96}$$

is the minimum effective scattering angle for a screened Coulomb field in the Fermi-Thomas model. If it is assumed that the transverse momentum acceptance, proportional to $\gamma\theta_m$, is independent of z, the total fraction of electrons lost is simply given by

$$\frac{4\pi N_s r_0^2 Z^2}{\gamma^2\theta_m^2 + (Z^{1/3}/137)^2} \tag{7-97}$$

where N_s is the total number of gas atoms per unit area.

The momentum acceptance is estimated as $m\gamma\theta_m \approx U/\pi a$, where U is the admittance and a is the aperture radius. If $U = 0.05\pi$ (MeV/c)(cm), then $\gamma\theta_m = 0.115$; let the residual gas be nitrogen at 10^{-6} torr or $N_s \approx 2 \times 10^{16}$ atoms/cm^2 for the 2-mile length; the fraction lost by single scattering is then 0.74×10^{-4}, which is negligible.

On the other hand, if it is assumed that $\theta_m = 0$, then the total fraction of electrons undergoing any single scattering (based on $\gamma\theta_1 = Z^{1/3}/137 = 0.014$) is $0.005 = \frac{1}{2}\%$.

Since this number may be interpreted as the total probability of single scattering for a given electron, it is concluded that the effects of plural and multiple scattering must be negligible also.

STRAY MAGNETIC FIELDS.[17] To estimate the effect of magnetic fields along the accelerator axis, consider the equation of motion of an electron in the absence of other transverse forces:

$$(Px')' = e(B_y - y'B_z) \approx eB_y \tag{7-98}$$

The $y'B_z$ term is negligible. The formal solution is

$$x = x_0 + \zeta(z, 0)p_{x_0} + e\int_0^z B_y(z_1)\zeta(z, z_1)\, dz_1 \tag{7-99}$$

where $\zeta(z, z_1)$ is given by Eq. (7-16).

As an example, consider the effect of a uniform field on a relativistic beam with uniform energy gradient in the absence of focusing. The magnetic deflection is

$$\Delta x = \frac{eBz}{m\gamma'}\left(1 - \frac{\gamma_0}{\gamma - \gamma_0}\ln\frac{\gamma}{\gamma_0}\right) \tag{7-100}$$

For $z = 3 \times 10^5$ cm, $m\gamma' = 0.06$ MeV/cm, $\gamma \gg \gamma_0$, and $B = 0.5$ G, we find $\Delta x \approx 750$ cm, i.e., the average transverse field would have to be reduced by a factor of 10^4 to keep the deflection to ≈ 1 mm; the tolerable field would be $\approx 6 \times 10^{-5}$ G.

The effect of external focusing on the deflection by stray magnetic fields may be calculated by the perturbation formulation used in the quadrupole error analysis [Eq. (7-71) ff.]. Considering the sector–multiplet type of focusing, the perturbation vector for one sector is obtained from Eq. (7-99):

$$\delta \mathbf{x}_n = \begin{bmatrix} \delta x \\ \delta p_x \end{bmatrix}_n \tag{7-101}$$

where

$$\delta x = \frac{e}{m\gamma}\int_{z-\Lambda}^{z} B_y(z_1)(z - z_1)\, dz_1 \tag{7-102}$$

and

$$\delta p_x = e\int_{z-\Lambda}^{z} B_y(z_1)\, dz_1 \tag{7-102}$$

on the assumption that the variation in γ per sector is adiabatic.

Two cases are considered explicitly:

1. *Uniform magnetic field over the entire length.* In this case it turns out that, if the quadrupole strengths are held essentially constant for compatibility with simultaneous beams of high and low energy, then the greatest deflection is at the highest beam energy. The result, based on the thin-lens approximation for sector multiplets, is

$$\xi_n \approx \frac{e}{m}\,\frac{B_y \Lambda^2 \gamma_n}{(\Lambda\gamma')^2 + 2\gamma_0^2} \tag{7-103}$$

where $m\gamma_0 = Q(\frac{1}{2}\Lambda D)^{1/2}$ is the energy at which the quadrupole strength is optimized [Eq. (7-62) or (7-68)]. For a typical case where $m\gamma_0 = 2$ GeV, $m\Lambda\gamma'$ = energy gain per sector = 0.7 GeV, $m\gamma_n$ = 20 GeV, and Λ = 100 meters, one finds

$$B_y = 1.4 \times 10^{-3}\ \mathrm{G}$$

as the field which produces a deflection of $\xi = 0.1$ cm.

2. *Random variation from sector to sector.* This could result, for example, from errors in setting or regulation of the degaussing system (see the paragraphs on the degaussing and magnetic shielding system below). Again constant quadrupole strength is assumed for compatibility with multiple beams. The mean-square deflection is found to be

$$\langle \xi_n^2 \rangle \approx \frac{n}{4}\frac{e^2}{m^2}\frac{\langle B^2 \rangle \Lambda^4}{\gamma_0^2} \tag{7-104}$$

which is nearly independent of beam energy. The Λ and γ_0 are defined above, and n is the number of sectors. Again taking $m\gamma_0 = 2$ GeV and $\Lambda = 100$ meters, it is found that

$$\langle B^2 \rangle^{1/2} = 2.4 \times 10^{-3}\ \mathrm{G}$$

for an orbit uncertainty of $\langle \xi_n^2 \rangle^{1/2} = 0.1$ cm at $n = 30$. A reduction of the external field by a factor approaching 10^3 is therefore required.

COUPLER ASYMMETRY.[18,19] The coupling of RF between the rectangular waveguide and the disk-loaded accelerator is accomplished through side slots in the end cavities of the 10-ft structure. (See Fig. 6-26.) The asymmetry of these couplers introduces transverse gradients in the accelerating field, which can deflect the beam in the manner of an RF separator.

The transverse impulse imparted by one coupler is related to the vector potential A_z and the electric field E_z accelerating the beam particle by[20]

$$\delta p_{xc} = e \int \frac{\partial A_z}{\partial x}\, dz = \frac{ie}{k} \int \frac{\partial E_z}{\partial x}\, dz \tag{7-105}$$

in which the integral extends over the region of the perturbation and k is the RF wave number.

The complex amplitude of the field acting on the particle at a particular point in the cavity is of the form

$$E_z = E(x)e^{i\Delta(x)} \tag{7-106}$$

where both the field amplitude $E(x)$ and the phase angle $\Delta(x)$ of the electron relative to the accelerating crest depend on x, the transverse coordinate in the coupler cavity.

The real part of Eq. (7-105) is then simply

$$\delta p_{xc} = -\frac{e\,\Delta z}{k}\left[\left\langle\frac{\partial E}{\partial x}\right\rangle_{\mathrm{AV}} \sin\Delta + \left\langle E\frac{\partial\Delta}{\partial x}\right\rangle_{\mathrm{AV}} \cos\Delta\right] \tag{7-107}$$

where $\langle\ \rangle_{\mathrm{AV}}$ refers to the average value of the quantity in question over the coupler cavity of length Δz.

Thus an amplitude asymmetry would produce a dispersive effect proportional to the bunch width, whereas a transverse phase variation of the field would produce a uniform deflection of the whole bunch, in phase with the accelerating field.

The effect of such momentum impulses, repeated coherently in each powered accelerator section of length ΔL, is mathematically equivalent to a uniform magnetic deflecting field of magnitude

$$B_c = \frac{1}{\Delta L}\frac{\delta p_{xc}}{e} \tag{7-108}$$

Hence the results obtained above for stray magnetic fields apply directly. Let the numerical values be $k = 2\pi/10.5 = 0.598\ \mathrm{cm}^{-1}$, $\Delta z =$ disk spacing $= 3.5$ cm, $\Delta \approx 5° \approx 0.1$ rad (typical RF bunch width), $\Delta L = 300$ cm, $E \approx 0.06$ MV/cm. Take $B_c \approx 1.4 \times 10^{-3}$ G corresponding to the tolerance from Eq. (7-103) for uniform magnetic field with moderate focusing, interpreted to give a betatron wavelength of four sectors at 2 GeV. The tolerances on coupler symmetry

$$\left|\frac{2a}{E}\left\langle\frac{\partial E}{\partial x}\right\rangle_{\mathrm{AV}}\right| \le 0.72\%$$

and

$$2a\left|\left\langle\frac{\partial\Delta}{\partial x}\right\rangle_{\mathrm{AV}}\right| \le 0.04° \tag{7-109}$$

are obtained where $2a =$ disk hole diameter ≈ 2 cm.

Quantitative effects of measured asymmetries of the SLAC couplers, and the cure by alternating the coupler orientations, are discussed in Chapter 6.

ACCELERATOR MISALIGNMENT. The misalignment effects to be considered here are associated with the accelerator structure itself, as distinguished from the special problems of the quadrupole misalignments discussed above.

Accelerator misalignments arise from fabrication errors, limitations of alignment precision, and environmental changes. The 10-ft accelerator sections are initially aligned on the 40-ft girder assemblies to a straightness of ±0.010 in.; the accelerator axis at the beginning of each 40-ft girder is referenced to the laser alignment system* to perhaps ±0.005 in.; absolute precision of the laser system itself is probably better than ±0.005 in. Mechanical

---

* See Chapter 22, "Support and Alignment."

loading by the rectangular waveguide and thermal distortions can contribute perhaps 0.010 to 0.020 in. to the intragirder deviations. Tolerances on the linkage between girders allow a maximum discontinuity of 0.015 in. in the accelerator axis.

In over a year of experience it has been found that the maximum motion of any point in the machine due to earth settlement is about 0.040 in. during a 3- to 4-month realignment cycle; maximum relative motion between any adjacent pair of support jacks is on the order of 0.005 to 0.010 in. in the same period.

The main effect of the initial random misalignment of the accelerator subassemblies is simply a loss in aperture of perhaps 10% in radius. This effect is not serious for the electron beam, which is kept to a radius of a few millimeters by the focusing system. Positron beam transmission, which is proportional to the fourth power of aperture, may be reduced appreciably.

Magnetic steering will cause only slight dispersion between interlaced beams of different energies. Transverse components of the accelerating field introduced by misalignment have a slight steering effect. This may contribute to the dispersion between interlaced beams and will generate slight motions of the beam when klystrons are turned on or off. To illustrate the latter effect, consider a misaligned 40-ft module, powered by a single klystron, and assumed to be internally straight. Figure 7-9 shows the optical equivalent of the module. The net deflecting impulse is due to the combination of the transverse component of the misaligned E-field and the fringe-field lens effect given by Eqs. (7-11) and (7-12). It is given to first order by

$$\delta p_x = eE \cdot \tfrac{1}{2}(\varepsilon_2 - \varepsilon_1) = \tfrac{1}{2} m\gamma'(\varepsilon_2 - \varepsilon_1) \qquad (7\text{-}110)$$

As a rather extreme example, assume a segment with a relative misalignment $\varepsilon_2 - \varepsilon_1 = 0.2$ cm, and an energy gain of $m\gamma' = 0.06$ MeV/cm. The impulse would be $\delta p_x \approx 0.006$ MeV/c, and the maximum beam deflection under focusing conditions corresponding to a betatron wavelength λ_β of four sectors at 1 GeV would be

$$\delta x \approx \frac{\delta p_x}{m\gamma} \frac{\lambda_\beta}{2\pi} \approx 0.04 \text{ cm}$$

Thus the steering effect in turning klystrons on or off can be appreciable.

Figure 7-9
Misaligned accelerator segment.

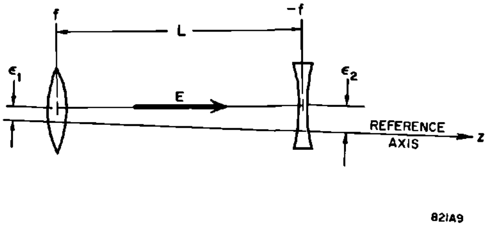

7-3 The beam control system

General description (RHH)

The major components used in beam control and monitoring will be reviewed briefly.

BEAM-ANALYZING STATIONS (BAS). These are two special instrumentation packages primarily intended for beam diagnostics; full details are given in Chapter 15. BAS-1 is located in the last 10-ft of the first 40-ft module of Sector 1 and BAS-2 occupies the first 40-ft of Sector 20. The most important features of both stations are magnetic spectrometers used in checking beam energy and spectrum. Beam current and position monitors also are included (see "Standard Drift Section" below). BAS-1 also contains a special, short quadrupole triplet which is part of the main focusing system; this is described under "Transport System" below.

LONG ION CHAMBER. The long ion chamber (commonly called "PLIC") consists of a coaxial transmission line, operated as an ion chamber, running the full length of the machine. Details are given in Chapter 21. The primary function of PLIC is to provide a signal used in the machine protection system. Another useful feature is that arrival time of signals at the injector end of the machine provides information as to location of sources of radiation and thus aids the operator in diagnosing the causes of beam loss.

DEGAUSSING AND MAGNETIC SHIELDING. Magnetic compensation is effected by degaussing wires and magnetic shielding along the accelerator and by steering dipoles at the end of each sector. Details are given below.

STANDARD DRIFT SECTION.* The layout of a typical instrumentation package (drift section) located at the end of each 333⅓-ft sector was shown in Fig. 5-22. The components include:

1. A *quadrupole doublet* (discussed under "Transport System" below).
2. The *reference cavity*, a TM_{010} resonant cavity driven by the beam current to generate a signal for phase reference and normalization of beam position monitor output (below). A portion of the signal from this cavity is logarithmically amplified and sent to central control as a broad-range beam current indication.
3. The *beam position monitor*, which consists of two TM_{120} rectangular cavities oriented to give signals proportional to the x or y displacements of the beam from the cavity axis, respectively. The phase of the signal

---

* The handling of signals from the various beam-sensing elements of the drift section is described in Chapter 15.

relative to the phase of the reference cavity tells the sign of the displacement, while the amplitude normalized by the reference-cavity amplitude is a measure of the amount of displacement.

4. The *beam intensity monitor*, which is a current transformer with a toroidal ferrite core, gives an accurate (1 %) measure of absolute beam current.
5. The *steering dipole*, which consists of Helmholtz-type coils rated at ≈2000 G-cm, equivalent to 0.6 MeV/c transverse momentum. It provides a final correction for all uncompensated deflections. The steering dipoles are designed for dc or pulsed operation.
6. The *beam profile monitor*, designed to display the transverse distribution of the beam. A retractable Čerenkov radiator of thin quartz, viewed by a television pickup, has been used, but this device is severely limited by heat dissipation in the radiator and by multiple scattering. A scanning device using a small (1 mm^3) beryllium bead on a fine wire has been developed, intercepting about 1 % of the beam. Detection of the scattered radiation provides a signal proportional to the beam intensity at the position of the bead.
7. The *beam scraper*, or protective collimator. This is a water-cooled copper collimator approximately 12 in. long with an aperture of 0.675 in. diameter, which is 2 mm smaller than the accelerator aperture. It tends to localize beam interception in case of mis-steering or poor focusing. The scrapers can dissipate 20 kW of average power (1 % of maximum design beam power) and can withstand a few beam pulses at full power. Indication of beam scraping is provided by PLIC and local discrete ion chambers. In the event of sudden beam interception by the scraper, the radiation information from PLIC will be used to shut the beam off within a few pulses.

The degaussing and magnetic shielding system[21,22] (RHH)

DESCRIPTION AND SPECIFICATIONS. Transverse stray magnetic fields result from several causes: the earth's magnetic field, magnetized reinforcing or structural steel, equipment in the klystron gallery, power line fields, and ground currents in the accelerator support girder. As shown in the previous section, the field tolerance is of the order of 2 mG, averaged over a sector, under moderate external focusing. Table 7-5 summarizes tolerances on the various magnetic effects.

Magnetic compensation was specified to limit the residual transverse field averaged over a given sector to 10^{-4} G.

Figure 7-10 shows the degaussing wires and shielding system. The degaussing currents in each sector are adjustable independently.

The magnetic shield was adopted primarily to compensate for the observed, short-range variation in the field (see the paragraphs on effects of magnetic fields, below). The shield also reduces ac fields, degaussing field fluctuations, and temporal variations in the earth's field which may amount to many

Table 7-5 Tolerances on magnetic effects under moderate focusing conditions[a]

Effect	*Tolerance*[b]
Uniform transverse field (full length)	1.4×10^{-3} G
Random sector-to-sector variations	2.4×10^{-3} G
Stray currents in the 24-in. diameter support girder	
dc	4 A
60 Hz[c]	40 A

[a] Betatron wavelength: four sectors at 1 GeV.

[b] The tolerances are set by allowing a maximum beam deflection of 1 mm.

[c] Increased shielding factor at 60 Hz due to skin effect in the accelerator pipe

milligauss per hour during magnetic storms. The shielding material is moly-Permalloy sheet, 6 mils thick. The inherent shielding factor is greater than 20 when the material is carefully demagnetized in an essentially null ambient field. However, the average dc shielding factor along the machine is on the order of 10 because of unavoidable gaps in the shielding at waveguide and water connections. At 60 Hz (skin depth ≈ 1 cm in copper), the shielding factor is larger by a factor of 10 due to skin effect.

Possible circulation of large ground currents, e.g., from power circuits and chemical EMF through the 24-in. aluminum support structure was once viewed with considerable alarm, and breaking up of ground loops by insulating gaps was considered. However, careful balancing and grounding procedures in the power distribution systems have kept the ac ground currents within tolerance; and chemical EMF were found to be insignificant.

EFFECTS OF MAGNETIC FIELDS. Figure 7-11 shows field measurements in the first few sectors of the tunnel before installation of the accelerator. Average field components are about 0.4 G vertical and 0.2 G horizontal, but short-range local fluctuations of over 0.5 G peak-to-peak are observed.

Figure 7-10 Magnetic shielding and degaussing system.

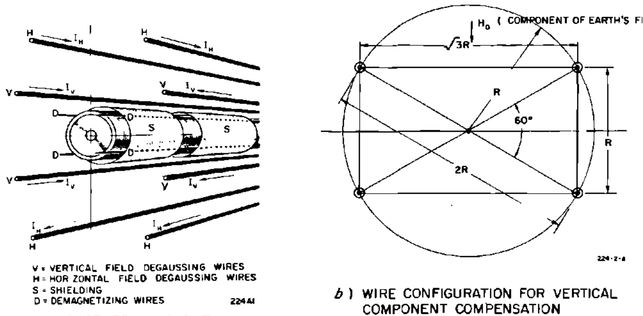

a) GENERAL LAYOUT

b) WIRE CONFIGURATION FOR VERTICAL COMPONENT COMPENSATION

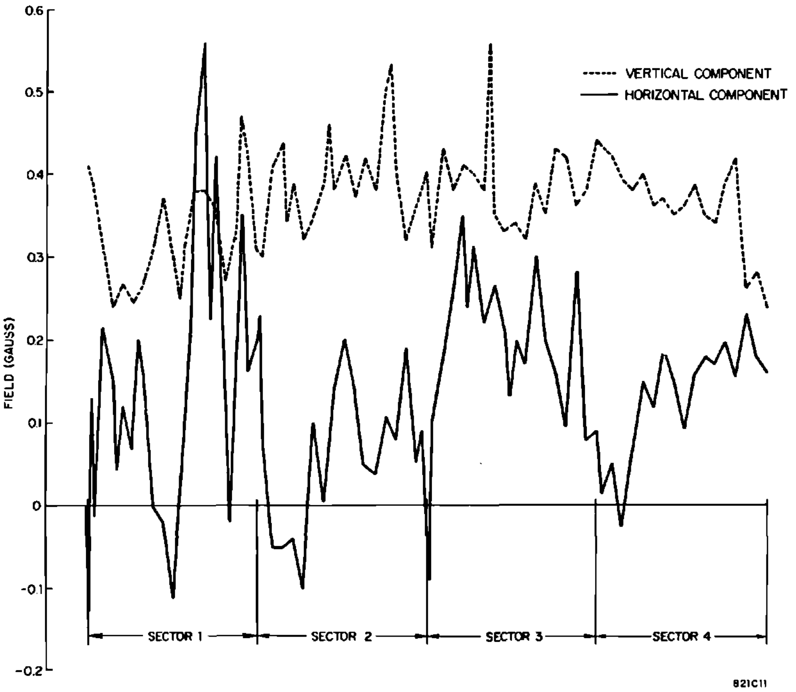

Figure 7-11 Magnetic field measurements in accelerator tunnel.

Figure 7-12 Beam deflections due to actual magnetic field.

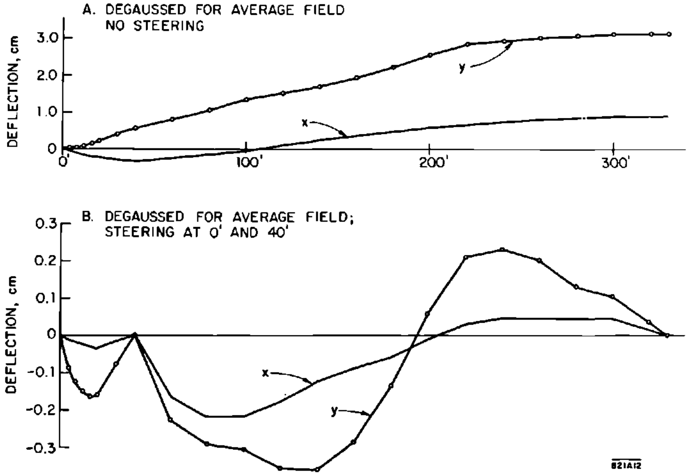

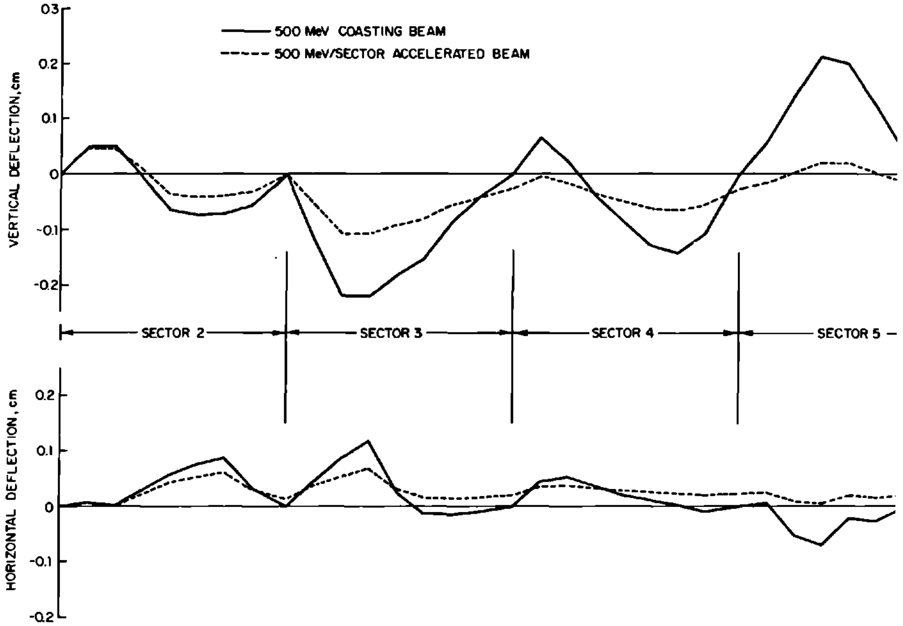

Figure 7-13 Dispersion between accelerated and coasting beams due to actual magnetic fields in early sectors.

Figure 7-12 shows computed deflections of the beam in Sector 1, neglecting focusing and shielding: (A) with the average field (but not the fluctuations) balanced out by the degaussing system and (B) with steering at the 0-ft point and at the 40-ft point (BAS-1), so that the beam is centered at BAS-1 and at the end of Sector 1. It is seen that with the latter conditions, the maximum deflections are greatly reduced. It is evident that a shielding factor of 10 would reduce the deflections to well within tolerance.

Figure 7-13 shows dispersion between a beam coasting at 500 MeV and a beam accelerated by 500 MeV per sector, based on measured fields in the first several sectors. The sector average fields are again assumed to be nulled by degaussing, and the steering is optimized for a 500-MeV coasting beam.

Transport system (RHH)

Here the existing accelerator transport system is described. The original sector triplet configurations of quadrupoles was rearranged into a combiantion of the alternating singlet and sector doublet schemes* in order to improve the beam current limit imposed by the transverse instability (see Section 7-4).

---

* See "Choice of Focusing System for SLAC," Section 7-2, and "The Magnetic Fix Program," Section 7-5.

Table 7-6 Quadrupole specifications for SLAC accelerator transport system

Specifications	*QA*	*QB*
Effective length[a]	4 in.	8 in.
Bore radius	0.6 in.	0.6 in.
Strength[a]		
nominal[b]	10 kG	20 kG
maximum	≈17 kG	≈40 kG
Energizing current		
nominal	6 A	6 A
maximum	≈12 A	≈15 A
Power (nominal)	45 W	72 W
Cooling	natural convection	

[a] Strength is given as $\int(\partial B_y/\partial x)\,dz$ and effective length is strength divided by central gradient.

[b] Excitation (strength vs energizing current) is linear up to at least the nominal values.

PHYSICAL DESCRIPTION. Two quadrupole designs are used. These are designated as types *QA* and *QB* and have effective lengths of 4 and 8 in., respectively; specifications are given in Table 7-6.

The optical elements of the system, in order of distance along the machine, are:

1. The BAS-1 triplet, consisting of quadrupoles *QA*, *QB*, *QA*, with each *QA* spaced 10.5 in. (center-to-center) from the *QB*. The electrical connection is series, with astigmatism control being provided by selective shunting of the *QB* or the *QA*'s.
2. Alternating singlets of type *QA* at 40-ft spacing through the rest of Sector 1, and at the same spacing in Sectors 2 through 6. The first singlet is at the 80-ft point of Sector 1 and the last is at the 280-ft point of Sector 6. Electrically the first singlet is run from a separate power supply, whereas in the remainder of Sector 1 and Sector 2 successive pairs are powered as independent doublets. In Sectors 3 through 5, quadruplet connections are used, and Sector 6 contains one quadruplet, one doublet, and one singlet, in that order. The disposition of the quadrupoles in Sectors 1 and 6 is shown schematically in Fig. 7-14.
3. Sector doublets of type *QA* in the drift sections DS-6 (end of Sector 6) through DS-9. Center-to-center spacing of the quadrupoles is 80.75 in.
4. Sector doublets of type *QB* in drift sections DS-10 through DS-29. Center-to-center spacing is 71 in.
5. A doublet of type *QA* in DS-30.

In all doublets, astigmatism control is available through selective shunting of either quadrupole.

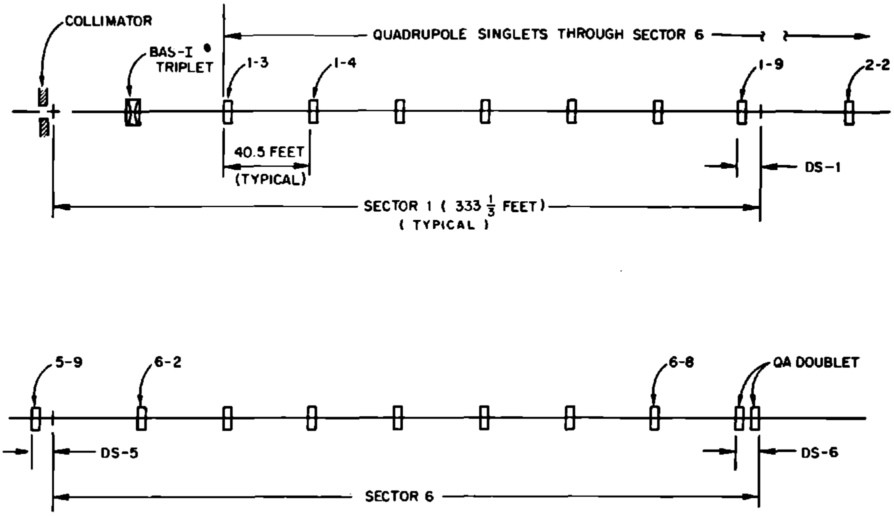

Figure 7-14 Schematic layout of quadrupoles in Sectors 1 and 6.

TRANSPORT PROPERTIES. The limiting admittance of the system occurs in the initial match into the alternating singlets, and is about 0.04π (MeV/c)(cm), compared to injector emittance of $\approx 0.004\pi$ (MeV/c)(cm). Typical quadrupole strengths in the singlet region are given by

$$Ql \approx \frac{QL}{m\gamma} = \frac{L}{f} \leq \sqrt{5} - 1$$

where $\sqrt{5} - 1$ is the "optimum" value. Using the numerical value $L = 40.5$ ft, one finds

$$Q \leq \frac{(\sqrt{5} - 1)}{L}\, m\gamma \approx \frac{m\gamma}{1000} \text{ (singlets)}$$

where Q is expressed in MeV/cm and $m\gamma$ in MeV. Corresponding betatron wavelengths [Eq. (7-53)] are $\lambda_\beta \geq 9.44L = 1.18$ sectors.

In the sector doublet region, typical quadrupole strengths are given by

$$Q(\lambda\, d)^{1/2} \approx \frac{Q(\Lambda D)^{1/2}}{m\gamma} \approx \left(\frac{\Lambda}{F}\right)^{1/2} \leq \sqrt{2}$$

where $\sqrt{2}$ is the "optimum" value. Corresponding betatron wavelengths are $\lambda_\beta \gtrsim 4$ sectors. In this case, the parameters $D \approx 200$ cm and $\Lambda \approx 10^4$ cm give

$$Q \lesssim \left(\frac{2}{\Lambda D}\right)^{1/2} m\gamma \approx \frac{m\gamma}{1000} \text{ (doublets)}$$

Thus, relationship between quadrupole strength and beam energy is practically the same for the singlets and doublets.

The maximum strength of the *QB* doublets, ≈40 kG or ≈12 (MeV/*c*)/cm, allows the optimum (4-sector) betatron wavelength to be maintained up to the 12-GeV point.

TYPICAL OPERATION. Usually most of the quadrupoles are set according to the above relationships between quadrupole strength and estimated beam energy. When interlaced beams of different energies are used, the quadrupoles must be set for the lowest energy.

The problem of phase space matching, between the injector and the singlet system and between the singlet system and the doublet system, has been solved approximately by use of the TRANSPORT computer program. In the computer fit, the BAS-1 triplet and the first singlet are varied to match the injector emittance to the remainder of the singlet system; the match of the singlets to the doublets is effected by tapering down the singlet fields in Sector 6, with independent adjustment of the last singlet and the drift section (Sector 6) doublet. When the actual quadrupoles are preset according to the computer fit, it is usually found that only minor readjustments are needed to establish good transmission.

Figure 7-15 shows typical beam envelope traces from the TRANSPORT computations in the region of the injector match and the singlet-to-doublet transition.

The quadrupoles always show some steering effects due to misalignments, but because of the high standards of prealignment and the excellent precision of the laser alignment system, these effects have not been very troublesome.

Figure 7-15a Computed envelope of matched beam through Sectors 1 through 5.

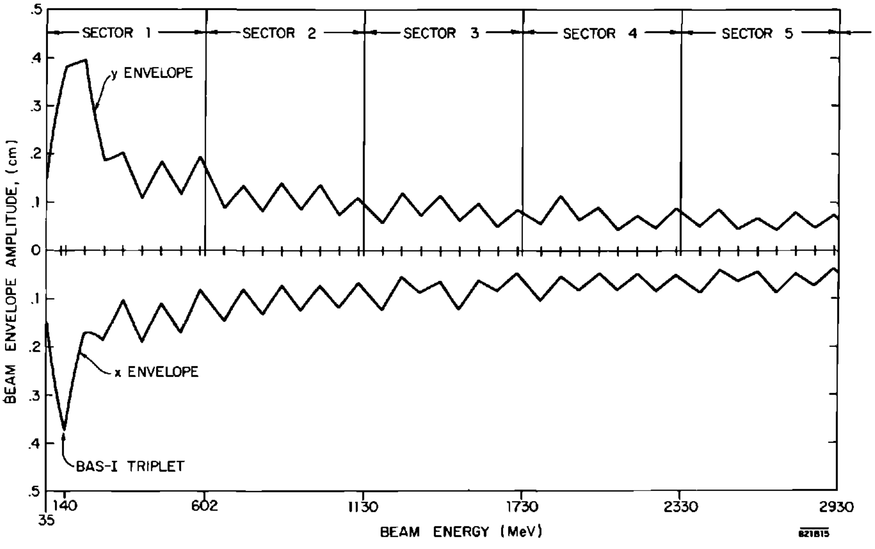

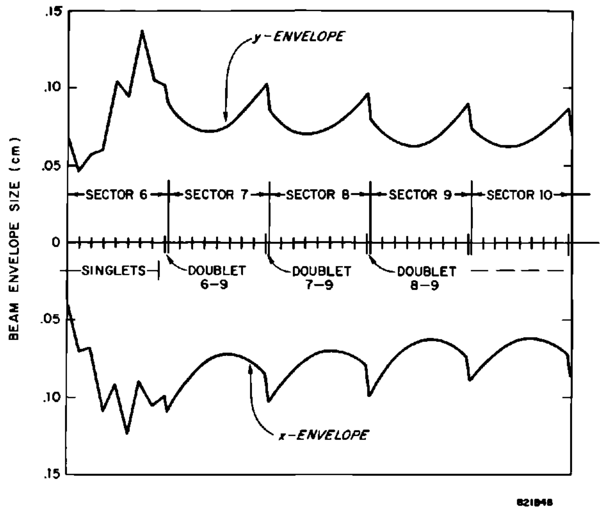

Figure 7-15b Computed envelope of matched beam —transition from singlet to doublet system.

*Phase space measurement**

The emittance of the accelerator was measured at the input to the beam switchyard. The equipment used in the measurement is shown schematically in Fig. 7-16. The beam from the accelerator was focused to achieve a minimum spot on the profile monitor. The beam diameter was measured at collimator No. 1 by steering the beam so as to scrape the beam on the collimator. The current through the collimator was measured with a toroid behind the collimator as a function of horizontal and vertical steering currents. Similarly, the current through collimator No. 2 was measured as a function of the steering currents. The first step in the measurement process was to adjust the quadrupole lens to minimize the beam diameter at the profile monitor. The beam

Figure 7-16 Equipment used in the measurement of accelerator emittance.

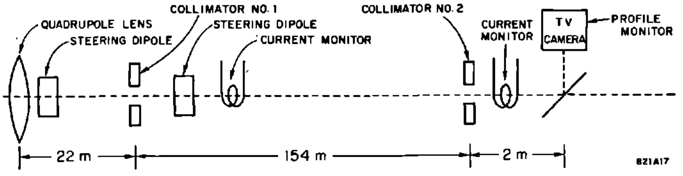

---

* This subsection written by R. H. Miller.

Figure 7-17 Emittance plane.

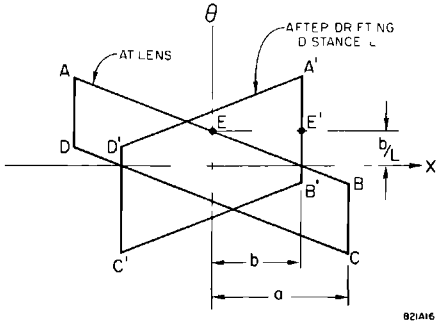

radii (a at the lens and b at the profile monitor) were then measured. As can be seen in Fig. 7-17, the radii a and b define a parallelogram in x, θ phase space, the area of which is

$$A = \frac{4ab}{L} \tag{7-111}$$

where L is the drift distance from the lens to the monitor. In Fig. 7-17 the parallelogram $ABCD$ represents the area in phase space at the lens limited by the radii a and b, whereas $A'B'C'D'$ represents the same area after transformation through the drift distance L. It is evident from the figure that the beam radius after the drift L is minimized by adjusting the beam convergence with the lens (and thus the slope of line segment AEB) until its image $A'E'B'$ is a vertical line since the θ coordinate of the point E' is unaffected by the lens. It is also evident that the beam passes through a waist somewhere between the lens and the end of the drift space. Similar considerations apply if the beam is represented by an ellipse in phase space. Following convention, the area of the largest ellipse contained within the parallelogram defined by the beam radii a and b will be used here. This area is

$$A = \frac{\pi ab}{L} \tag{7-112}$$

or in the conserved form

$$U = \gamma A = \frac{\pi ab\gamma}{L} \tag{7-113}$$

where γ is the energy of the beam.

The emittance of a 9.3-GeV beam with a peak current of 3.8 mA was measured. A sample of the data is shown in Fig. 7-18. Using Eq. (7-113), the fraction of beam current contained in the emittance ellipse of variable area was computed; the result is shown in Fig. 7-19. Ninety percent of the current is contained in 0.1π (MeV/c)(cm). This measured emittance is approximately one order of magnitude larger than the injector emittance reported in Chapter 8.

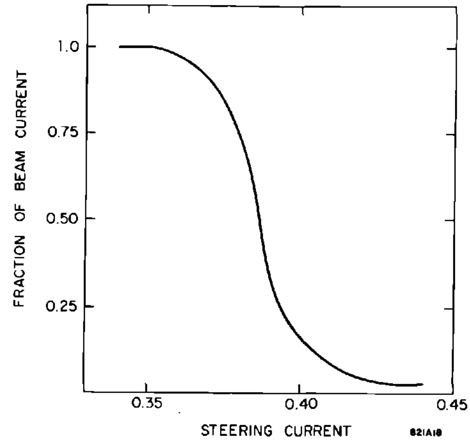

Figure 7-18 Beam current through collimator No. 2 vs steering current.

Figure 7-19 Beam current contained in a given accelerator emittance at $E = 9.3$ GeV, $I = 3.8$ mA peak.

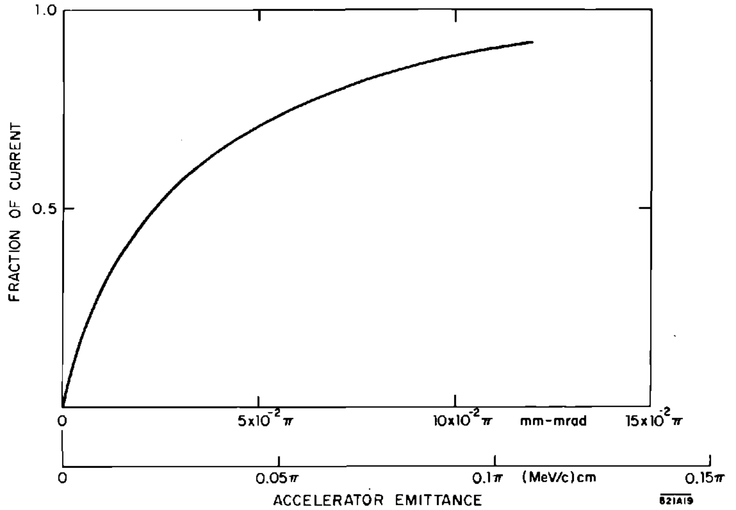

7-4 Theory and calculations of beam breakup

Effects of the beam on radial particle motion (WKHP)

In the previous sections, orbit motion has been treated as single particle dynamics in external fields. In all accelerators available, intensity is ultimately limited by instabilities produced by the action of beam-induced fields on the particle motion—and the electron linear accelerator is no exception.

SPACE CHARGE. If the effects of the currents induced in conducting surfaces surrounding the beam are ignored, the problem is reduced to analysis of conventional space-charge action. Let J be the current in particles per unit length in the beam,* concentrated in a cylinder of radius b and concentrated longitudinally into a bunch of phase length $\Delta\phi$. Using Eq. (7-2), the effect of the radial space charge can easily be shown to be described by

$$\beta(\beta\gamma r')' = \frac{J}{\gamma^2}\frac{rr_0}{b^2}\frac{4\pi}{\Delta\phi} = Ar\gamma^{-2} \tag{7-114}$$

where the γ^2 factor originates from the cancelation of electric and magnetic space-charge forces, and where r_0 is the classical electron radius. With reasonable numerical constants ($J = \frac{2}{3} \times 10^7$ electrons/cm, $b = 0.2$ cm, $\Delta\phi/2\pi = 0.015$) the constant A in this case becomes $A = 0.008$. The WKB solution of Eq. (7-114) indicates an exponential radial increase for $\beta \approx 1$ given by

$$r \approx \exp\left\{A^{1/2}\int_{z_0}^{z}\gamma^{-3/2}\,dz\right\} = \exp\left\{\frac{2A^{1/2}}{\gamma'}(\gamma_0^{-1/2} - \gamma^{-1/2})\right\} \tag{7-115}$$

for constant energy gain γ'. Numerically $\gamma' \approx 0.12$ cm^{-1}; the radial increase due to space charge is small if γ_0 at injection from the bunching section is large enough. If $\gamma_0 = 60$, then the radial growth factor after the injector is about 1.2.

RESISTIVE WALL EFFECTS. If the effects of currents in the conducting walls induced by the beam are considered, the phenomena are more complex. In general, the radial motion of individual particles will be affected by the so-called "wake field" of each bunch falling off inversely as the square root of the distance behind the bunch. This wake field is due to the induced currents in the tube wall and gives rise to the "resistive wall instability" observed in circular accelerators and storage rings. Calculation of this effect has been carried out only for a tube of smooth bore having walls of conductivity σ and, therefore, can be applied to SLAC only by the use of an "effective" radius R of somewhat uncertain magnitude. Calculation by Sessler[13,23] predicts an asymptotic amplitude increase described by

$$\exp\{Azt^{1/2}R^{-3}\sigma^{-1/2}\}^{2/5} \tag{7-116}$$

where A is a numerical constant. If $R = 1$ cm, a current of 530 mA causes the beam radius to increase from an initial misalignment offset of 0.05 cm to a radius of 1.0 cm at which beam loss would occur. Note that this is not a very large factor of safety beyond the rated current of 50 mA specified for SLAC.

---

* Note that $c = 1$.

BEAM BREAKUP. Considerably lower threshold currents are observed for the onset of instabilities. These instabilities are due to beam excitation of specific electromagnetic modes which produce a regenerative transverse deflection. Such instabilities have been observed in smaller linear accelerators for some time. However, one should clearly recognize that there are two quite distinct mechanisms by which such modes can lead to an exponential "blowup" of radial motion. The first mechanism, which is extensively discussed in the literature,[24–27] results from the negative group velocity of the HEM_{11} mode. This is the mode nearest in frequency to the TM_{01} mode used for accelerating. The HEM_{11} mode has a field configuration producing a transverse deflection of the beam[28] (Fig. 7-20).

The negative group velocity of the HEM_{11} mode will feed energy from the field excited by the beam in the end of each accelerating section toward the front. There it will produce additional transverse modulation in the beam which will, in turn, increase the excitation of the mode. This sequence of events leads to the regenerative action responsible for the conventional "backward-wave oscillator." This phenomenon characteristically occurs in a given section at currents of several hundred milliamperes.

The buildup mechanism which is dominant in limiting beam currents in the SLAC accelerator involves amplification from section to section and is coupled only through the electron beam. Of course, both mechanisms will contribute to transverse modulation buildup, but by way of introduction to the problem, a simple, but very general, model of the multisection buildup phenomenon is presented next.

Figure 7-20 (a) A ω–β diagram of conventional disk-loaded structure. (b) Field configuration of the HEM_{11} and TM_{01} modes in the disk-loaded structure.

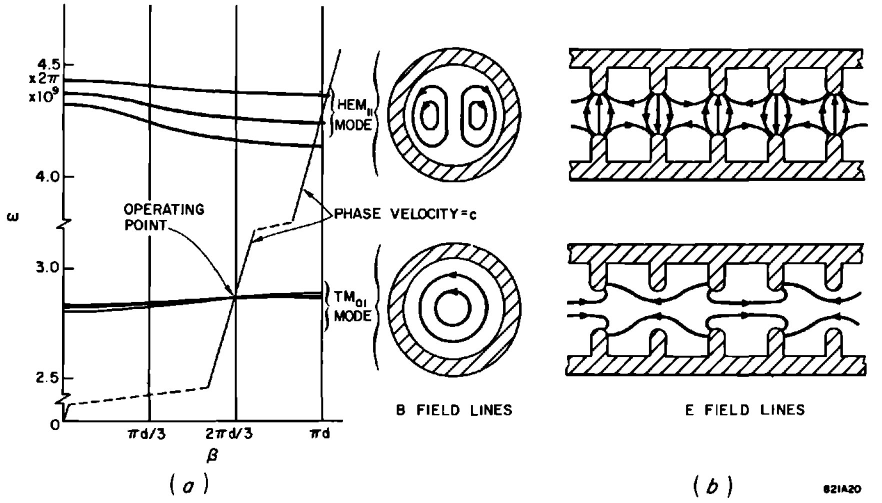

The multicavity model of beam breakup[29] (WKHP)

Let each accelerator section be represented by a single cavity. Let each cavity be excited in a mode of frequency ω_0 and quality factor Q; let the mode have a vanishing accelerating field E_z along the axis. Furthermore, let the rate of buildup be small compared to ω_0. Consider a particle of charge e to cross the nth cavity at a distance x from the z axis at a time t, and let the distance between cavities be L (Fig. 7-21). Let the fields (**E**, **B**) in the nth cavity be derived from a vector potential **A**. The transverse momentum per cavity is given as in Eq. (7-105) by[20,30]

$$\delta p_x = e \int \frac{\partial A_z}{\partial x}\, dz \tag{7-117}$$

giving rise to a radial differential equation of motion,

$$\frac{d}{dn}\left(\gamma \frac{dx}{dn}\right) = \frac{eL}{m} \int \frac{\partial A_z}{\partial x}\, dz \tag{7-118}$$

If the particle is deflected a distance x from the axis, in general it will do work against the field and thus the field amplitudes will be increased. Succeeding particles will then meet a larger deflecting field. This combined action of deflection by suitable fields and excitation of such fields by deflected particles gives rise to a buildup of transverse motion both in time and with distance along the accelerator.

A current eJ will deliver energy to the field at a rate

$$-eJ \int \mathbf{E} \cdot d\mathbf{z} = -Jxe \int \frac{\partial E_z}{\partial x}\, dz$$

Since $E_z = 0$ on the axis, the rate of buildup of energy U in a deflecting mode is then controlled by the relation

$$\frac{\partial U}{\partial t} + \frac{\omega U}{Q} = \mathrm{Re}\left\{-\frac{eJ}{2}\, x \int \frac{\partial E_z^*}{\partial x}\, dz\right\} \tag{7-119}$$

Figure 7-21 Radial orbits in multicavity model.

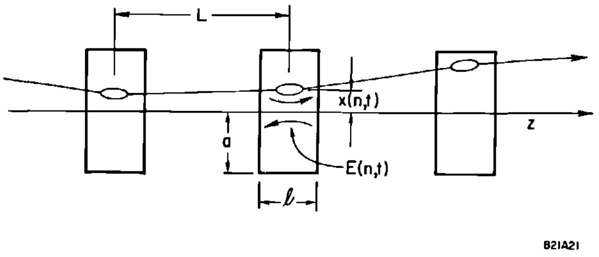

In general, the field energy U depends quadratically on the field integral

$$I = \int \frac{\partial E_z}{\partial x}\, dz$$

Specifically,

$$U = \tfrac{1}{2}\,\mathrm{Re}\,\{KII^*\} \tag{7-120}$$

where the constant K is given by

$$K = \frac{a^4}{181l} \tag{7-121}$$

for a simple cylindrical cavity of radius a and "interaction length" l.

When Eqs. (7-118) through (7-121) are combined, the basic beam breakup equation is obtained,

$$\left[\left(\frac{\partial}{\partial t} + \beta\right)\frac{\partial}{\partial n}\left(\gamma\frac{\partial}{\partial n}\right) + iCJ\right]x = 0 \tag{7-122}$$

where the dimensionless constant C is given by

$$C = 14.4\left(\frac{r_0\, l\lambda L}{a^4}\right) \qquad \text{and} \qquad \beta = \frac{\omega}{2Q}$$

and where the vector potential $\mathbf{A}$ is assumed to relate to the electric field $\mathbf{E}$ through $\mathbf{E} = -i\omega\mathbf{A}$. These equations govern the buildup of the displacement x with time from section to section, starting from initial disturbances. Among such starting sources are

Shot noise in beam
Shock excitation through misalignments
Thermal noise in early sections
Noise or spurious signals from klystron power sources
Electrical discharges in high microwave fields

Present experimental evidence is not conclusive as to which of these initial driving terms are important. However, all experimental data are consistent with a factor of 10^7 to 10^9 (e^{16} to e^{20}) increase from initial amplitude leading to loss of beam.

The solution of the beam breakup differential equation (7-122) can best be carried out by numerical computations as indicated in a later section. However, the general behavior of such solutions and the applicable scaling can be determined from the asymptotic solution, which can be derived analytically. Such a solution can be obtained by expressing the transverse displacement x as a Laplace transform along an appropriate contour C in the complex μ plane:

$$x(n, t) = e^{-\beta t}\int_C f(n, \mu)e^{\mu t}\, d\mu \tag{7-123}$$

where $f(n, \mu)$ obeys

$$\mu(\gamma f')' + iCJf = 0 \tag{7-124}$$

This has a WKB solution, valid for adiabatic variation of γ,

$$f(n, \mu) \sim \gamma^{-1/4} \exp\{\pm i(iCJ)^{1/2}\mu^{-1/2}g\} \tag{7-125}$$

where g is the integral

$$g(n) = \int_{n_0}^{n} \gamma^{-1/2}\, dn' \tag{7-126}$$

which is a known function of n for a given acceleration program $\gamma(n)$. The aymptotic solution valid for a large blowup factor can be generated by evaluating the integral (7-123) along a contour C along a path of "steepest descent" through the "saddle point" of the exponent located at

$$\mu = (CJ)^{1/3}\left(\frac{g}{2t}\right)^{2/3} e^{-i\pi/6} \tag{7-127}$$

The contour C passes through this point at an angle of $5\pi/12$ to the real axis. Evaluation of the integral gives

$$x(n, t) = x_0(n, t) \exp\left\{3\left(\frac{2^{1/3}}{4}\right)(\sqrt{3} - i)(CJt)^{1/3}g^{2/3} - \beta t\right\} \tag{7-128}$$

where $x_0(n, t)$ is a relatively slowly varying function given by

$$x_0(n, t) \approx J^{1/6}t^{-5/6}g^{1/3}\gamma^{-1/4} \tag{7-129}$$

The growth is thus controlled by the exponent

$$1.64C^{1/3}(tJg^2)^{1/3} \tag{7-130}$$

in the highly transient breakup observed at SLAC, where the term βt is small compared to the previous term. The effective onset of beam breakup corresponds to this exponent, assuming a value of 16 to 20. The exponent defines the scaling laws for beam breakup. The threshold of beam instability will occur for specific values of the quantity

$$s = CtJ\left[\int_{n_0}^{n} \gamma^{-1/2}\, dn'\right]^2 \tag{7-131}$$

This approximate treatment describes the principal qualitative features of the phenomenon and gives a good representation of the scaling laws. It ignores the multiplicity of modes which can generate the phenomenon, and it does not include contributions from the "backward-wave oscillator" mechanism, which is, however, relatively small in the SLAC accelerator. An analytical solution derived by iteration of Eq. (7-122) has been obtained by Bander[31] in the form of a series expansion; extensive results similar to the ones outlined here have been obtained by Voskresenskii, Koroza, and Serebryakov.[32–34]

Effect of focusing on beam breakup (WKHP)

Equation (7-122) describes the particle motion as affected by the beam-induced fields but omits the effect of any external focusing magnetic lenses. Their effect can be included by introducing a smoothed focusing term $\gamma k^2 x$ into Eq. (7-124), where k is the "betatron" wave number discussed earlier. The equation becomes

$$\mu[(\gamma f')' + \gamma k^2 f] + iCJf = 0 \qquad (7\text{-}132)$$

which has the WKB solution

$$f(n, \mu) = \gamma^{-1/4} \exp\left\{\pm i \int_{n_0}^{n} \left[\frac{iCJ}{\mu\gamma} + k^2\right]^{1/2} dn'\right\} \qquad (7\text{-}133)$$

Analytical evaluation of this expression by the "steepest descent" method appears difficult in general except for small values of k^2. If only terms linear in k^2 are carried, it is found that the beam breakup threshold is raised by a factor K given by

$$K = 1 + \frac{0.6}{s^{2/3}} \left(\int_{n_0}^{n} \gamma^{-1/2}\, dn'\right)\left(\int_{n_0}^{n} k^2 \gamma^{1/2}\, dn'\right) \qquad (7\text{-}134)$$

where s is the scaling parameter given previously in Eq. (7-131). This equation gives a fair description of the corrective effect of weak external focusing.

Numerical computation of beam breakup[35] (RHH)

Two different formulations have been used in computational studies of the beam breakup phenomenon: (1) a coupled resonator model, analogous to the treatment of transient wave propagation in the accelerator mode, as discussed in Chapter 6 and (2) the separated cavity model used in the analytical solutions discussed in the previous section.

COUPLED RESONATOR MODEL. Here the notation of Chapter 6 relating to transient filter characteristics and beam loading will be used. The simplified phenomenological wave equation, Eq. (6-17), is employed to describe the details of the interaction of the beam with the deflecting mode in the disk-loaded structure. It is assumed that the cavity wave function characteristic of the HEM_{11} mode is linear in x near the accelerator axis, i.e.,

$$\psi_{zn}(r) \approx x\psi_n^{(1)}(z)$$

where

$$\psi_n^{(1)} = \left[\frac{\partial \psi_{zn}}{\partial x}\right]_{x=0}$$

The transverse momentum impulse for an electron traversing the nth cell in terms of the z component of the vector potential A_{zn} from Eq. (7-117) is

$$g_n(\tau) = \frac{1}{m}\,\delta p_{x,n} = \frac{e}{m}\int_{\text{cell}}\left[\frac{\partial A_{zn}}{\partial x}\right]_e dz' \tag{7-135}$$

where $[\partial A_{zn}/\partial x]_e$ implies evaluation along an electron trajectory. On the assumption that the time variation of A_z is instantaneously sinusoidal, i.e.,

$$[A_{zn}]_e = A_n(\tau)\psi_{zn}\,e^{i\omega_n(\tau+z'/v)}$$

the following is obtained

$$g_n(\tau) = \frac{e}{m}\int_{-l/2}^{l/2}\psi_n^{(1)}(z')A_n(\tau + z'/v)\,dz' \approx \frac{e}{m}\,F_n A_n(\tau) \tag{7-136}$$

where

$$F_n = \int_{-l/2}^{l/2}\psi_n^{(1)}(z')e^{i\omega_n z'/v}\,dz' \tag{7-137}$$

is the "form factor" of the nth cell. With this substitution into Eq. (6-17), the wave equation

$$\left(\frac{\partial}{\partial\tau} + \beta_n - i\omega_n\right)g_n(\tau) + \frac{i}{2}\{\tilde{\Omega}_{n-1/2}\,g_{n-1}(\tau) + \tilde{\Omega}_{n+1/2}\,g_{n+1}(\tau)\} = -iC_n J(\tau)x_n(\tau) \tag{7-138}$$

is obtained, where

$\tilde{\Omega}_{n\pm1/2} = \Omega_{n\pm1/2}\,e^{\mp i\omega_n l/v}$,

$\Omega_{n\pm1/2}$ is the half-bandwidth of the structure, related to the coupling between adjacent cells,

$J(\tau)$ is the (slowly varying) beam current amplitude expressed as electrons per unit time,

$x_n(\tau)$ is the RF component of the centroid of the transverse beam displacement which has an instantaneous frequency close to ω_n.

C_n is defined by

$$C_n = \frac{2\pi r_0}{\omega_n}\frac{|F_n|^2}{u_n} \tag{7-139}$$

where $r_0 = e^2/m$ = the classical electron radius, $u_n = \int_{\text{cell}}|\psi_n|^2\,d^3\mathbf{r}'$ as defined in Chapter 6, and F_n is defined by Eq. (7-137).

The geometric constant C_n of Eq. (7-139) is essentially the C of Eq. (7-122) except that the definition here is for a single cell of the disk-loaded waveguide, and transit-angle correction of the cavity has been included through the form factor (Eq. 7-137). The constant C_n may also be related to the "transverse shunt impedance" defined by Altenmueller, Larsen, and Loew,[30] which is given in the present notation by

$$\left(\frac{r_\perp l}{Q}\right)_n = \left(\frac{R_\perp}{Q}\right)_n = 29.98\,\frac{\lambda_n^3|F_n|^2}{\pi^2 u_n} \tag{7-140}$$

where $R_\perp$ is the transverse shunt impedance per cavity in ohms, Q_n is the unloaded quality factor of the structure, and λ_n is the RF wavelength.

Evaluation of F_n and u_n by approximating the field as a simple TM_{11} cavity mode gives

$$\frac{r_\perp}{Q} \approx 29.98\,\frac{8\pi}{\lambda_n}\left[\frac{\sin(\pi l/\lambda_n)}{\pi l/\lambda_n}\right]^2\left(\frac{1}{\alpha_{11}J_0(\alpha_{11})}\right)^2 \tag{7-141}$$

where $\alpha_{11} = 3.823\ldots$ is the first root of $J_1(\alpha)$. SLAC parameters give $r_\perp/Q \approx 20$ ohms/cm.

The orbits, in the absence of external focusing, are given by simple recursion formulas:

$$p_{x,n+1/2} = p_{x,n-1/2} + mg_n(\tau) \tag{7-142}$$

$$x_{n+1/2} \approx x_{n-1/2} + \frac{l}{m\gamma_n}\,p_{xn} \tag{7-143}$$

in which the $n \pm \frac{1}{2}$ indices refer to the cell boundaries, and the midcavity values x_n, p_{xn} are appropriate averages.

A computer solution of the above formulation has been developed. The numerical method and boundary options for the wave equation (7-138) are as described in the discussion of transient filter characteristics and beam loading in Chapter 6. Simultaneous evaluation of the beam dynamics equations [(7-142) and (7-143)] is straightforward. For convenience in the numerical integration, the substitutions

$$x_n(\tau) = X_n(\tau)e^{i\omega'\tau} \qquad p_{xn}(\tau) = P_{xn}(\tau)e^{i\omega'\tau} \qquad g_n(\tau) = G_n(\tau)e^{i\omega'\tau} \tag{7-144}$$

are used, where ω' is an arbitrary reference frequency (independent of n) such that $|\omega_n - \omega'| \ll \omega_n$; the complex amplitudes X_n, P_{xn}, and G_n are assumed to vary slowly in phase and magnitude.

The simple dispersion equation, implied by the wave equation (7-138), i.e.,

$$\Omega_n \cos k_n l \approx \omega_n + i\beta_n - \omega \tag{7-145}$$

does not fit the measured dispersion curve over the entire passband (see Fig. 7-20a). However, useful results may be obtained by employing a fit of the parameters Ω_n and ω_n which is valid over a restricted frequency range. Figure 7-30 shows a result, obtained in this way, which simulates several resonant modes characteristic of the first few cavities of the SLAC disk-loaded structure. The existence of such resonances is explained by reference to Fig. 7-29 where it is seen that the π-mode cutoff frequency in the tapered structure increases with distance along the structure; thus a band of frequencies is trapped between the stop band and the input coupler, which is a large mismatch except at the frequency of the accelerating mode. For certain frequencies within this trapped band the round-trip phase shift is a multiple of 2π, and resonance occurs. The resonances near the beginning of the structure, and particularly the lowest one ($\approx$4140 MHz), are most nearly synchronous with the electrons and, consequently, are the most serious in exciting the breakup effect.

The computer experiments by which these resonances were found were performed by simulating a transverse beam modulation of constant amplitude and by varying the modulation frequency until resonance conditions were satisfied. Comparison of the computed resonances with experimental values are shown in Table 7-7. The "effective lengths" of the modes were found by comparing the net transverse impulse at each resonance with that of a single cell cavity.

Table 7-7 Comparison of computed and experimental resonant modes in the HEM$_{11}$ passband in SLAC waveguide

Computed resonant frequency (MHz)	*Experimental resonant frequency (MHz)*	*Computed effective interaction length (cm)*
4139.4	4139.64	23.2
4147.8	4147.50	8.9
4154.5	4154.00	11.2
4160.5	4159.72	8.1
4165.7	4164.82	8.1

By combining the effective length computed in this way with the shunt impedance per unit length as estimated above [Eq. (7-141)], it was possible to find the interaction impedance for an entire resonating region considered as a single cavity. For the dominant ($\approx$4140 MHz) mode,

$$\frac{R_{\text{eff}}}{Q} = \frac{r_{\perp} l_{\text{eff}}}{Q} \approx 460 \text{ ohms} \tag{7-146}$$

or in terms of the geometric constants defined in the previous section [Eq. (7-122)],

$$C \approx \left(\frac{\pi^2 r_0 L}{\lambda_n^2}\right) \frac{R_{\text{eff}}/Q}{30\,\Omega} \approx 2.5 \times 10^{-10}$$

A determination of R_{eff}/Q based on experimental beam breakup data is presented in a later paragraph; the result is

$$\frac{R_{\text{eff}}}{Q} = 400 \text{ ohms } (\pm 40 \text{ ohms})$$

which is in reasonably good agreement with the estimate.

Another interesting computer experiment done under the beam breakup theoretical program was an investigation of the regenerative type of blowup in coupled resonator structures. Figure 7-22 shows typical results under

Figure 7-22a Computed regenerative breakup in the first 30 cells of the SLAC injector showing growth of field during regenerative breakup. The quantity plotted is $|g_n|$ or $|A_n|$. Conditions: $I_0 = 3.0$ A; injection energy = 260 keV ($v/c = 0.75$); $Q = 8000$; $r_\perp = 0.16$ megohms/cm. The accelerating field varies approximately in accordance with steady-state beam loading. The starting signal is a delta function impulse of transverse modulation. The breakup takes place at a natural frequency of 4148.5 MHz, about 1 MHz above the second normal mode.

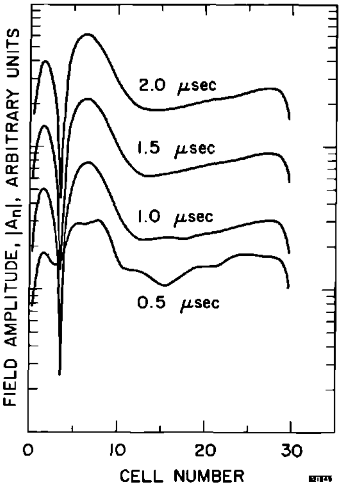

Fig. 7-22b Computed regenerative breakup in SLAC injector showing growth of beam deflection during regenerative breakup at several currents. Conditions same as in Fig. 22a.

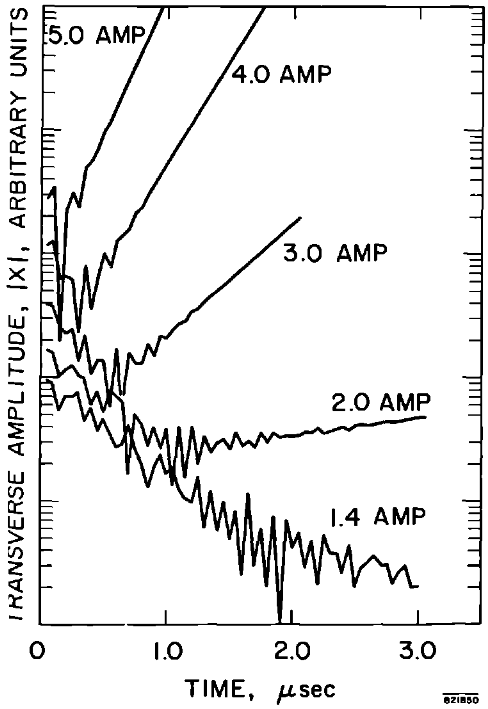

Figure 7-22c Computed regenerative breakup in SLAC injector showing exponential buildup rate of regenerative breakup as a function of beam current. Same conditions as in Fig. 22a.

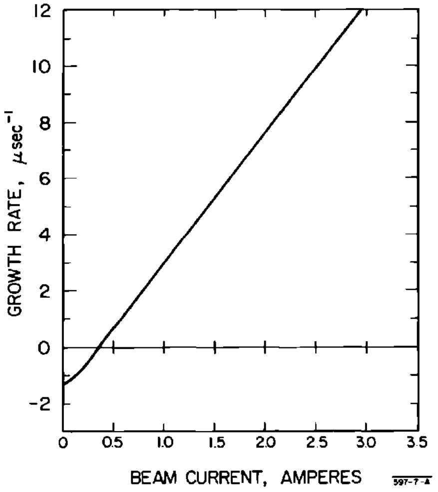

conditions simulating the SLAC injector. As discussed previously, regenerative breakup in a coupled cavity structure does not occur very readily in the SLAC accelerator design.

ISOLATED CAVITY MODEL. Formulation of multisection beam breakup in the previous sections treat the transverse modulation of the beam as a continuous, nearly sinusoidal wave with slowly varying amplitude and phase. Any effects of the longitudinal bunching of the beam are ignored in such a treament because of the implicit assumption that the beam charge is uniformly distributed over RF phase angle. Similarly, nonlinear focusing elements, such as sextupoles, are precluded by the assumption that the modulation is essentially sinusoidal. (It should be noted that the electromagnetic interaction between the beam and the RF deflecting mode is described by an essentially linear theory.)

It is of considerable interest to include these effects in the beam breakup theory. For example, the longitudinal structure of the beam, coupled with accidental misalignments, could contribute to the "shock excitation" of a driving signal to start the breakup. In cases where the bunching frequency and breakup frequency happen to be sufficiently close to a small-integer ratio, there may be important interference effects which could either enhance or dampen the rate of breakup. The effects of longitudinal structure might be of particular importance in the case of subharmonic bunching schemes.

On the other hand, nonlinear focusing elements could provide a mechanism, analogous to Landau damping, whereby the coherence of the transverse modulation would be partially destroyed by dependence of the betatron wavelength on transverse phase space.

As in the previous formulation of isolated cavity breakup, each accelerator section is treated as a short resonant "cavity," which is resonant in one of the modes described above. The form of the wave equation given by Eq. (6-14) is used. For a particular mode in the nth cavity, this becomes

$$\left(\frac{\partial^2}{\partial\tau^2} + 2\beta_n \frac{\partial}{\partial\tau} + \omega_n^2\right) A_n(\tau) = \frac{4\pi}{u_n} \int_{\text{cav}} \psi_{zn}(\mathbf{r}') J_z\left(\mathbf{r}', \tau - \frac{z'}{v}\right) d^3\mathbf{r}' \qquad (7\text{-}147)$$

where the various quantities may all be considered real, and the wave function now characterizes the normal mode rather than a single cell. In terms of the normalized momentum impulse [Eq. (7-135)] it may be shown that

$$g_n(\tau) \approx 2C_n \int_0^\tau J(t') x_n(t') e^{-\beta_n(\tau - t')} \sin\left[\omega_{rn}(\tau - t')\right] dt' \qquad (7\text{-}148)$$

where the quantities are defined formally in the previous section except that now in the definition of g_n, F_n, and u_n the integrals are over all the cavities participating in the resonance instead of over just a single cavity, and

$$\omega_{rn}^2 \equiv \omega_n^2 - \beta_n^2 \approx \omega_n^2$$

(the loss coefficient, $\beta_n = \omega_n/2Q_n$, is assumed $\ll \omega_n$).

Assuming that the beam current is bunched at a frequency $\omega_b = 2\pi/t_b$ so that

$$J(\tau) = \bar{J}(\tau)t_b \sum_{j=0}^{\tau/t_b} \delta(\tau - jt_b) \tag{7-149}$$

where $\bar{J}$ is the electron current averaged over the bunching cycle and using Eq. (7-148), one finds that the normalized impulse for the jth bunch is

$$g_n(j) = 2C_n t_b \sum_{j'=0}^{j} \bar{J}(j')x_n(j') \{\exp[-\beta_n t_b(j - j')]\} [\sin \omega_n t_b(j - j')] \tag{7-150}$$

This may be expressed more compactly as the imaginary part of a complex function $h_n(j)$,

$$h_n(j) = 2C_n t_b \sum_{j'=0}^{j} \bar{J}(j')x_n(j') \exp[i\theta_n(j - j')] \tag{7-151}$$

where

$$\theta_n = (\omega_n + i\beta_n)t_b \tag{7-152}$$

Figure 7-23 Computed beam breakup (BBU) growth as function of time and distance with typical SLAC parameters. Conditions: acceleration at 600 MeV/sector; $R_\perp/Q = 400$ ohms/active length in a 10-ft section; $Q = 8000$; beam breakup frequency = 4140 MHz; beam current = 7 mA; no focusing.

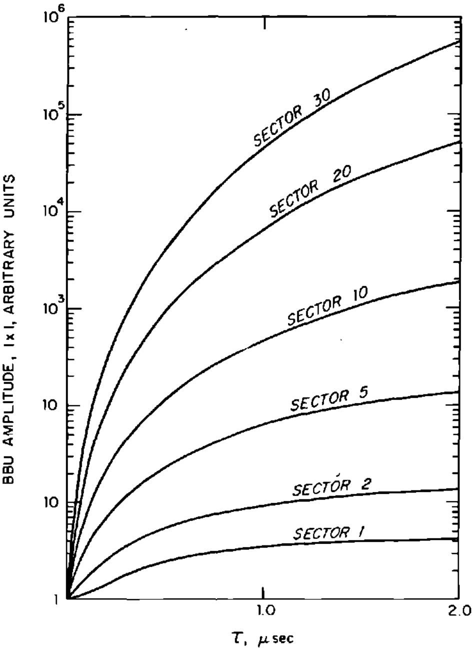

The function h_n satisfies the recursion relation

$$h_n(j) = 2C_n t_b \bar{J}(j) x_n(j) + h_n(j-1) \exp(i\theta_n) \tag{7-153}$$

which is useful for efficient numerical computation because it avoids the necessity of recomputing the entire summation [Eq. (7-150)] with every increment in time (or j).

The transformation of the jth bunch through the nth cavity to an impulse approximation, is

$$\left.\begin{aligned} p_{x,n+1}(j) &= p_{xn}(j) + m \operatorname{Im}[h_n(j)] \\ x_{n+1}(j) &= x_n(j) \end{aligned}\right\} \tag{7-154}$$

The numerical computation is carried out by tracing each successive bunch through the various elements of the system—cavities, accelerator and drift sections, lenses, etc.—starting with initial conditions such as h_n (0) = 0 and

Figure 7-24 Effect of external focusing on beam breakup threshold with typical SLAC parameters. Conditions: total length = 30 sectors; one sector = 333 ft; uniform acceleration at 600 MeV/sector; $R_\perp/Q = 400$ ohms/10-ft section; $Q = 8000$; f(beam breakup) = 4140 MHz; $\mu = 1.6$ μsec; constant betatron wavelength. The computed curve is based on sector focusing, i.e., discrete lenses at sector intervals, whereas Eq. (7-134) assumes a uniform and weak focusing force.

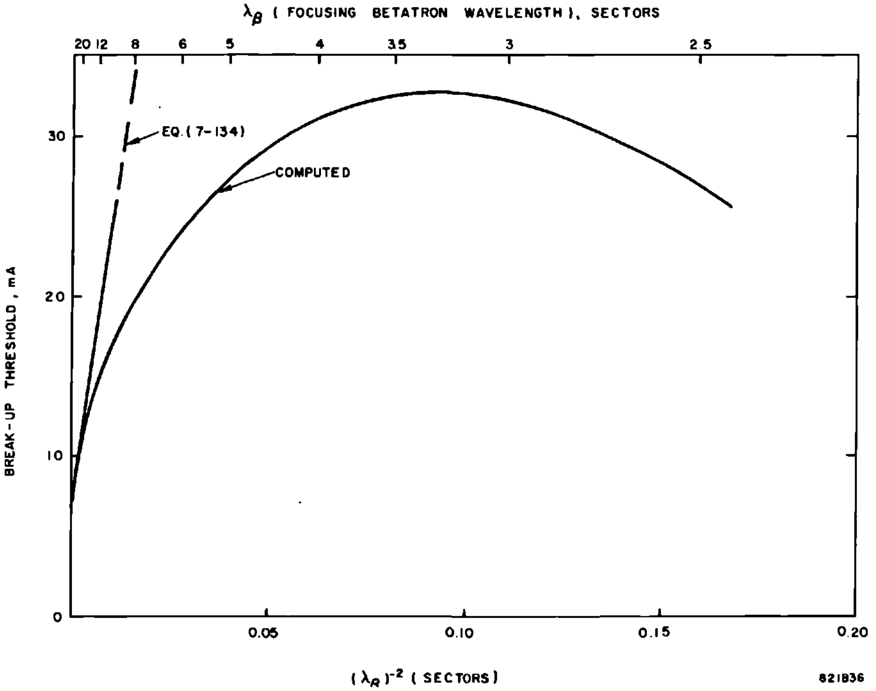

with boundary conditions such as $x_0(j)$ and $p_{x0}(j)$ being given functions of time (bunch number). Numerical calculations for the beam breakup for typical SLAC parameters are shown in Fig. 7-23, plotted in the absence of focusing. Curves computed when focusing is included are shown in Fig. 7-24.

7-5 Beam breakup: observations, experimental laws, and remedies

Qualitative observations (GAL)

The first observation of beam breakup at SLAC was made on April 27, 1966, 1 week after the beam was first turned on over two-thirds of the accelerator's 2-mile length.[36,37] Manifestations of the regenerative phenomenon known alternatively as beam breakup, beam blowup, or pulse shortening had been observed as early as 1957 in various, short, commercially built linacs operating in the 500-mA range. However, it was the surprisingly low current thresholds in the 10 to 20-mA range discovered with the SLAC accelerator which led to the analysis and understanding of the multisection type of interaction presented in the previous section of this chapter. Although the dates are not exactly known, it appears that similar observations made on the 2-GeV Kharkov linac in the U.S.S.R.[38,39] and on another linac in Japan[24] prompted the parallel studies already mentioned above.

The basic manifestation of the beam breakup effect at SLAC is illustrated in Fig. 7-25. As seen from the three video pulses, the injected beam pulse length, shown here to be 1.5 μsec for the top pulse, is shortened erratically when the beam current is increased above a certain value. The shortening becomes more pronounced as the current from the injector is increased. The pattern of pulses shown here can be observed at any location along the accelerator and the onset of breakup is determined by the beam current

Figure 7-25 Oscillograms of beam pulses below and above beam breakup threshold.

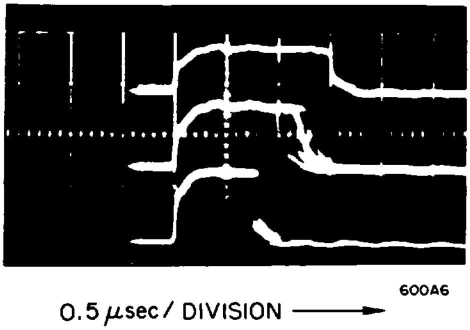

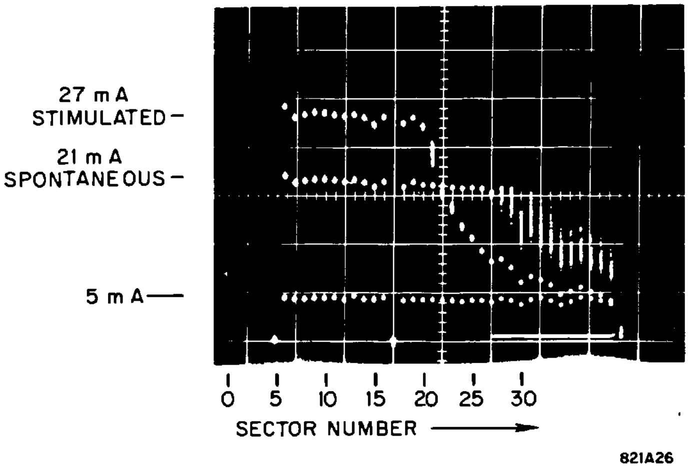

Figure 7-26 Transmitted beam profiles below and above beam breakup threshold (energy: 2 GeV; pulse length; 1.5 μsec).

transmitted through that point. Figure 7-26 shows an example of three different beam profiles along the machine. The ordinates of the dots represent the amount of charge transmitted past the end of each of the thirty accelerator sectors. In the lower trace (5 mA), the beam current from the injector is at a level below the breakup threshold for this particular set of energy, pulse length, and focusing conditions, and no current is lost along the accelerator. In the middle trace (21 mA), the injected current has been increased to a level above the natural breakup threshold. As can be seen, the current transmitted past Sector 20 becomes erratic and an increasingly large fraction of the electron bunches is lost to the accelerator walls and to the beam collimators. Thus, bunches which get transmitted to sectors beyond Sector 20 correspond to increasingly earlier parts of the injected pulse. In the upper trace (27 mA), the injected current has been further increased and, in addition, a few milliwatts of CW power at 4140 MHz have been injected onto the beam by means of an in-line cavity, 40 ft downstream of the injector. It is seen that breakup now occurs as early as Sector 14 and the external stimulation causes the breakup pattern to be less erratic, the amplitude of the driving term of the breakup mode having been stabilized. Still another manifestation of the beam breakup effect is illustrated in Fig. 7-27. This figure is a profile of the pulse obtained from the long ion chamber described earlier in this chapter. The peaks on the fine structure of the display correspond to ionization maxima resulting from beam scraping by the collimators, one of which is located at the end of each of the thirty sectors. In this example scraping starts at Sector 12, and there are 18 peaks to the end of the machine. Finally, Fig. 7-28 shows photographs of beam cross sections as observed at the end of the accelerator on a profile monitor. Various cases are shown. At the top, the current is below

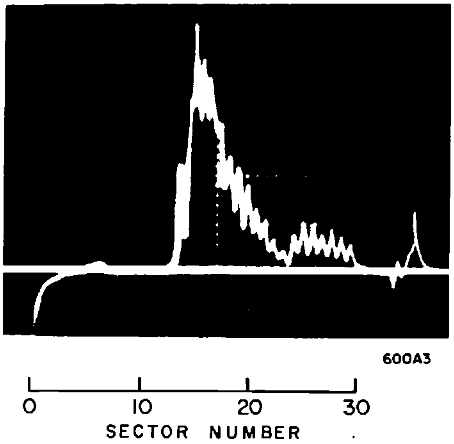

Figure 7-27 Long ion chamber profile for beam breakup at Sector 12 (5 GeV, 1.6-μsec pulse)

threshold for breakup. In the next picture, the breakup appears predominantly in the vertical direction. This direction is approximately perpendicular to the plane of the couplers. As will be discussed below, spontaneous breakup always starts in this plane because the Q of the HEM_{11} mode is greater in the vertical than in the horizontal plane. In the lower figures, the current has been increased even further and breakup now occurs more and more at random in all directions.

As this book is being written, more than a year has gone by since the first observation of beam breakup in the accelerator. Numerous measurements to compare theory and experiment have been performed. In the next two sections, an attempt will be made to summarize the experiments carried out to understand the microwave properties of the HEM_{11} mode and to verify the laws of breakup on the two-mile machine.

Microwave observations and experiments (GAL)

As discussed earlier in this book and particularly in this chapter, one of the important characteristics of the SLAC accelerating structure is that it is of the constant gradient design. Because of the tapered dimensions, the phase shift per cavity for any frequency other than 2856 MHz changes from cavity to cavity. Brillouin dispersion diagrams for specific cavities can be obtained with equivalent cavity stacks. Experimental data for the HEM_{11} mode in cavities at five different locations along a 10-ft section are shown in Fig. 7-29. The lowest resonant frequency at which beam breakup has been observed at the present operating currents (< 100 mA) is 4139.6 MHz, roughly 4140 MHz.

a) CURRENT BELOW BREAK-UP (12.5mA)

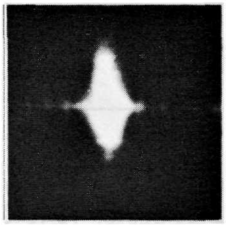

b) CURRENT FOR PREDOMINANTLY VERTICAL BREAK-UP (25mA)

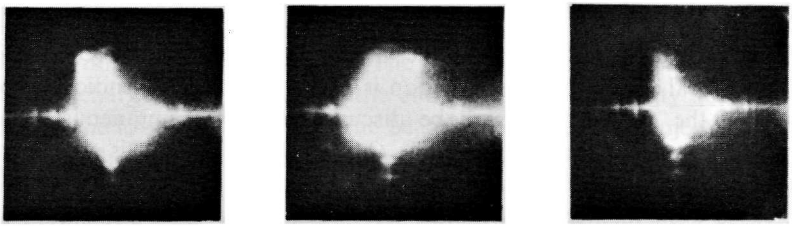

c) CURRENT WHERE BREAK-UP BEGINS TO OCCUR IN RANDOM DIRECTION (45mA)

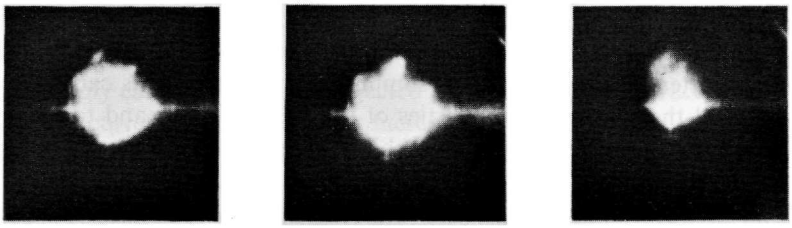

d) CURRENT FOR ENTIRELY RANDOM BREAK-UP DIRECTION (70mA)

821828

Figure 7-28 Beam cross sections as seen on profile monitor at the end of the accelerator (1.6-μsec beam pulse). These photographs were obtained from a 16-mm movie and represent frames taken at the rate of 24 frames/sec.

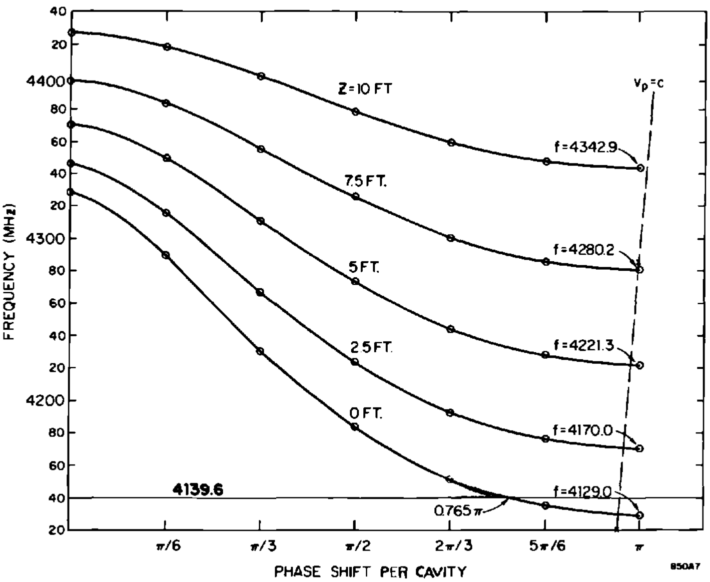

Figure 7-29 Brillouin diagrams for the HEM$_{11}$ mode at five locations along a constant-gradient section.

Since the electrons are bunched at 2856 MHz, the growing sine wave representing the envelope of their displacement appears not only at 4140 MHz but also at the difference frequency, 4140 − 2856 = 1284 MHz. It also appears at the difference between 4140 and the third harmonic of 2856, namely, 4428 MHz, and at 4428 − 2856 = 1572 MHz (etc.). Hence, although the basic microwave interaction takes place only at 4140 MHz, the other frequencies are always present on the beam. They can be detected by means of microwave probes and can also be used to precipitate and sharpen the breakup by artificially stimulating the beam with an external source. The mechanism by which the first and higher resonances can be excited is understood by further examining Fig. 7-29. At 4139.6 MHz, the phase shift of the first cavity beyond the coupler is 0.765π. As the wave at this frequency progresses along the guide, the phase shift per cavity reaches π and then becomes cut-off. As has been illustrated in Table 7-7, the lowest frequency resonance occurs when the phase shift through the first 8 to 10 cavities adds up to a multiple of π. Figure 7-30 shows that there is excellent agreement for the first three resonances between the computer calculations (Fig. 7-30b) and the VSWR measured at the input of the structure (Fig. 7-30a). The amplitude of the electric field intensity for the first mode nearest to the coupler has also been measured by means of a bead perturbation test and is illustrated in Fig. 7-31. The phase angle in Fig. 7-30b is plotted for the wave with respect to a relativistic beam. The fact that this phase angle is not zero can be understood since in Fig. 7-29, the crossover of the $v_p = c$ line allows only quasi-synchronism.

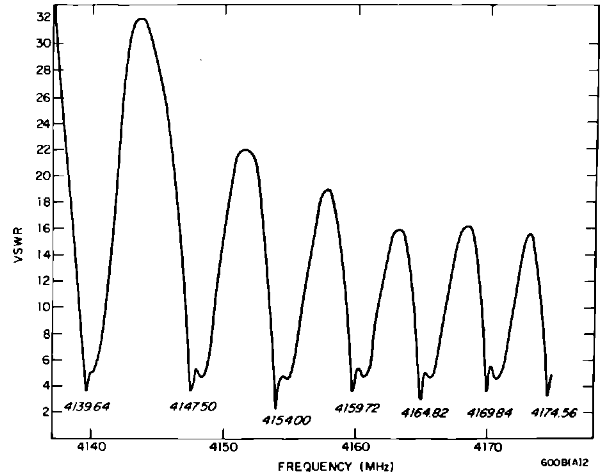

a) VSWR LOOKING INTO SECTION INPUT

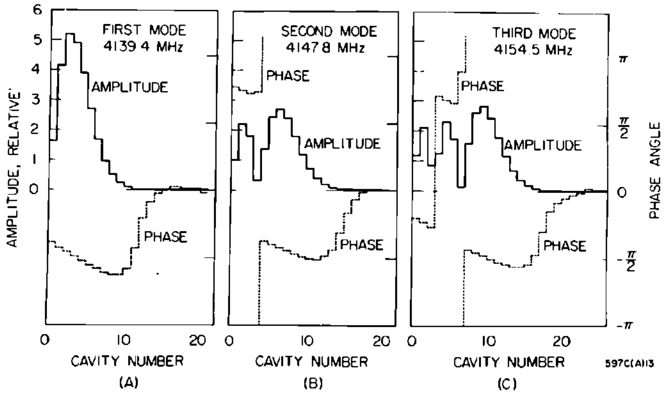

b) EXAMPLES OF COMPUTED AMPLITUDE AND PHASE DISTRIBUTION

Figure 7-30 Measured and computed HEM$_{11}$-mode resonances in SLAC constant-gradient section. (a) Measured VSWR; (b) computed.

Another important observation to be made in Fig. 7-30a is the fact that the valleys in the VSWR curve exhibit two minima. Although this fact is not yet completely understood, it appears that the two minima correspond to the horizontal and vertical HEM$_{11}$ mode polarizations. Whether beam breakup starts from noise or is stimulated through some external source, both horizontal and vertical polarizations are possible. This fact is further illustrated in Fig. 7-32 where the mode polarization of the HEM$_{11}$ wave excited through the horizontal input coupler of an accelerator section is plotted as a function of frequency. As already shown in Fig. 7-28, for low beam currents and long

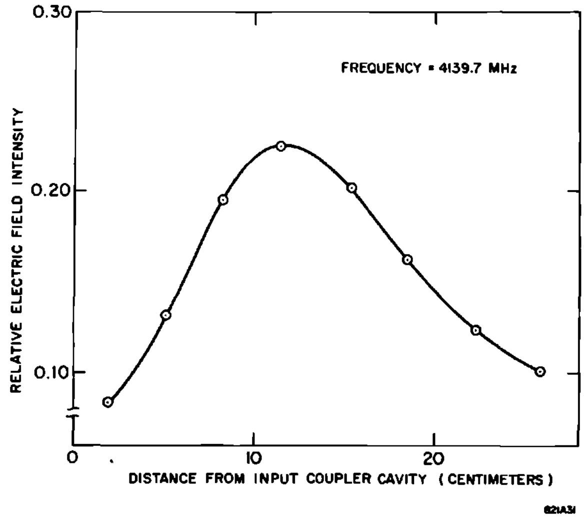

Figure 7-31 Measured electric field variation in the first eight cavities of a 10-ft accelerator section, when excited at 4139.7 MHz through the input coupler.

Figure 7-32 Axial electrical field intensity for the HEM_{11} mode in the first eight cavities of a 10-ft accelerator section as function of azimuthal angle, when excited through the input coupler. Plots are shown for five different frequencies.

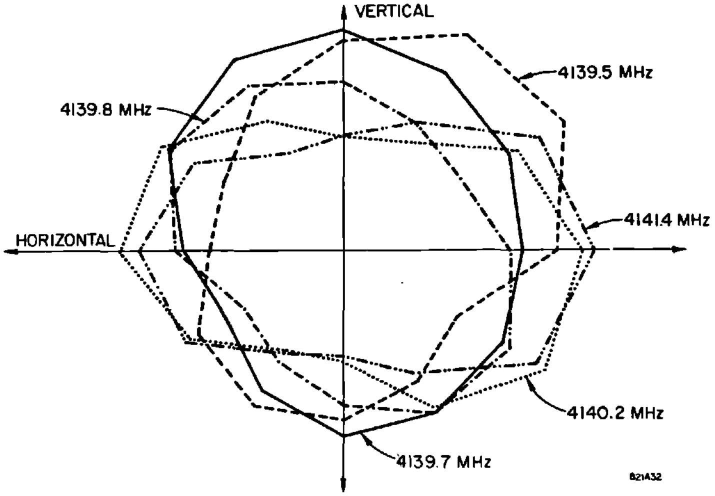

pulses, breakup appears first in the vertical plane, and it is only after increasing current above the vertical threshold in a ratio of approximately 3 : 2 that the orientation of the breakup plane becomes random. Although a definitive measurement of Q has not yet been made, it appears that the value in the vertical plane, Q_0, is of the order of 8000 and that Q_L, the loaded Q in the horizontal plane, is roughly two-thirds of this value. The one-way travel time of the resonant wave is of the order of 50 nsec. Hence, for very short high-current injector pulses, the beam still breaks up in one plane, but since there is no time for resonant buildup, the orientation of the plane is random from pulse to pulse.

In addition to the cold tests described so far in this section, several other microwave experiments were conducted directly on the accelerator. These experiments included the measurement of beam breakup gain and investigation of the effects of external stimulation, as will be described in the next paragraph, and the "feedback" described below. For this purpose several in-line cavities were installed along the accelerator in available space in the drift sections. An example of two such C-band cavities is shown in Fig. 7-33. Similar cavities resonant at the difference frequency, 1284 MHz, were also installed at discrete locations for the purpose of performing feedback experiments. The object of the feedback experiments was to derive a beam-induced signal proportional to the beam transverse displacement in one cavity, to amplify the signal, and feed it back into an adjacent cavity so as to impart a corrective transverse momentum impulse to the beam. One such experiment, illustrated in Fig. 7-34, was performed at 1284 MHz with a 10-kW pulsed output amplifier. The total gain and time delays in the feedback chain were approximately 100 dB and 50 nsec, respectively. Measurements on frequency modulation through the 1284-MHz pulse indicated that a 50-nsec time delay introduced only 12° phase slip between induced and fed-back signals. With

Figure 7-33 Cavities (4140 MHz) used in breakup experiments.

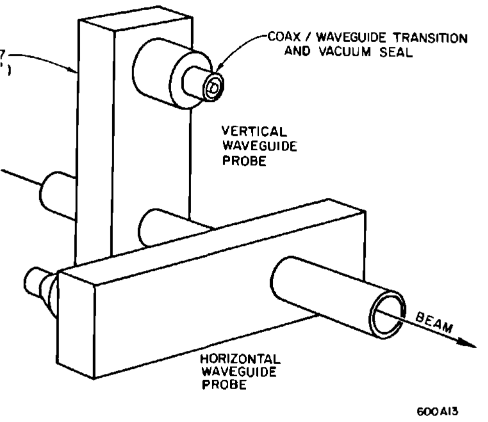

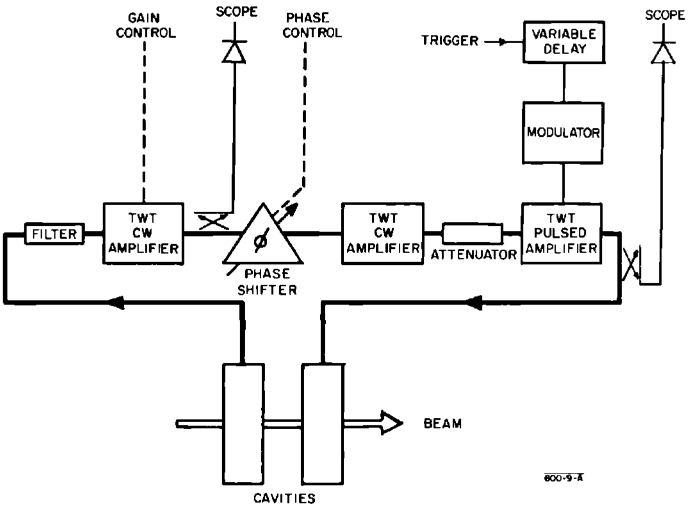

Figure 7-34 Block diagram of beam breakup, feedback experiment.

the equipment installed at the end of Sector 3, after very careful phase and gain adjustments, it was barely possible to move the location of natural breakup for a given current by as much as one sector length. When the current was increased by 20%, cancellation was no longer obtained. From this experiment, it was concluded that to make the feedback system workable, several stages would be necessary along the machine, perhaps as many as five to ten. Since the cavities only pick up one polarization, both horizontal and vertical cavities would be required. The gain and bandwidth of the amplifier chains would have to be considerable, and the system would, thus, be very expensive and complex. For these reasons, as will be discussed below, feedback cancellation was not adopted as a beam breakup remedy at SLAC.

Experimental verification of beam breakup laws (GAL)

The analytic expressions and computational studies presented early in this chapter have been tested experimentally on the SLAC accelerator under a variety of conditions. The degree to which these laws have been verified will now be discussed.

Referring to Eqs. (7-128) and (7-131), it is seen that for uniform acceleration, the variation of beam breakup current as a function of inverse distance should be approximately linear. This fact, verified by computer calculations, is illustrated in Fig. 7-35. Similarly, it can be shown that for a beam accelerated to a given point and coasting from there on, proper integration of Eq. (7-126) gives a parabolic variation of log x as a function of the cube root of the distance where x is the transverse amplitude of the beam. This fact is shown in Fig. 7-36. If, on the other hand, distance and pulse length are kept

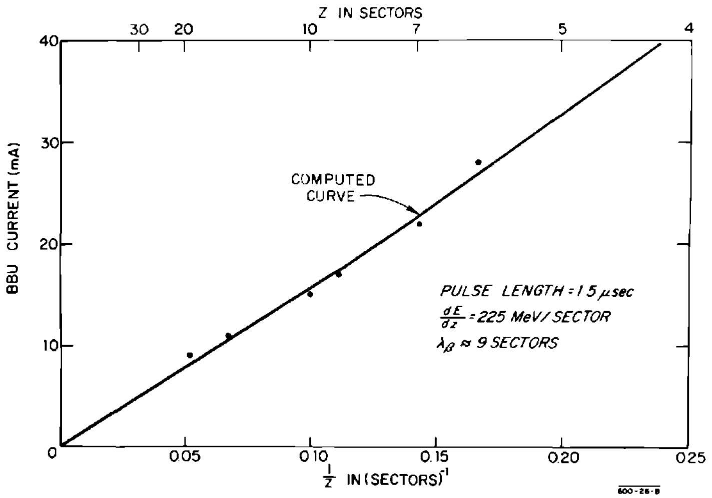

Figure 7-35 Beam breakup (BBU) current vs inverse length.

Figure 7-36 Logarithm of square root of induced beam breakup power (proportional to transverse beam amplitude) vs sector number, for a coasting beam with moderately strong focusing. The solid curve was found by simulating the experimental conditions (including focusing) with the computer program and agrees moderately well with the simple analytical formula [Eq. (7-126)].

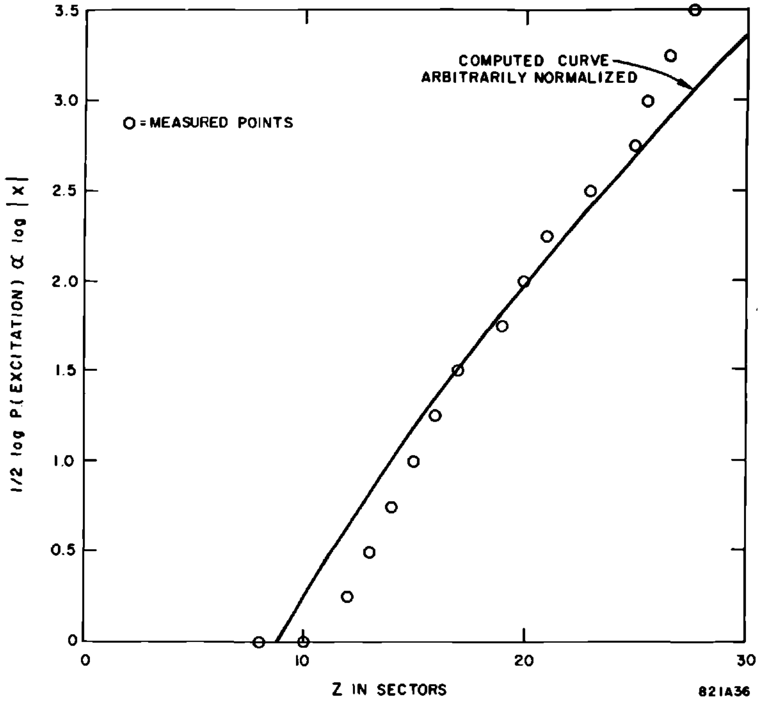

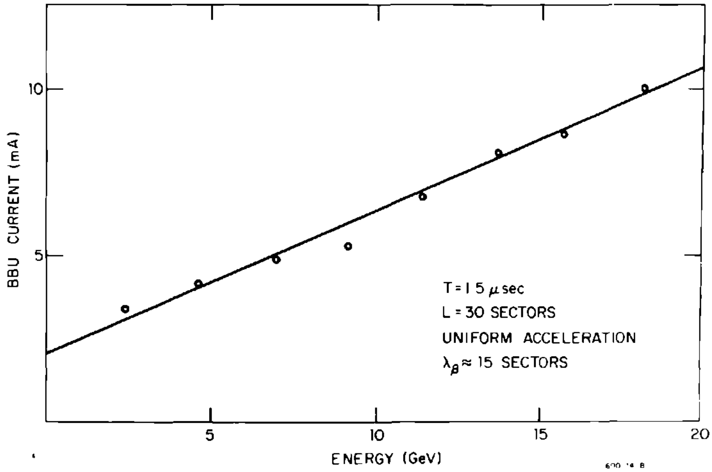

Figure 7-37 Beam breakup (BBU) current vs energy; weak focusing.

constant, then in the case of weak focusing, the variation of beam breakup threshold current as a function of energy gradient γ', should be linear as illustrated in Fig. 7-37. When stronger focusing is applied, Eq. (7-132) is no longer easy to solve, and one must resort to the computer calculations. Figure 7-38 shows a plot of beam breakup current as a function of betatron phase shift per sector. It is seen that when the theoretical data is normalized to one given experimental point, the agreement with experiment is excellent. For relatively weak focusing, the curves for different energy gradients are close to straight lines.

Further examination of the solution of Eq. (7-122) prompts one to examine the variation of the pulse length t as a function of the variable* $(tIz)^{1/3}$ evaluated at the beam breakup threshold. This is done in Fig. 7-39, and it is seen that for fixed focusing conditions, the curves are close to straight lines. This result is understandable because, neglecting focusing and the slowly varying coefficient $x_0(n, t)$ of Eq. (7-128), the slope of these curves should be a function of the loss term β, which is constant. A curve which is probably of greater interest to accelerator users who wish to know the maximum current obtainable as a function of pulse width is given in Fig. 7-40. Both experimental and computed total charge and peak beam current are plotted. For example, for a 50-nsec pulse, the maximum obtainable current below breakup is 250 mA peak.

Another way of verifying the laws of beam breakup is to measure indirectly the relative amplitude of the transverse modulation. A particular variable of interest is $(Iz)^{1/3}$. In Fig. 7-41, the experimental points for the ordinate x,

---

* The term (tIz) is analogous to the earlier term (tJg^2) of Eq. (7-130).

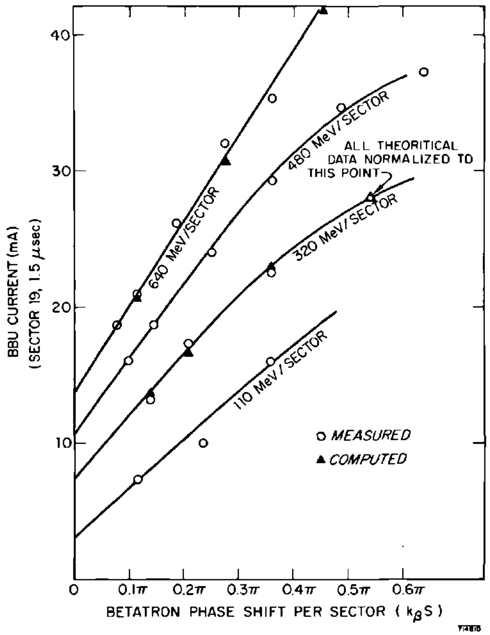

Figure 7-38 Beam breakup (BBU) current vs focusing strength expressed as betatron phase shift per sector.

Figure 7-39 Curves of $(tIz)^{1/3}$ vs t at beam breakup threshold.

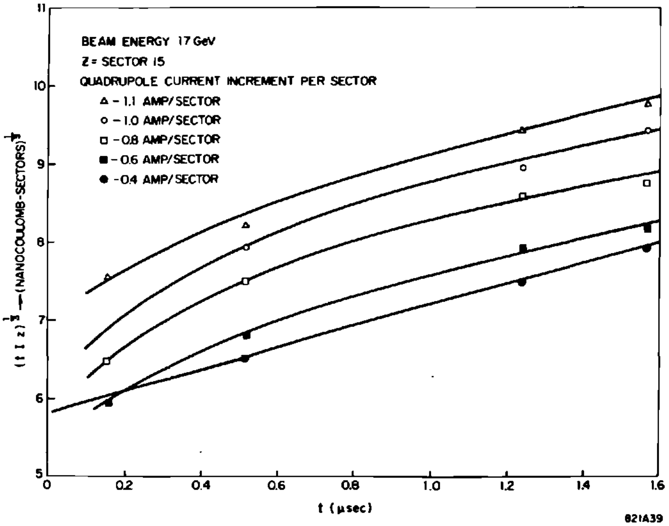

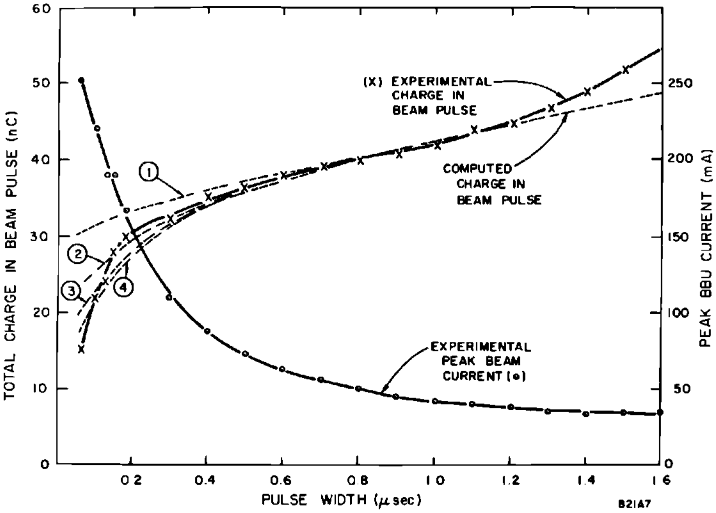

Figure 7-40 Experimental and computed beam breakup threshold as a function of pulse width. Curve 1 is computed, considering only the dominant (4139.64 MHz) resonant mode; curve 2 includes the effect of the first two modes (4139.64 and 4147.50 MHz); curve 3 includes the first three modes (4139.64, 4147.50, and 4154.00 MHz); and curve 4 includes the first four modes (4139.64 through 4160.5 MHz). It is assumed in the computation that $Q = 8000$ for all modes and that $R_\perp/Q = 400$ ohms/10-ft sections for the dominant mode. The values of $R_\perp/Q$ for the other modes are scaled according to the computed "effective lengths" given in Table 7-7. The failure of the computation to predict the time dependence in detail is probably due in part to the effects of transient beam loading and beam current pulse shape, which are not taken into account in the computation.

were obtained indirectly from the microwave power induced in one of the C-band cavities described in the previous paragraph. Computed values are also shown. Similarly, it has been possible to verify the law of beam breakup gain as illustrated in Fig. 7-42. The experimental points were obtained by successively disconnecting klystrons along the accelerator and measuring the amount of injected microwave power at 4140 MHz required barely to affect pulse shortening at a fixed point along the machine, namely the end of Sector 19. Again, it is seen that agreement with the computed power is quite good.

In the experiments discussed so far, the beam breakup starting conditions have not been considered. As mentioned earlier in this chapter, there appear to be several competing noise sources at the beginning of the accelerator which are illustrated in somewhat simplified form in Fig. 7-43. As this book is being written, experiments are still being conducted to discover if one of

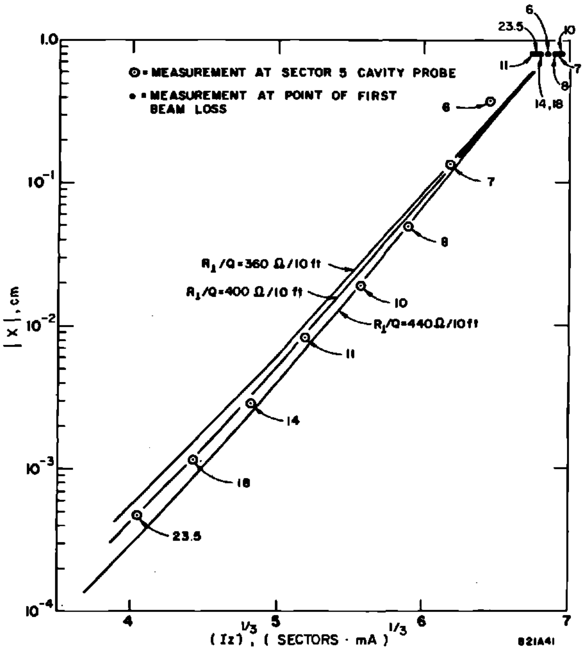

Figure 7-41 Transverse modulation in beam breakup as a function of $(Iz)^{1/3}$. The circled points were measured by means of a C-band cavity probe at the end of Sector 5; the solid points correspond to points along the machine at which breakup occurred at $\tau = 1.6$ μsec. The number attached to each point represents the sector at which breakup was first observed at a given beam current. The three curves for different values of $R_\perp/Q$ were calculated by the computer program. Comparison indicates an experimental value of $R_\perp/Q \approx 400 \pm 40$ ohms/10-ft accelerator section.

the sources is dominant. However, whether this is the case or not, it should be pointed out that it would take a significant reduction in noise power before the effect on the current threshold would become noticeable. Hence, letting the exponent given by Eq. (7-130) be called F, it can be shown that a reduction in noise power R in decibels corresponds to a relative increase in beam breakup threshold

$$T = \left(1 + \frac{R_{\text{dB}}}{8.68\,F}\right)^3 \tag{7-155}$$

Thus, for example, letting $R \approx 20$ dB and $F \approx 20$, it is seen that $T = 1.39$, giving less than 40% improvement in current.

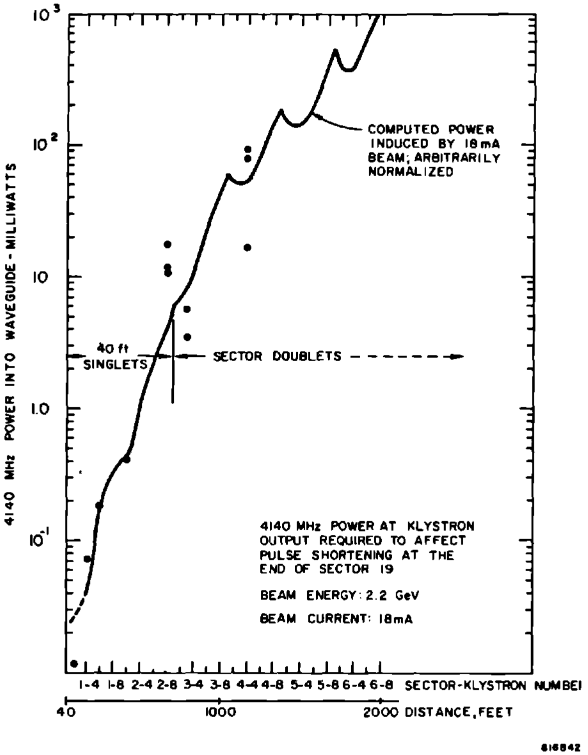

Figure 7-42 Beam breakup power vs distance.

Figure 7-43 Diagram of beam breakup, noise excitation mechanisms.

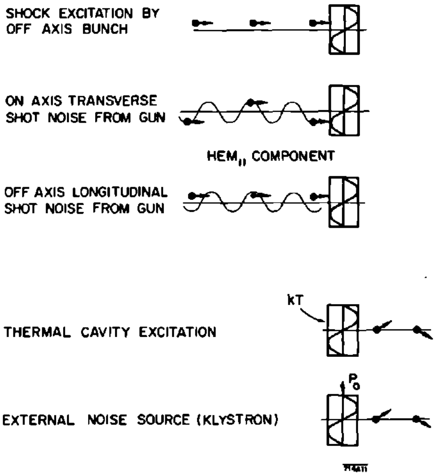

If shock excitation were the dominant driving term, the breakup threshold should be particularly sensitive to misalignment or mis-steering in the beginning of the accelerator. The threshold should also be strongly dependent on gun pulse shape. Finally, if x_0 in Eq. (7-128) is at least linear with J, the initial equivalent noise power would have to be quadratic with J. None of these assumptions has yet been clearly verified. On the other hand, if shot noise were the dominant source, the equivalent noise power would be linear with injected current. To test this idea, the following experiment was devised. At the 40-ft point, downstream of the injector, power P_0 at 4140 MHz was injected into the in-line C-band cavity mentioned earlier. At the end of Sector 5, roughly 1600 ft downstream, beam-induced power P_5 was extracted from a similar cavity. In the absence of any external excitation, this induced power P_5 was measured for a given beam current. Then, the injected power P_0 was increased until P_5 was roughly doubled. This measurement was repeated over a range of beam currents and at different times. Since that fraction of injected power P_0 which actually acts on the electron bunches must be of the same order of magnitude as the natural noise power carried by the beam, a relative, normalized measure of noise can be inferred. The results, which are plotted in Fig. 7-44, do not allow one to distinguish whether the normalized noise

Figure 7-44 Injected noise power equivalent to interval noise vs beam current.

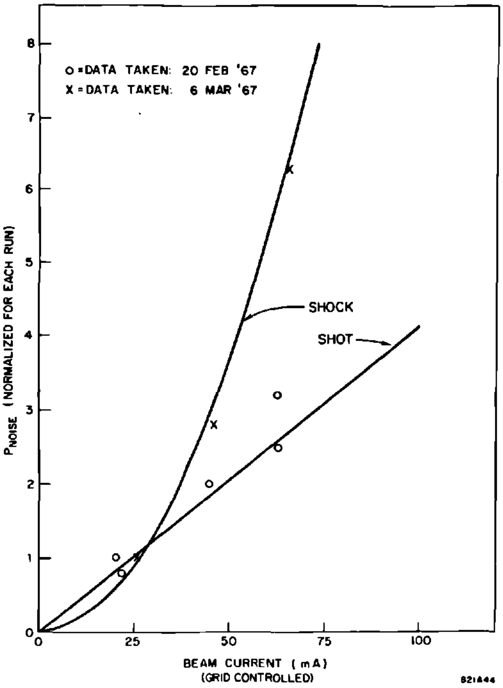

power is linear or quadratic with beam current. However, it can be concluded with fair certainty that this power is not entirely independent of current and, hence, that neither klystron noise nor cavity thermal excitation are the only sources of beam breakup noise. This conclusion is further confirmed by another experiment where the operation of the injector gun was taken from the temperature-limited region into the space-charge-limited region. As seen in Fig. 7-45, an improvement in beam breakup threshold of about 12% was found by increasing the cathode filament power from the temperature-limited to the space-charge-limited case. Unfortunately, under normal conditions, the gun is already operating under space-charge-limited conditions and straightforward improvements do not seem easily obtainable. Attempts are presently being made to design a cathode with a smaller radius which may, if shot noise is dominant, increase the present threshold. Finally, referring back to Fig. 7-42, it should be noticed that in the position where the first klystron was disconnected, an equivalent noise power of 12 μW was required. This value sets an upper limit to the allowable noise power from a high-power klystron. Above this value, klystron noise power would certainly become the dominant driving term for beam breakup. As this book is being written, it has not been possible to ascertain whether, indeed, the noise power from the klystrons is above or below this value. However, high-power filters capable of selectively attenuating signals at 4140 and 4428 MHz are being designed and will eventually be installed in the outputs of the early klystrons in the accelerator.

Figure 7-45 Beam breakup current vs cathode temperature (filament power).

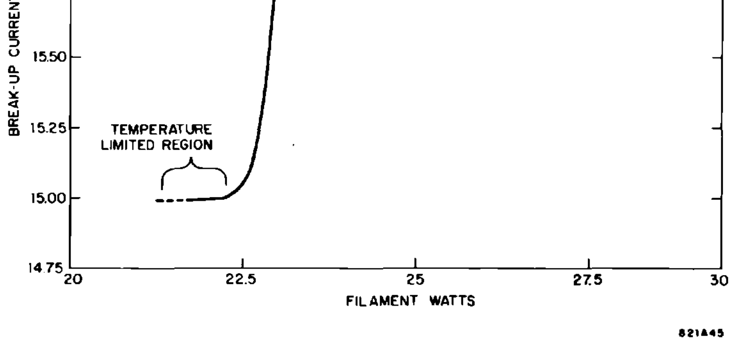

The magnetic fix program (RHH)

SUMMARY OF ALTERNATIVE BEAM BREAKUP REMEDIES. We list here some of the schemes which have been considered for suppression of the beam breakup at SLAC, and the reasons for rejecting most of them:

1. "*Landau damping*" *mechanisms.* Here we refer to any mechanism which destroys the coherence of the transverse beam oscillations. Two possibilities have been considered: (a) varying the focusing strength as a function of time during the RF pulse, e.g., by addition of ferrite quadrupoles modulated at a few MHz; and (b) nonlinear focusing, e.g., by addition of sextupole or octupole magnetic lenses. Computer investigation has indicated that both these schemes would be very ineffective under SLAC conditions. The key to this failure is the fact that the Landau mechanisms can be effective only if the instability grows adiabatically over many betatron wavelengths. In the SLAC transport system, the maximum number of betatron wavelengths in the entire machine is on the order of 10, whereas the e-folding distance for the beam breakup is on the order of a sector or less at onset of beam loss.
2. *RF cancellation.* The positive result of the RF cancellation experiment, described in an earlier section, proves that active RF suppression can work in principle. The expense and operational complexity appear to be prohibitive, however. We note in passing that true feedback, over a significant fraction of the machine, is ruled out (for low duty factor linacs) by the transit time problem.
3. *Starting-noise suppression.* Some effort has been devoted to the possibility of filtering the klystron output to remove frequency components in the 4140-MHz band. This is likely to give only marginal improvements, however, because both statistical beam fluctuations (shot noise) and shock excitation through misalignments appear to be of sufficient magnitude, even under best conditions of gun operation, steering, and alignment, to initiate the instability.
4. *RF "fixes" (passive).* Some possibilities are: (a) modification of the RF structure to decrease the coherence (effective length); (b) using several different accelerator modifications that resonate at different frequencies in the HEM_{11} band, so that the amplification in different sections is incoherent; (c) "Q-spoiling," i.e., coupling power selectively out of the HEM_{11} fields. The use of some sort of passive structure, which is excited by the transverse modulation and imparts a net demodulating impulse, also has been suggested. The most promising sort of passive RF fix for SLAC appears to be a selective detuning of the first cells of existing accelerator sections, over a finite fraction of the machine. These various approaches are under continuing study, but as of this writing (July 1967), no definite conclusions have been reached.

5. *Brute force* (*external focusing*). As has been seen in the previous sections, this approach gives a demonstrable improvement in the beam breakup threshold. Focusing has the additional advantage of nonselectively suppressing instabilities associated with other HEM_{11} resonances, higher transverse modes, and wake-field interaction.

THEORETICAL CONSIDERATION; CHOICE OF FOCUSING MODIFICATION. As was shown in a previous section, the improvement in beam breakup current threshold from external focusing is proportional (in the weak-focusing limit) to the quantity

$$\int \gamma^{1/2} k^2 \, dz$$

[see Eq. (7-134)] where k is the betatron wave number. In terms of the quadrupole strength, this integral is proportional to

$$\int \gamma^{-3/2} S^2 \, dz \tag{7-156}$$

where S is the quadrupole strength (gradient × length) referred to as Q in Section 7-2.

Thus, if the focusing is limited by the low-energy stop band, so that the quadrupole strength can be increased in proportion to beam energy, then the integrand goes as $\gamma^{1/2}$, and it is advantageous to increase the focusing at the high-energy end of the machine.

If, on the other hand, the limitation is imposed by available quadrupole strength so that $S \approx$ constant, then the integrand goes as $\gamma^{-3/2}$, and it is advantageous to concentrate the relatively weak quadrupoles at the low-energy end.

In order to take advantage of these considerations, a scheme was evolved for a more efficient arrangement of the original sector triplet quadrupoles.* In the first phase of the conversion, all the sector triplets were reconnected as doublets, using only the outer two, weaker, QA quadrupoles. The stronger QB quadrupoles were then removed from the drift sections and used to convert the doublets in the last two-thirds of the machine to QB doublets (this required changing some of the special positron triplets to doublets, also). Finally, the excess QA's which were thus released were then used to convert the first six sectors to the 40-ft alternating singlet system.

IMPROVEMENTS IN BEAM BREAKUP THRESHOLD; COMPUTED AND OBSERVED. Figures 7-46 and 7-47 illustrate computer results from which improvement factors were predicted, based on the best estimates of the deflecting mode parameters as of September 1966 and June 1967, respectively. In these figures, "Phase 0" refers to the system as originally designed, capable of being

---

* See Section 7-3 for detailed description of the existing transport system.

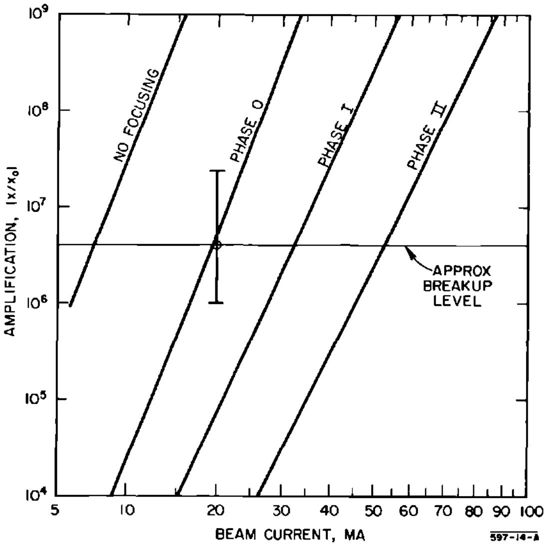

Figure 7-46 Beam breakup gain vs beam current for various earlier focusing schemes.

Figure 7-47 Similar to Fig. 7-46 but based on parameters as of June, 1967. Conditions: uniform acceleration to 18 GeV; $R_\perp/Q = 400$ ohms/10-ft section; $Q = 8000$; $\tau = 1.6$ μsec. "Phase I-A" differs from the "Phase I" of Fig. 7-46 in that the quadrupole singlets had been installed in Sectors 1 and 2. "Phase II-A" differs from the "Phase II" of Fig. 7-46 in that "Phase II-A" is based on the actual 40-ft spaced quadrupole singlets in Sectors 1 through 6, while "Phase II" was based on the assumption of 80-ft spaced doublets in Sectors 1 through 6. The circled points represent observed maximum currents under conditions similar to those for which the curves were computed.

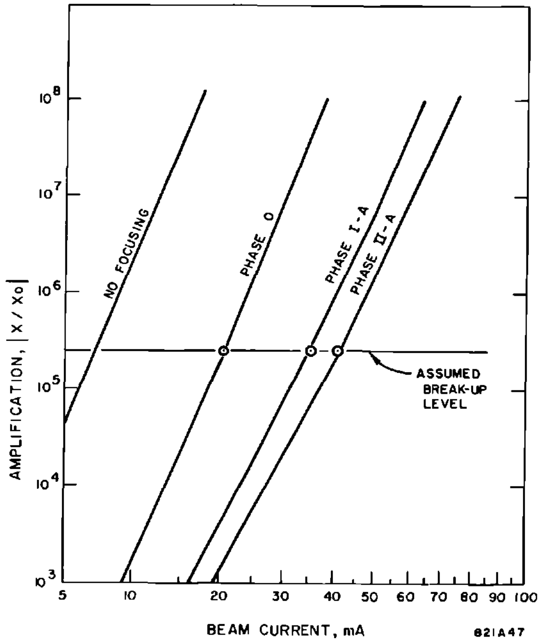

focused to optimum strength only up to Sector 7; "Phase I" refers to the first stage of quadrupole rearrangement in which the optimum focusing taper could be carried through most of the machine; and "Phase II" means the final stage in which additional lenses have been placed at closer spacing in the first six sectors.

(Actually, Phase I never existed; the alternating singlets were installed in the first two sectors before the doublet conversion was completed. This is taken into account in the "Phase I-A" line in Fig. 7-47.)

The experimental beam current thresholds, shown for comparison, are seen to be in reasonable agreement with the predictions.

References

1 M. S. Livingston and J. P. Blewett, *Particle Accelerators*, McGraw-Hill, New York, 1962.

2 W. K. H. Panofsky, "Note on Radial Beam Dynamics," Tech. Note No. SLAC-TN-63-89, Stanford Linear Accelerator Center, Stanford University, Stanford, California (1963).

3 R. H. Helm, "Notes on Electromagnetic Forces in Linear Accelerators," Tech. Note No. SLAC-TN-63-107, Stanford Linear Accelerator Center, Stanford University, Stanford, California (1963).

4 J. S. Bell, "Basic Algebra of the Strong Focusing System," Rept. No. AERE-T/R 1114, Atomic Energy Research Establishment, Harwell, Berkshire, England (January 1953).

5 A. P. Banford, *The Transport of Charged Particle Beams*, E. and F. N. Spon, London, 1966.

6 Klaus G. Steffen, *High Energy Beam Optics*, Wiley (Interscience), New York and London, 1965.

7 P. A. Sturrock, *Static and Dynamic Electron Optics*, Cambridge Univ. Press, London and New York, 1955.

8 E. D. Courant and H. S. Snyder, *Ann. Phys. N.Y.* 3, 1 (1958).

9 P. A. Sturrock, "A New Interpretation of the Adiabatic Approximation," Rept. No. AERE-TM-88, Atomic Energy Research Establishment, Harwell, Berkshire, England (September 1953).

10 R. H. Helm, "Discussion of Focusing Requirements for the Stanford Two-Mile Accelerator," Rept. No. SLAC-2, Stanford Linear Accelerator Center, Stanford University, Stanford, California (August 1962).

11 R. H. Helm, "Optical Properties of Quadrupole Multiplets for Sector Focusing in the Two-Mile Accelerator," Rept. No. SLAC-14, Stanford Linear Accelerator Center, Stanford University, Stanford, California (February 1963).

12 Albert Septier, "Strong Focusing Lenses," *Advan. Electron. Electron Phys.* **14**, 85.

13 A. Sessler, Lecture given at the Stanford Linear Accelerator Center, May 26, 1966 (unpublished).

14 R. H. Helm, "Misalignment and Quadrupole Error Effects in a Focusing System for the Two-Mile Accelerator," Rept. No. SLAC-11, Stanford Linear Accelerator Center, Stanford University, Stanford, California (January 1963).

15 R. H. Helm, "Misalignment and Quadrupole Error Problems Affecting the Choice of Multiplet Type for Sector Focusing of the Two-Mile Accelerator," Rept. No. SLAC-15, Stanford Linear Accelerator Center, Stanford University, Stanford, California (March 1963).

16 H. C. DeStaebler, Jr., "Scattering of Beam Electrons by the Residual Gas in the Accelerator," Rept. No. M-281, Stanford Linear Accelerator Center, Stanford University, Stanford, California (1961).

17 Bruno B. Rossi, *High Energy Particles*, Prentice-Hall, Englewood Cliffs, New Jersey, 1952, p. 65.

18 R. H. Helm, "A Note on Coupler Asymmetries in Long Linear Accelerators," Rept. No. M-167, Stanford Linear Accelerator Center, Stanford University, Stanford, California (March 1960).

19 R. H. Helm, "Effects of Stray Magnetic Fields and RF Coupler Asymmetry in the Two-Mile Accelerator with Sector Focusing," Rept. No. SLAC-20, Stanford Linear Accelerator Center, Stanford University, Stanford, California (October 1963).

20 W. K. H. Panofsky and W. A. Wentzel, *Rev. Sci. Instr.* **27**, 967 (1956).

21 W. B. Herrmannsfeldt and B. L. Salsburg, *Rev. Sci. Instr.* **35**, 906 (N) (1964).

22 W. B. Herrmannsfeldt, *IEEE Trans. Nucl. Sci. NS-12*, 929 (1965).

23 A. Sessler, "Instabilities of Relativistic Particle Beams," *Proc. 5th Intern. Conf. High-Energy Accelerators, Frascati, 1965* (C.N.E.N., Rome, 1966), pp. 319–329.

24 H. Hirakawa, *Japan J. Appl. Phys.* **3**, 27 (1964).

25 M. G. Kelliher and R. Beadle, *Nature* **187**, 1099 (1960).

26 T. R. Jarvis, G. Saxon, and M. C. Crowley-Milling, *Proc. Inst. Elec. Engrs. (London)* **112**, 1795 (1965).

27 P. B. Wilson, "A study of Beam Blow-up in Electron Linacs," Rept. No. HEPL-297 (Rev. A), High Energy Physics Laboratory, Stanford University, Stanford, California (June 1963).

28 H. Hahn, *Rev. Sci. Instr.* **34**, 1094 (1963).

29 W. K. H. Panofsky, "Transient Behavior of Beam Break-up," Tech. Note No. SLAC-TN-66-27, Stanford Linear Accelerator Center, Stanford University, Stanford, California (1966).

30 O. H. Altenmueller, R. R. Larsen, and G. A. Loew, "Investigations of Traveling-Wave Separators for the Stanford Two-Mile Linear Accelerator," Rept. No. SLAC-17, Stanford Linear Accelerator Center, Stanford University, Stanford, California (August 1963).

31 M. Bander, "Solution of the Beam Break-up Equation," Tech. Note No. SLAC-TN-66-28, Stanford Linear Accelerator Center, Stanford University, Stanford, California (June 1966).

32 G. V. Voskresenskii, V. I. Koroza, and Yu. N. Serebryakov, "Transverse Instabilities of a Beam in a Linear Accelerator prior to Increasing Injection

Current," *Uskoriteli* (Accelerators), Vol. 8, p. 136, Moscow Inst. Eng. Phys., Atomizdat, Moscow, 1966.

33 G. V. Voskresenskii *et al.*, *Soviet At. Energy* **20**, 3 (1966).

34 G. V. Voskresenskii, V. I. Koroza, and Yu. N. Serebryakov, "Toward the Investigation of the Radial Instability of a Beam in a Linear Electron Accelerator," *Uskoriteli* (Accelerators), Vol. 9, Moscow Inst. Eng. Phys. Atomizdat, Moscow, 1966.

35 R. H. Helm, "Computer Study of Wave Propagation, Beam Loading and Beam Blowupat the SLAC Accelerator," *Proc. 1966 Linear Accelerator Conf.*, Rept. No. LA-3609, Los Alamos Scientific Laboratory, Los Alamos, New Mexico (1966), p. 254.

36 O. H. Altenmueller *et al.*, "Beam Break-up Experiments at SLAC," *Proc. 1966 Linear Accelerator Conf.*, Rept. No. LA-3609, Los Alamos Scientific Laboratory, Los Alamos, New Mexico (1966), p. 267.

37 G. A. Loew, *IEEE Trans. Nucl. Sci. NS-14*, No. 3, p. 529 (June 1967).

38 V. A. Vishnyakov, A. I. Zykov, I. A. Grishaev, and L. A. Makhnenko, "Questions Concerning the Increase of the Limiting Current in Multisection Linear Accelerators," Rept. No. 309/VE-072, the Academy of Sciences, U.S.S.R. Physics and Engineering Institute, Kharkov (1967).

39 V. A. Vishnyakov, A. I. Zykov, I. A. Grishaev, N. I. Mocheshnikov, and G. D. Kramskoi, "An Investigation into the Effects of Current Pulse Shortening in Multisection Linear Accelerators," Rept. No. 276/VE-062, the Academy of Sciences, U.S.S.R. Physics and Engineering Institute, Kharkov (1966).

40 J. E. Bjorkholm and R. F. Hyneman, *IEEE Trans. Electron Devices ED-12*, p. 281 (1965).

41 H. S. Butler, S. K. Howry, and C. H. Moore, "Specifications for the Beam Transport Systems to End Stations A and B," Rept. No. SLAC-29, Stanford Linear Accelerator Center, Stanford University, Stanford, California (June 1964).

42 G. H. H. Chang, Pulse shortening in electron linear accelerators, M.Sc. Thesis, University of California, Berkeley, California (1964); see also E. L. Chu, "A Crude Estimate of the Starting Current for Linear Accelerator Beam Blow-up in the Presence of an Axial Magnetic Field," Tech. Note No. SLAC-TN-66-17, Stanford Linear Accelerator Center, Stanford University, Stanford, California (1966).

43 M. C. Crowley-Milling, "A 40-MeV Electron Accelerator for Germany," *AEI Eng.* **2**, No. 2 (1962).

44 R. L. Gluckstern and H. S. Butler, *IEEE Trans. Nucl. Sci. NS-12*, p. 607 (1965).

45 J. A. McIntyre, R. L. Kyhl, and W. K. H. Panofsky, "External Magnetic Focusing Devices for the Mark III Accelerator," Rept. No. ML-202, Microwave Laboratory, Stanford University, Stanford, California (July 1953).

8

INJECTOR

J. Berk, R. F. Koontz, and R. H. Miller, Editor

Many of the dominant features which determine the ultimate qualities of the electron beam emerging from a linear accelerator depend on the proper design and operation of the injector system. Thus, the ease with which the beam can be transported over long distances, the width of the energy spectrum, the precision with which the beam energy can be measured, and the precision with which scattering angles of particles can be determined in a physics experiment all depend on the phase space of the beam. The injector which was designed to help optimize these desirable requirements as the beam gets launched into the accelerator is the subject of this chapter.

8-1 Introduction and specifications (RHM)

The SLAC injector, is a short one-section linear accelerator consisting of the following components, shown schematically in Fig. 8-1:

1. A spherical triode gun and gun modulator.
2. A velocity modulating cavity or prebuncher.
3. A short bunching section with phase velocity equal to three-quarters the velocity of light.
4. A 10-ft long, constant-gradient, accelerator section with phase velocity equal to the velocity of light.
5. A focusing solenoid surrounding the buncher and the accelerator section.
6. Two 24-MW klystrons, one of which drives the injector. The other remains as a standby driver which can be switched onto the injector in less than a minute.
7. Steering dipoles and thin lenses.
8. RF deflection plates to add a 20–80 MHz structure to the beam.
9. Beam monitoring devices.

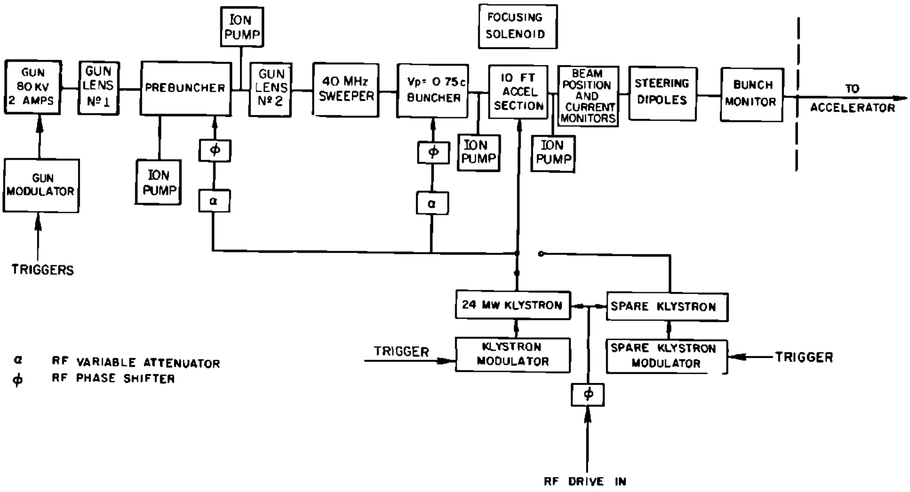

Figure 8-1 Main injector, schematic diagram.

A beam of 80-keV electrons from the gun is initially bunched by the resonant cavity prebuncher. It is further bunched and accelerated to 250 keV in a 10-cm long, travelling-wave buncher. The beam then enters the 10-ft long, accelerator section in which it is still further bunched into less than a 5° phase interval and accelerated to 40 MeV.

The most important objectives of the SLAC injector design were excellent bunching and beam optics, and maximum flexibility and reliability of operation. The bunch size is important since it sets the ultimate limit on the narrowness of the energy spectrum which can be achieved with the two-mile accelerator. A broad spectrum reduces the number of useful electrons for many experiments and also increases the radiation background against which these experiments must discriminate. The contribution of the bunch size to the energy spectrum spread of an otherwise perfect accelerator has been set at 0.1%. For optimum phasing of the injector relative to the rest of the accelerator, the relative energy spectrum is given by

$$\frac{\Delta E}{E} = 1 - \cos\frac{\Delta\phi}{2} \approx \frac{\Delta\phi^2}{8} \tag{8-1}$$

where $\Delta\phi$ is the bunch length in radians. For a 0.1% spectrum, a 5° bunch is required.

The ease with which a high-energy beam can be transported over long distances, the precision of beam energy measurements, and the accuracy to which scattering angles of particles can be determined all depend on the transverse phase volume occupied by the beam. Since the volume in phase cannot be reduced (except by throwing away part of the beam), these factors set restrictions on the injector emittance.

Flexible operation of the injector is mandatory for good utilization of the beam from the accelerator. A triode gun and its modulator permit the beam

Table 8-1 Injector specifications

Klystron peak power	14 MW
power to prebuncher	≈1 kW
power to buncher ($v_p = 0.75c$)	≈1 MW
power to accelerator	13 MW
Beam radius	0.5 cm
Radial phase space ($\pi r \times p_r$)	$\leq 5\pi \times 10^{-3}$ (MeV/c) (cm)
Bunch length (80% of accelerator current)	$\leq 5°$
Phase coherence of bunches	$\pm 5°$
Loaded beam energy	27.5 MeV (at 0.3 A)
Unloaded beam energy	38 MeV
Energy spectrum width	1%
Peak beam current	Programmable from 10^{-9} to 0.3 A
Allowable current variation	
within pulse	±0.5%
pulse-to-pulse	±0.75%
Current pulse length	Adjustable within a range of 0.04 to 2.1 μsec
Repetition rates	1–360 pulses/sec
Multiple beam capability	Three interlaced beams with independently adjustable pulse length and current

current and pulse length to be selected on a pulse-to-pulse basis from any of the three preset levels. Each of the three preset pulse lengths can be continuously varied from 0.04 to 2.1 μsec, and each current level can be varied from $\approx 10^{-9}$ to 0.3 A. In addition, the energy of the accelerator beam can be varied from pulse-to-pulse by switching klystrons beyond the injector in and out of time with the beam. These combined features permit several experiments to be carried on simultaneously. They also enable the operator to set up a new beam at a low repetition rate while current experiments are using most of the pulses.

These injector requirements are reflected in the specifications presented in Table 8-1. The klystron driving the injector is conservatively run at one-half to two-thirds full power to improve its life and reliability. To further improve reliability, a standby klystron and klystron modulator are installed. A waveguide "switch," consisting of two 3-dB hybrids and a hybrid phase shifter in the configuration commonly used for variable directional couplers, permits switching from one klystron to the other in less than 1 min.

8-2 Electron gun (JB, RHM)

General characteristics

The pulse characteristics of the accelerator beam are initially determined by the electron gun system. SLAC requires a range of pulse widths of from 0.04 to 2.1 μsec, rise and fall times of 0.2 μsec, and a range of beam current amplitude from 2 A, for use with beam choppers, down to the dark current threshold of the accelerator which is less than 1 nA. Any combination of these pulse widths and heights has to be available on a pulse-to-pulse basis at repetition rates from 1 to 360 pulses/sec.

Several common techniques are available to vary the amplitude of the emitted current. The simplest methods are (1) controlling the cathode temperature and (2) controlling the space-charge-limited current allowed to reach the anode by varying the anode voltage in a diode or the grid voltage in a triode. Here the "grid" can be either an intercepting wire mesh or a nonintercepting modulator anode. The temperature-limited emitter cannot be considered, because the thermal time constant of a practical cathode would not permit current changes to be made on a pulse-to-pulse basis. Varying the cathode-to-anode voltage cannot be used for current control, since a changing injection energy is not compatible with tight bunching. An advantage of the intercepting grid over the nonintercepting anode is that it is capable of a greater range of beam current control. The nonintercepting anode and the intercepting grid can also provide the on–off control of the beam pulse. Another common technique, transverse deflection of the beam across an aperture, can also be used to define the pulse duration. Such a system is used for subharmonic pulse selection as will be described later in this chapter. The intercepting grid has the disadvantage that it intercepts 10–20% of the cathode current and, consequently, has a heat dissipation problem. However, the mesh grid was chosen in preference to the nonintercepting anode because it was clear that an order of magnitude higher gain could be achieved with a mesh grid. Anticipation of a need for rise and fall times of the order of a nanosecond favored a high gain triode.

Computer design

The gun electrode configuration was developed using a computer program written by W. B. Herrmannsfeldt[1] to solve the Poisson equation. Using this program, the computer iteratively calculates electron trajectories through the gun in the presence of space charge. The program begins by solving the Laplace equation in the gun (i.e., it maps the field distribution with no space charge present). It then calculates the cathode emission densities and electron trajectories for that Laplace potential distribution. Then the charge distribution resulting from the trajectory calculation is inserted in the potential-solving subprogram, and the process is iterated. With suitable damping (accomplished by averaging cathode emission between successive trials) the calculation converges in about six iterations.

Gun electrode spacings were originally calculated using a spherical diode model. The electrode shapes were modified until the computed trajectories closely approximated those of the ideal spherical diode. Computed potentials along the beam edge agree with the analytic solution for a spherical diode to within 1% for over 90% of the distance from the cathode to the anode.

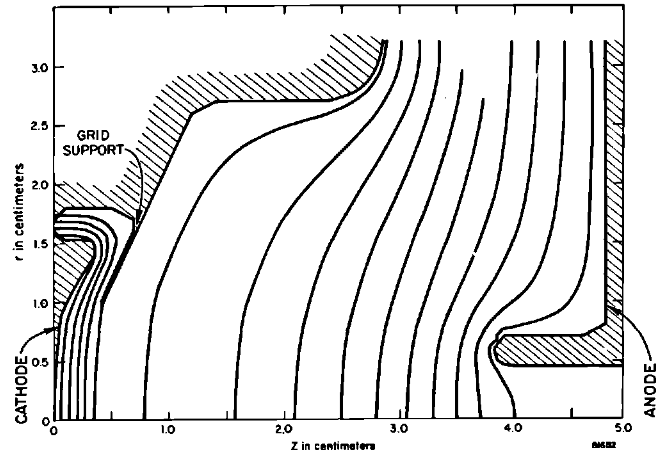

Figure 8-2 Computed equipotential plot.

The mesh grid was contoured to follow the equipotential surface which is nominally 1% of the cathode-to-anode voltage. This position allowed the highest gain consistent with a 2:1 ratio of mesh size to grid–cathode spacing. The closer the mesh grid is to the cathode, the more sensitive are the beam optics to perturbations in grid shape and spacing due to fabrication errors and thermal expansion.

The computer program treats the grid as an equipotential which does not intercept beam current. The computed equipotentials are shown in Fig. 8-2. The computed electron trajectories in the triode are shown in Fig. 8-3.

Phase space

The minimum emittance a gun can have is determined by the area and temperature of the cathode. The electrons emitted from the cathode

Figure 8-3 Computed electron trajectories.

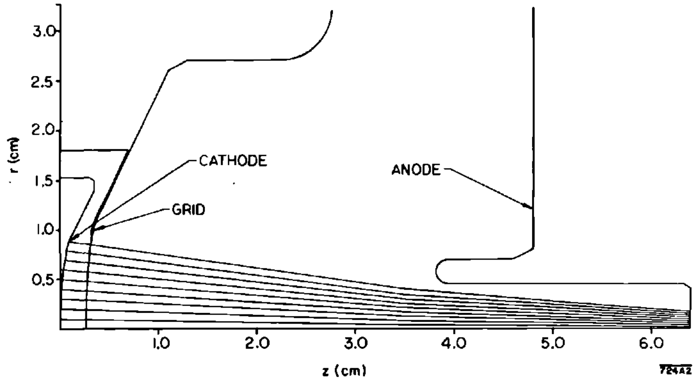

have a mean-square transverse velocity due to thermal energy given by

$$v_r^2 = \frac{kT}{m} \tag{8-2}$$

where k is Boltzmann's constant (1.38×10^{-16} erg/deg), T is the absolute temperature of the cathode, and m is the rest mass of the electron. So the emittance area due to thermals is

$$A_T = \pi r_c mc\left(\frac{kT}{mc^2}\right)^{1/2} \tag{8-3}$$

where r_c is the cathode radius.

For thermal electron emitters, kT varies from ≈ 0.1 eV for oxides to ≈ 0.2 eV for pure metals. The cathode radius in the SLAC gun is approximately 1 cm so the minimum emittance achievable is

$$2.3\pi \times 10^{-4}\,(\mathrm{MeV}/c)\,(\mathrm{cm})$$

The focusing elements of the gun also contribute to phase space. The computer program assumes that electrons have zero velocity at the cathode surface, so a measure of the focusing contribution can be obtained from the computed trajectories. The computer output includes the radius r and the slope dr/dz of each trajectory at the exit plane. These data are plotted in Fig. 8-4. In order to obtain a quantitative evaluation of various electrode configurations, it was necessary to calculate[2] an effective emittance area, for sets of discrete points, such as that shown in Fig. 8-4. The computed electron trajectories shown in Fig. 8-3 have an effective emittance of

$$5.7\pi \times 10^{-4}\,(\mathrm{MeV}/c)\,(\mathrm{cm})$$

Mechanical design

Figure 8-5 illustrates the physical configuration of the gun. On the right is the vacuum flange which is the mechanical and electrical interface with the

Figure 8-4 Computed gun emittance.

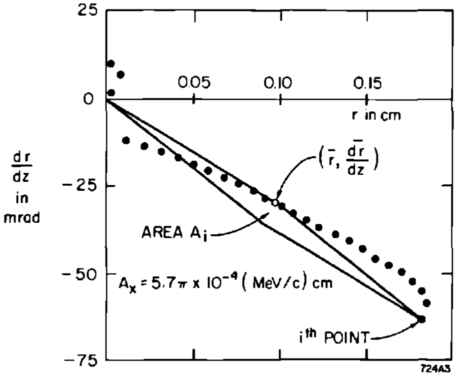

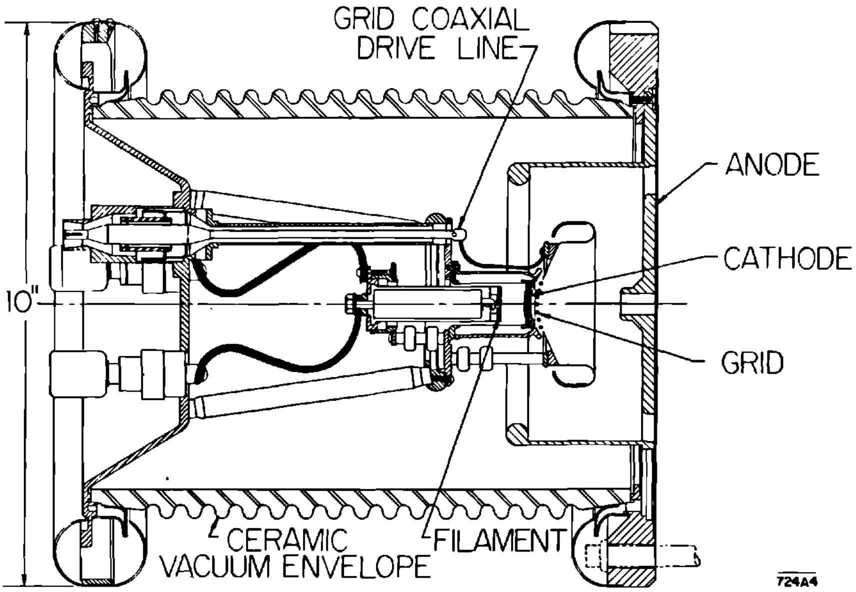

Figure 8-5 Electron gun assembly.

grounded accelerator structure. On this flange is mounted the anode, removal of which permits access to the inner gun. On the left is the rear deck which operates at cathode potential and is separated from the vacuum flange by the alumina insulator. With the corona shields shown the gun can be operated at 100-kV dc without arcing. Potential plotting on a conductive paper analog permitted adjustment of the corona shield on the anode flange to limit the maximum potential gradient in the ceramic to less than 890 volts/mm.

The rear deck is a recessed vacuum wall penetrated by the two filament feedthroughs and the grid, coaxial, drive line. The 50-ohm grid drive line has its outer conductor at cathode potential and its inner conductor connected to the grid structure. Inside the vacuum envelope the rear deck provides a structural support for the inner gun.

The inner gun can be replaced as a unit simply by connecting the two filament leads and the grid to the new unit. The mounting interface with the rear deck is the cathode deck on which the cathode assembly, the inner heat shields, and the beam-forming electrode are mounted. Two decks, each supported from the cathode deck with three insulated legs, support the grid structure and the bombarder.

The bombarder is a spiral "pancake" filament supported by a coaxial structure made from molybdenum and alumina. Two tantalum screws for clamping the filament legs allow convenient, but secure, filament installations. With suitable spacers installed at the rear of the bombarder the distance of the filament from the back of the cathode can be adjusted permitting either bombardment or radiant heating of the cathode.

The gun is designed to be baked as an assembly at temperatures in the range of 400 to 600°C for vacuum processing. Materials, therefore, are restricted to stainless steel, cupric nickel, oxygen-free high-conductivity copper, and refractory metals such as tungsten, tantalum, and molybdenum. Fixed joints are brazed wherever possible. Joints between components that can be reused several times are inert-gas welded or screwed together.

Mechanical thermal expansions are, of course, significant. The 3.95-cm distance between the cathode and the anode changes to 3.89 cm (1.5%) when the cathode temperature is raised from room temperature to its operating level. Temperature distributions on all components were estimated or measured. Room temperature dimensions were then calculated so that the computed electrode geometry would be assumed at the operating temperature.

GRID. The operating voltage chosen for the grid results in a grid–cathode spacing of 2.5 mm. The mesh is woven with 0.05-mm diameter, molybdenum wires at 1-mm spacing resulting in a ratio of interception area-to-total area of 10%. The mesh disk is stress relieved at 1000°C brightness for 1 min in a molybdenum jig, thereby forming it into a spherical cap. The individual wire ends are then spot-welded to the supporting 0.18-mm thick, molybdenum, focus electrode in an assembly jig. When the cathode is oxide coated and is operated at a temperature of 950°C brightness, the grid temperature measures about 410°C.

CATHODE. Considerations of the maximum beam pulse current requirement when operating with subharmonic pulse selection led to specifying a gun which would deliver 2 A at 80 kV, corresponding to a perveance of 0.0885×10^{-6} A/V$^{3/2}$. A cathode diameter of 1.90 cm and area of 2.84 cm^2 requires a maximum, homogeneous emission density of 0.775 A/cm^2 (assuming 10% grid capture). This emission level can, for a 2.5-μsec pulse and a maximum 0.001 duty factor, be obtained from several emitter materials.[3]

The technology of thin-film emitters, applied to a conducting base as a mixture of barium, strontium, and sometimes calcium carbonates and later thermally converted to oxides is well developed and reliable. The first SLAC guns used a carbonate emitter material sprayed on a nickel cathode base. Bases with either a fine nickel mesh or a fine nickel powder sintered to the surface provide adequate bonding interfaces for the carbonates.

The cumbersome and sometimes slow conversion processes required and the sensitivity of these emitters to poisoning in vacuums worse than 10^{-5} torr has led to a gun design which can accept a carburized, thoriated, tungsten cathode similar to that described by Haimson and Brodie.[4] The initial production of the 0.2-mm thick, carburized layer using colloidal graphite is as involved as the preparation of the oxide cathode. However, it can be done in a vacuum bell jar as this emitter can be exposed to air and reconverted (with a quick temperature flash) several times.

The carburized tungsten cathode has the disadvantage of requiring a higher operating temperature. Whereas the oxide cathode operates below about 900°C, the tungsten cathode requires up to 1600°C. The effect of the higher temperature on the heater power required can be seen by calculating the power radiated by the electron-emitting surfaces of the different cathodes. Assuming the cathodes face a cold wall with no additional heat shielding, the oxide cathode at 900°C radiates 10 W, whereas the tungsten cathode at 1600°C radiates 100 W.

HEATER. The oxide cathode temperature can easily be achieved using a radiant-heating spiral filament. Heaters with 0.6-cm spacing between center leg and outer leg, 9½ turns of 0.25-mm diameter tungsten (2% thoria) wire and 0.50-mm turn-to-turn spacing have a resistance of about 2.57 ohms at 1720°C. In the SLAC gun, they require about 40 W to maintain the oxide cathode at 780°C. Depending on the bombarder emitter efficiency, about 150 to 200 W is required to maintain the tungsten cathode at 1600°C. The same filament is used in carburized form as a bombarder diode emitter.

The filaments are wound two at a time, interleaved, and back-to-back, in a molybdenum jig. They are then stress relieved by heating to 1500°C for 2 min in a vacuum bell jar. For use as electron emitters, they are sprayed with colloidal graphite in an aqueous solution and then carburized by firing in vacuum to 1800°C for 30 sec.

In bombarder service these filaments are mounted 1 cm from the cathode back. With 1.4 kV applied between filament and cathode, a bombarder beam current of 150-mA dc provides 210 W of power with only 5 W of applied filament power. The filament operates at a temperature of 1450°C with a cathode temperature of 1600°C. Most of the power required to heat the bombarder filament is derived from back-heating from the hotter cathode. Temperature stability of the main cathode is controlled by regulating the bombarder beam current. This is achieved by operating the bombarder filament temperature limited and controlling the power used to heat it by means of a feedback circuit which senses the bombarder current.

Performance

BEAM OPTICS. The beam profiles shown in Fig. 8-6 were measured using a SLAC Model 4-1 gun with an oxide cathode and the SLAC beam analyzer. Cross sections of the beam current density were determined using a 0.25-mm diameter hole in front of a small Faraday cup. The radii at which the beam current density had dropped to 10% of its maximum value were then measured. Thus the profiles should contain about 90% of the beam current.

The profiles illustrate a beam minimum diameter of 0.76 cm at about 2.5 cm downbeam from the gun vacuum flange for the 0.10 microperveance ($K = 10^{-7}$ A/V$^{3/2}$) beam which is approximately the gun design perveance.

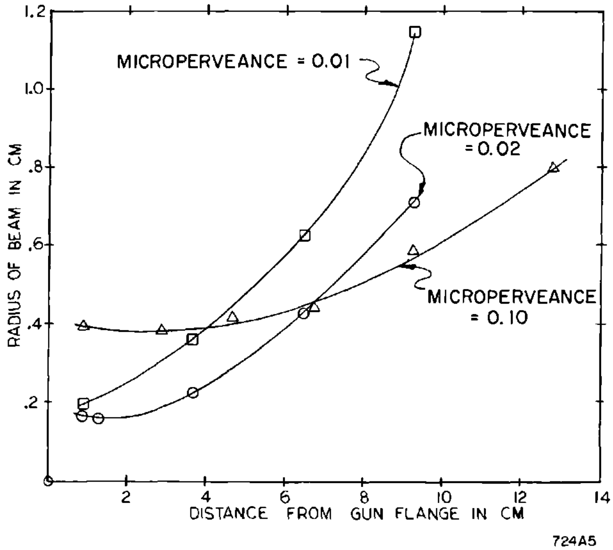

Figure 8-6 Measured beam profiles for three gun currents.

Space-charge spreading is an important effect at this perveance. The figure shows that the beam minimum moves back toward the cathode and becomes smaller with decreasing perveance.

ELECTRICAL CHARACTERISTICS. The transfer characteristics shown in Fig. 8-7 were taken using a SLAC Model 4-2 gun with an oxide cathode at a cathode–anode voltage of 40 kV. Therefore, the 1 % grid drive current of 1.2 A at 40 kV is a perveance of 0.15 microperveance. At 80 kV, this would give 3.4 A.

The cutoff characteristic shown in Fig. 8-8 was measured on a SLAC Model 4-2 gun with a tungsten cathode at a cathode–anode voltage of 70 kV. The cutoff value of 0.5-nA beam current was voltage dependent and may be due to grid emission. Use of the gun on the SLAC accelerator has indicated that the cutoff current is $\lesssim 0.1$ nA.

CATHODE LIFE. Although oxide cathodes have useful lives in excess of 10,000 hours in sealed tubes, their lifetimes in continuously pumped, linear accelerators have frequently been much less. For the last several years, however, since installation of a differential pumping system between the accelerator and the gun, the Mark III accelerator at Stanford University (1 GeV, 100 meters long) has been achieving oxide cathode gun lives of about 1 yr, or 6000 operating hours. No statistics are yet available for the SLAC gun. The first gun installed, which has an oxide cathode, is still in service and its performance is very encouraging. It now (July 1967) has been installed for 21 months and has been operated approximately 8000 hours.

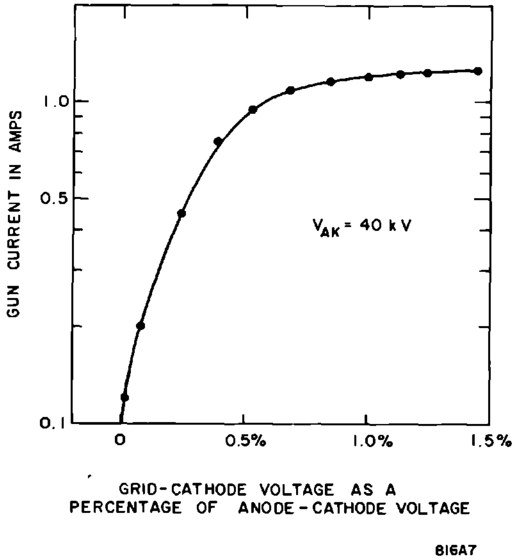

Figure 8-7 Gun transfer characteristic.

Figure 8-8 Gun cutoff characteristic.

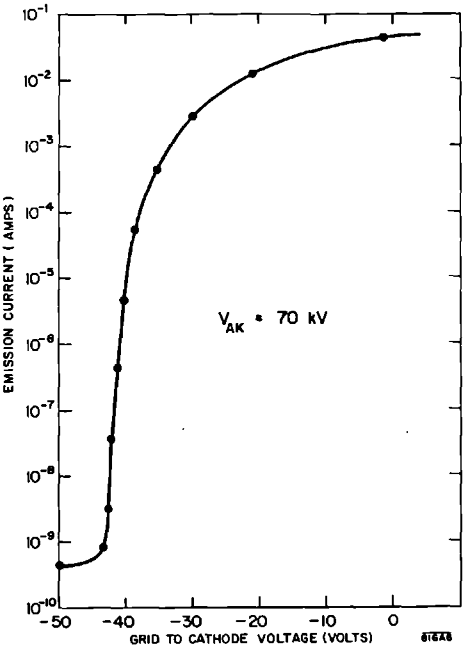

8-3 Multiple beam capability (RFK)

Beam parameters required

Early in the design of the accelerator, the problem of full beam utilization by the experimenters was considered. Some experiments such as bubble chamber studies cannot use the full repetition rate capability of the machine (360 pulses/sec), while other experiments require large amounts of integrated beam time, but are not concerned with a small percentage of missing pulses. Time is also required for setting up new beam configurations or experiments and this ideally should not represent wasted accelerator time. The outgrowth of these considerations was a beam switchyard concept with a capability of directing beams on a pulse-to-pulse basis to the several different target areas where the physics experiments are installed. Along with the capability of directing the beam to different experimental areas on a pulse-to-pulse basis came the requirement of programming the various beam parameters on a pulse-to-pulse basis. In addition to pulse repetition rate, the significant beam parameters from an experimenter's viewpoint are beam energy, beam spectrum, beam intensity, pulse duration, beam structure, and beam timing. Of these parameters, the injector influences or determines all but the beam energy. Beam energy depends on the number of klystrons used to accelerate the beam, and the machine control system makes provision for programming this number on a pulse-to-pulse basis. If the accelerator is properly phased, the beam spectrum is determined by the microwave properties of the injector structure. This is discussed in the following section. Of the remaining parameters, beam intensity and pulse duration are controlled by varying the output of the gun through control of the gun modulator. Beam structure refers to further intensity modulation within a single beam pulse. Various time-of-flight experiments require different structuring of the beam and, so far, two structuring systems have been built at SLAC and will be described below. Additional systems are being studied and designed and in time will become available for experimental use. The last parameter mentioned is beam timing. Control of beam timing and transmission of timing information to the experimenter is accomplished by the machine trigger system. The injector is required to maintain a stable relationship between machine trigger and the gun output.

The appropriate beam specifications associated with the injector gun and modulator system are given in Table 8-1. The gun has been discussed in detail in the preceding section.

The following gun characteristics are pertinent to the modulator design. The Pierce triode gun operates at a dc cathode potential in the range of 40 to 100 kV with 80 kV the nominal operating voltage. It requires about 700 volts, positive grid drive to achieve a 2-A peak current output. Grid current is about 10% of cathode current. Grid-to-cathode capacity is in the range of 20 to 25 pF, and the input structure looks like a 50-ohm transmission line terminated in this capacity. Virtually complete gun cutoff (less than 10^3 electrons/pulse) is achieved at a negative bias of 100 volts on the grid.

Gun modulator physical design

The SLAC accelerator is housed in a tunnel 25 ft below ground level. The moderate amounts of radiation present in the tunnel dictate that electronic equipment, especially that containing semiconductors, be installed if at all possible above ground in the klystron gallery and not in the tunnel. Since the gun must be in the tunnel, the choice had to be made whether to install all the gun pulser electronics in the gallery and face the problem of getting the pulser output to the gun by some transmission system or to mount portions of the pulser electronics in the tunnel close to the gun in a radiation environment and, therefore, inaccessible for maintenance during operation.

The first modulator system, a prototype, used at SLAC had a 300-ohm, distributed, amplifier pulser which was mounted in the tunnel. A large "box within a box" structure was built. The inner box contained instrument racks and was insulated from the outer box. The structure was installed in the tunnel directly behind the injector. An aperture in the outer box wall permitted the structure to be fitted over the gun so that the gun insulator spanned the gap between boxes. The inner box was floated at the dc cathode potential and was connected to the floating deck electronics in the gallery by a specially constructed 100-kV multiconductor cable which contained coaxial cables as well as individual wire pairs. The prototype modulator components previously mentioned were mounted in this box in close proximity to the gun and connected to electronics in the gallery through the multiconductor high-voltage cable. The present modulator has all of its electronics in the gallery as shown in Fig. 8-9, but it is anticipated the deck in the tunnel will be used later to mount fast grid driving pulsers associated with future beam structuring schemes. Recent developments in fast rise-time, high-voltage, dc,

Figure 8-9 Gun pulser block diagram.

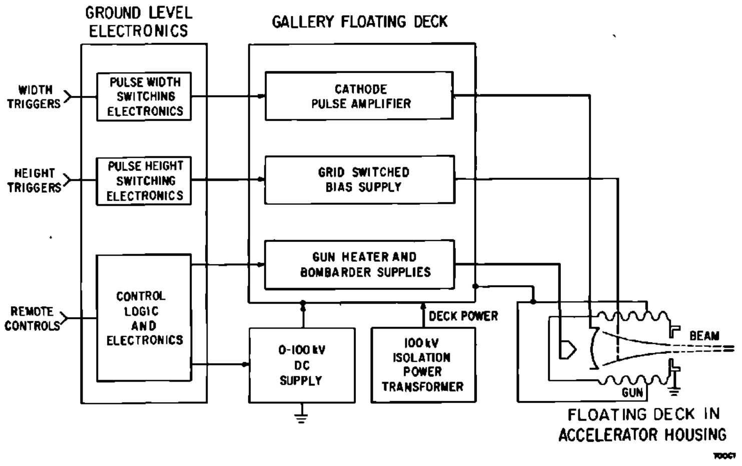

isolation transformers may even allow fast grid driving pulsers to be mounted in the gallery at ground level, in which case the large floating deck in the tunnel will be unnecessary.

Electrical requirements

BIAS PROGRAMMING. The present modulator is capable of selecting one of three remotely programmable grid bias settings in response to one of three pretriggers. The bias, in turn, controls the current output of the gun. A pretrigger is supplied to the gun modulator in advance of each machine pulse as required by the multiple beam pattern set up for the machine. If no trigger is received, or if two or more simultaneous triggers due to a programming error are received, the bias reverts to a high, but remotely controllable level which either cuts off the beam or reduces it to an extremely low intensity. The bias control channels are not part of either the personnel or machine protection interlock system, so this fourth channel feature guarantees an experimenter only that he will not receive a damagingly intense beam if a multiple trigger programming error or a missed trigger condition occurs. The fourth channel with its remote control capability also allows experiments which require very low electron densities (10^4–10^8 electrons/pulse) to be run while using the bias channel as a higher current "steering" channel. The low electron density beam is not seen by the machine beam-steering monitors, but an occasional pulse on the "steering" channel makes the orbit of the low-intensity beam visible on the monitors.

The switched grid bias electronics consists of a fast regulating, power supply and four, remotely controlled, reference potentiometers which can be switched into the power supply regulator circuits. These circuits and the receiving circuits of the RF pattern generator are mounted on the gallery

Figure 8-10 Bias control circuits.

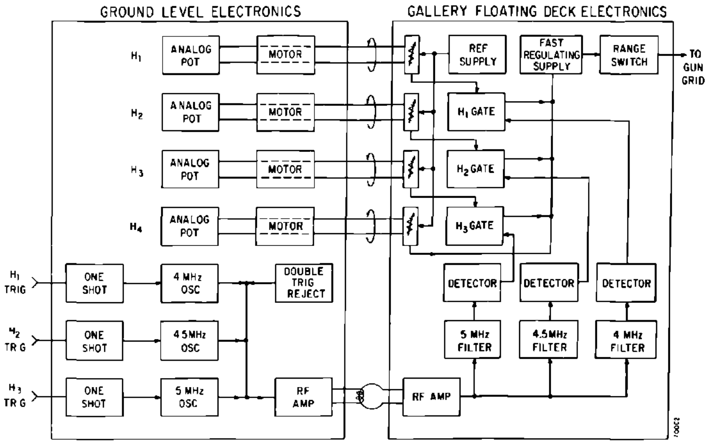

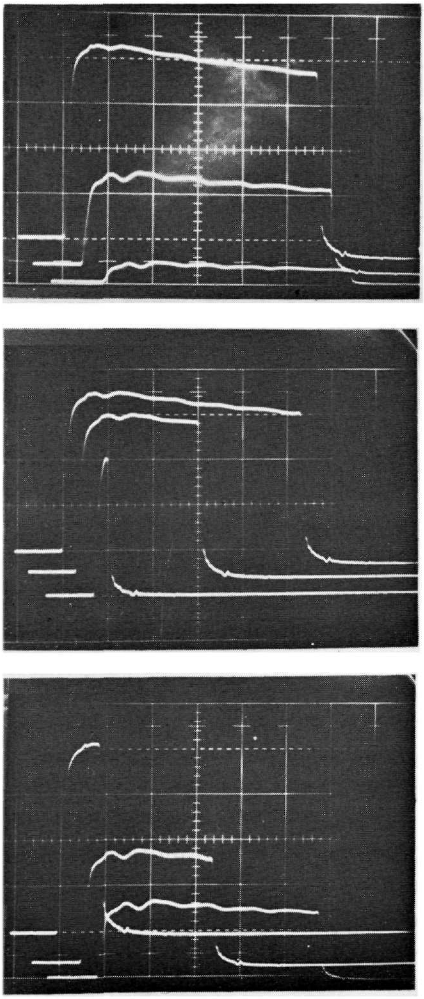

a) EXAMPLE OF GUN PULSE HEIGHTS SELECTABLE ON PULSE TO PULSE BASIS

b) EXAMPLE OF GUN PULSE WIDTHS SELECTABLE ON PULSE TO PULSE BASIS

c) EXAMPLE OF TYPICAL MIXED BEAM PROFILES

816A11

Figure 8-11 **Gun pulse profiles (sweep speed 0.25μsec/cm).**

floating deck. An RF pattern corresponding to the selected beam intensity profile is generated in ground level electronics and coupled to the floating deck via an isolation transformer. Figure 8-10 shows a block diagram of the complete bias control system. Figure 8-11a shows a picture of three, typical, gun pulse-height profiles which are selectable on a pulse-to-pulse basis in response to the appropriate input triggers.

PULSE WIDTH PROGRAMMING. Beam pulse width is also selectable from pulse-to-pulse. Separately triggered, low-level pulsers generate three pulses, remotely controllable in width, which can be selected as the machine beam pattern requires. These channels can be triggered in parallel, and, since each

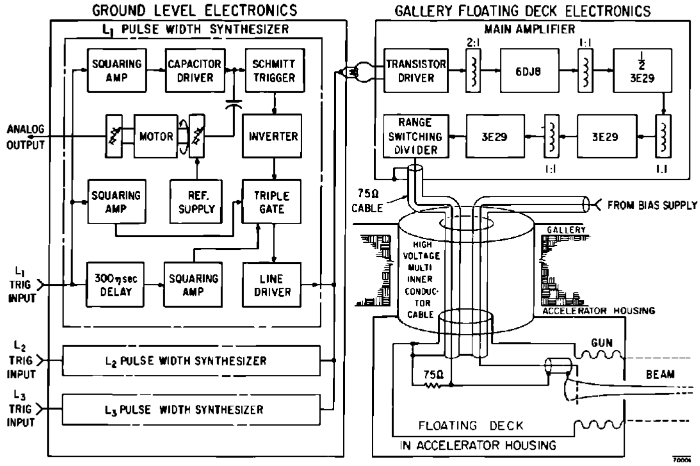

Figure 8-12 Gun pulser circuits.

has a separate timing control, three current pulses can be accelerated during one machine RF pulse. There is no ambiguity in driving all three of these pulsers during the same machine pulse either concurrently or sequentially, and this mode of operation has been used for some experiments. The pulse width circuits are part of the machine protection system so special effort is made to prevent triggering on noise or producing output pulses when there is no trigger. The outputs of all three pulse synthesizers are combined in a diode matrix to drive a high-voltage isolation transformer used to span the ground-to-floating deck gap.

On the gallery floating deck, the isolation transformer output is amplified and squared in a three-transistor driver whose output is a 30-volt pulse at a 50-ohm impedance level with rise and fall times of less than 20 nsec. This signal drives the four-tube saturated amplifier which produces an output of 800 volts into an impedance of 75 ohms. The four tubes of this amplifier all operate normally cut-off, and the last stages run from a separate power supply so that the tube plate has the correct dc reference level to drive the gun cathode directly. The polarity of the output is such that it directly drives the gun cathode. The block diagram of this system is shown in Fig. 8-12.

A set of typical pulse width profiles is shown in Fig. 8-11b. When the pulse-width and pulse-height programming capabilities are jointly used, gun beam profiles such as are shown in Fig. 8-11c are the result.

Beam structure equipment

Subharmonic beam sweeper systems are used to impress further structure on the electron beam pulse. The electron beam already has a fine structure corresponding to electron bunching at the machine frequency, 2856 MHz. For time-of-flight experiments, it is desirable to eliminate most of the electron bunches and accelerate an equivalent amount of charge in a train of widely separated bunches or bunch groups, spaced apart by a time long enough to avoid ambiguities and to permit measurement of the time of flight using time stretching techniques. To obtain single bunches, a deflector system phase-locked to the accelerator frequency is employed to eliminate all but the desired bunches. For bunch groups consisting of several bunches, phase-locking is not necessary and the experimenter can vary his group spacing at will by changing the deflector frequency.

Two early scheduled time-of-flight experiments generated requirements for a structured beam of single bunches periodic at 12.5 nsec and a structured beam of three bunches periodic in a range from 25 to 50 nsec. The 12.5-nsec period corresponds to a $\approx$40-MHz drive frequency and the 25–50 nsec periodicity corresponds to a variable frequency drive of from 10 to 20 MHz.

The single bunch system is shown in Fig. 8-13. It consists of a 50-kW RF amplifier and a resonant beam deflection structure close to the gun. The operating frequency of this system is, at the seventy-second subharmonic of the machine, 39.667 MHz. The master oscillator of the machine has an output at this frequency and this signal is used to drive the 50-kW peak pulsed RF amplifier. Pulsing is required since in multiple beam operation, the experiment requiring the structured beam may be assigned only a portion of the total machine pulses.

INITIAL BEAM DEFLECTOR. The first beam deflector is a pair of plates in the beam line following the gun and prebuncher. At this point the beam may not be sufficiently bunched for the plates totally to eliminate electrons in bunches

Figure 8-13 Subharmonic sweeper system.

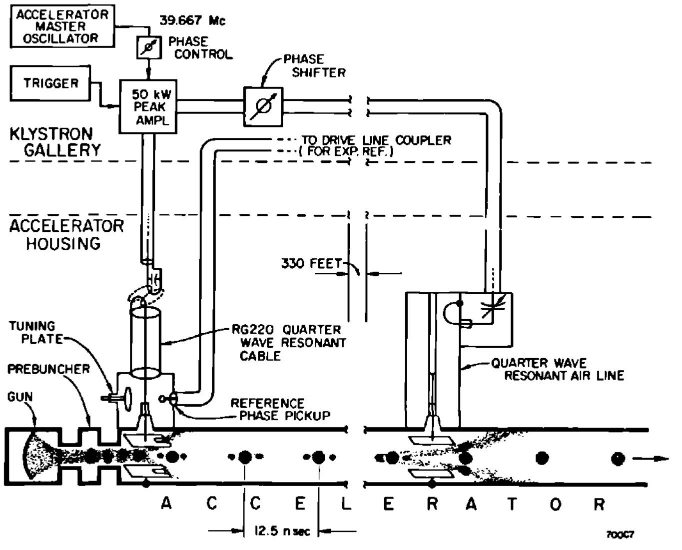

adjacent to the desired bunch, so provision has been made for later installation of a cleanup deflector downstream at the end of Sector 1. Early elimination of unwanted electron bunches prevents their loading the following buncher and accelerator structures. Consideration of these loading effects dictated the location of the first deflector. A quarter-wave section of RG 220 cable forms the deflector resonant circuit and steps the RF drive voltage up to 40 kV peak. This deflects all but the central bunch and vestiges of adjacent bunches into the walls of the deflector structure. The deflector phase is adjusted so that the central bunches occur at the zero crossings of the RF cycle. There are two of these per RF cycle, so only one out of every thirty-six bunches is transmitted.

A typical chopped beam is seen in Fig. 8-14a and b. This is the output of a single-turn toroid, 15 ft downstream of the first deflector as viewed on a 100-MHz bandwidth oscilloscope. If the beam is not precisely centered, and is improperly phased, electron bunches corresponding to alternate zero crossings will not have the same orbit and will suffer unequal transmission losses. This is observable in the photographs.

A capacitor divider samples the drive phase and transmits this information to the experimenter via the machine master drive line. The machine drive line frequency is 476 MHz and transmission of a 39.667-MHz signal does not

Figure 8-14 **A 39.667-MHz structured beam.**

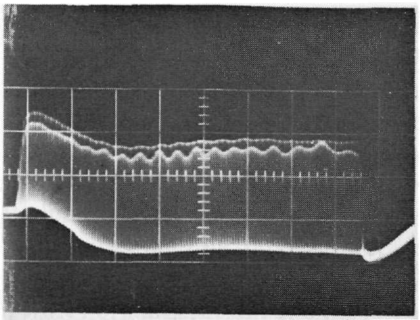

a) STRUCTURED BEAM AS SEEN ON TOROID AT 15 FOOT POINT

SWEEP SPEED
0.2 μ sec/cm

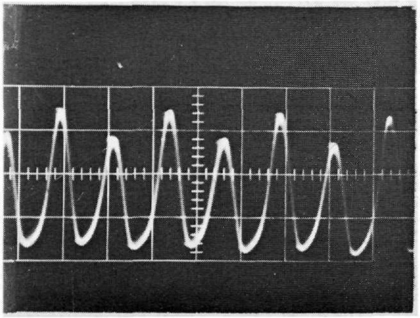

b) FINE DETAIL OF STRUCTURED BEAM (LIMITED BY OSCILLOSCOPE BANDWIDTH)

SWEEP SPEED
10 nanosec/cm

816A14

degrade its primary function of providing phase coherent drive for the machine sub-boosters, which, in turn, drive the 2856-MHz klystrons.

The resonant circuit for the 40-MHz system is not compatible with the 10–20 MHz chopping system at the present time. Work is proceeding on developing a broad-band voltage stepup transformer which will be useful over the range of 10 to 40 MHz.

SECOND BEAM DEFLECTOR. The second beam deflector, if installed, will be used only with the 40-MHz system and so does not have broad-banding problems. Its design will be similar to the first deflector, but the *Q* of its resonator will be higher since beam interception losses are not a factor. This deflector serves two purposes. It eliminates the residual adjacent bunches missed by the first deflector; it also eliminates all random electrons captured and accelerated in the injector and first 333 ft of the machine. Preliminary measurements of this "dark current" electron count indicate quantities of from 10^2 to 10^3 electrons/pulse. Eliminating these "dark current" electrons at the end of the first 333 ft of the machine effectively eliminates them from the experiment since all electrons captured downstream have insufficient energy to pass through the energy-analyzing slits of the machine.

8-4 Microwave system (RHM)

Buncher

Bunching in the SLAC injector occurs in three lumped components: the prebuncher, the 10-cm long, traveling-wave buncher, and the first 10 cm or so of the 10-ft accelerator section. A bunching system having several lumped components was chosen in preference to a tapered buncher because the former is easier to design, fabricate, and cold-test and because provision of independent phase and power controls to the components permits correction for design or fabrication errors. This flexibility also permits tuning to achieve optimum bunching despite malfunctioning equipment, such as a gun modulator or a gun that cannot achieve the design voltage, a low-power klystron, or stable but improper temperature control of the RF components.

The buncher design concept is one suggested by Lichtenberg.[5,6] It consists of matching the longitudinal phase space emittance of a prebuncher to the admittance of the accelerator with a quarter-wave transformer. Consider the following: (1) a prebuncher the emittance of which can be approximated by an erect* ellipse with a momentum extent of p_1 and phase extent ϕ_1; (2) an accelerator the admittance of which, for the desired final bunch, can be represented by an erect ellipse p_3 by ϕ_3; and (3) an intermediate traveling wave structure, or buncher, which can be characterized by the fact that a

* In this case, "erect" means that the principal axes of the ellipse are parallel with the p and ϕ axes, respectively.

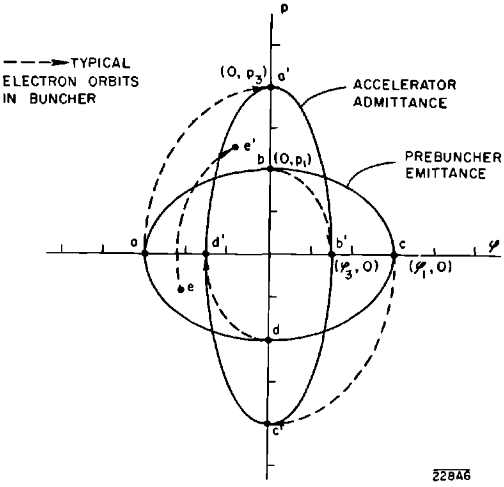

Figure 8-15 Buncher phase space.

particle performing phase oscillations with a maximum phase excursion of ϕ_2 will have a maximum momentum excursion p_2. The problem is to find the essential properties of the buncher so that it will transform the prebuncher emittance ellipse into the accelerator acceptance ellipse.

It has been shown by a number of authors[7,8] that an electron bound to a wave having a constant phase velocity less than the velocity of light oscillates in phase and also, of course, in momentum. For reasonably small oscillations and field strengths the equations can be linearized, and the oscillations in phase and in momentum are sinusoidal and in quadrature with each other. Consequently, in a plot of momentum against phase, an electron traces out a closed path which is an erect ellipse. Electrons with differing initial values trace out concentric, linearly scaled ellipses.

The function of the buncher is presented graphically on the momentum-phase plane in Fig. 8-15. The coordinate system chosen is one in which the electron in the middle of the bunch is at rest. The ellipse labeled "prebuncher emittance" with principal semiaxes p_1 and ϕ_1 encloses the initial conditions of all electrons considered to be within the bunch. The ellipse labeled "accelerator admittance" with semiaxes p_3 and ϕ_3 encloses the desired end points of all electrons in the bunch. The dashed lines represent electron orbits in the buncher which will map initial points *a*, *b*, *c*, *d*, and *e* within the prebuncher emittance into points *a'*, *b'*, *c'*, *d'*, and *e'* in the accelerator admittance. The orbits are segments of concentric similar ellipses. If p_2/ϕ_2 is the ratio of the semiaxes of the orbit ellipses within the buncher, then to map points *a* and *c* to *a'* and *c'*, p_2/ϕ_2 must satisfy the condition

$$p_3 = \frac{p_2}{\phi_2}\phi_1 \tag{8-4}$$

Since the transformation maps a point on the ϕ axis onto a point on the p axis, the buncher must be $(2n + 1)/4$ phase oscillations long. Similarly, in order to map b and d into b' and d', p_2/ϕ_2 must satisfy

$$\phi_3 = \frac{\phi_2}{p_2} p_1 \tag{8-5}$$

From Eqs. (8-4) and (8-5) the conditions for the mapping are found to be

$$p_3 \phi_3 = p_1 \phi_1 \tag{8-6}$$

and

$$\frac{p_2}{\phi_2} = \left(\frac{p_1 p_3}{\phi_1 \phi_3}\right)^{1/2} \tag{8-7}$$

From the linear nature of the mapping, it follows that the entire prebuncher emittance is mapped into the accelerator admittance. Equation (8-6) requires the areas of the two ellipses to be equal. Equation (8-7) is analogous to the condition on the impedance of a quarter-wave matching transformer in transmission line theory. The buncher orbit ellipticity p_2/ϕ_2 is the analog of the transformer impedance, whereas the ellipticity of prebuncher emittance p_1/ϕ_1 and the ellipticity of accelerator admittance p_3/ϕ_3 are analogs of the input and output impedances, respectively. The ratio p_2/ϕ_2 must be the geometric mean of p_1/ϕ_1 and p_3/ϕ_3.

In the buncher design for the present injector the buncher increases the momentum spread by a factor of about 2.5 while reducing the phase spread by a factor of about 2.5.

The phase velocity of the wave in the buncher is 0.75*c*, and the field strength is 25 kV/cm. The buncher is 10.5 cm long. In this distance the electrons oscillate a quarter of a cycle about the phase stable point. The mean velocity of the electrons entering the buncher is 0.50*c*. For electrons leaving the buncher, it is 0.75*c*. Thus the buncher accelerates the electrons as well as transforming the ratio of the momentum extent to the phase extent. The phase velocity in the 10-ft accelerator section is 1.00*c*, and the field strength is 120 kV/cm.

The precise electrical parameters for the prebuncher, buncher, and accelerator, and the resulting theoretical performance were determined by numerical integration of the following longitudinal and radial equations of motion[9] and by summing over space harmonics:

$$\frac{d\gamma}{dZ} = -\sum_n \alpha_n \left\{ J_0(k_{\rho n}\rho) \sin\left(\phi + \frac{2\pi n Z}{l}\right) - \frac{k_{zn}\rho p_\rho}{\beta\gamma} \cos\left(\phi + \frac{2\pi n Z}{l}\right)\right\} \tag{8-8}$$

$$\frac{d\phi}{dZ} = k_{z0} - \frac{2\pi}{\beta} \tag{8-9}$$

$$\frac{dp_\rho}{dZ} = \sum_n \frac{J_1(k_{\rho n}\rho)}{k_{\rho n}} \left[\alpha_n\left(\frac{k_{zn}}{\beta} - 2\pi\right)\cos\left(\phi + \frac{2\pi nZ}{l}\right) + \frac{1}{\beta}\frac{\partial\alpha_n}{\partial Z}\sin\left(\phi + \frac{2\pi nZ}{l}\right)\right] \tag{8-10}$$

$$\frac{d\rho}{dZ} = \frac{p_\rho}{\beta\gamma} \tag{8-11}$$

where

$Z = z/\lambda$

$\rho = r/\lambda$

$\beta = \dfrac{v}{c}$ for the electrons

$\gamma = \dfrac{1}{(1-\beta^2)^{1/2}}$ = total energy in rest mass units

p_ρ = radial momentum in units of mc

$\alpha = \dfrac{eE\lambda}{mc^2}$ = normalized electric field strength

n = space harmonic index and runs from $-\infty$ to $+\infty$ with 0 designating the fundamental space harmonic

k_{z0} = axial propagation constant of the fundamental space harmonic

$k_{zn} = k_{z0} + \dfrac{2\pi n}{l} = \dfrac{2\pi}{\lambda_g/\lambda}$

l = periodic length of the disk-loaded guide

$k_{\rho n} = [(2\pi)^2 - (k_{zn})^2]^{1/2}$ = radial propagation constant

These equations are appropriate for either traveling-wave or standing-wave structures with suitable choice of the periodic length l. The computer program written by W. Herrmannsfeldt using these equations was used to calculate electron orbits through the prebuncher, buncher, and accelerator section and intervening drift spaces. The values of the space harmonic amplitudes α_n were obtained from cold test measurements of disk-loaded structures which have been made at Stanford over a period of years.[10] Only three space harmonics were used in the injector calculations: $n = 0, -1, +1$.

Microwave components

The microwave power for the injector prebuncher, buncher, and accelerator comes from either of two standard SLAC 24-MW klystrons driven by standard modulators. The rectangular waveguide system consisting of a high-power switch for switching from one klystron to the other, directional couplers for splitting off power for the prebuncher and buncher, and a waveguide phase shifter and phase-compensated attenuator for the buncher, are described in Chapter 11. The prebuncher drive has a commercial, rotary vane attenuator. This type of attenuator was chosen because it introduces practically no phase shift as the attenuator is varied over a wide range. The prebuncher phase shifter is a Fox phase shifter of the type used in the RF drive system described in Chapter 9. The fact that the prebuncher and buncher attenuators do not introduce appreciable phase shifts greatly speeds the process of converging on optimum phase and power settings for the prebuncher and buncher.

PREBUNCHER. The prebuncher is a re-entrant resonant cavity machined from stainless steel. Stainless steel is used to lower the Q to approximately 500 so as to minimize the effects of temperature, mechanical distortions, and electron beam loading on the fields in the cavity. The peak gap voltage in the cavity is about 10 kV at the design drive power of 1 kW. The velocity modulation introduced by the prebuncher causes 70% of the electrons to be bunched into a 75° interval in the 30-cm drift space between the prebuncher and the buncher.

BUNCHER. The buncher and accelerator are copper disk-loaded structures fabricated by means of the brazing technique described in Chapter 6. The buncher is a traveling-wave structure only four cavities long, including the input and output couplers. It operates in the $2\pi/3$ mode (i.e., three cavities per guide wavelength) with a phase velocity of $0.75c$, so it has a length of one free space wavelength (10.5 cm). The buncher is brazed to the injector accelerator section to form a single assembly with a 1.9-cm thick, copper spacer between them. Each has a separate input waveguide, output waveguide, and load. The buncher and accelerator section have common water-cooling tubes brazed to the outer surface and they are supported in a common concentric stainless steel tube, which also supports the solenoid coils surrounding the buncher and the accelerator section. The buncher has a peak field of 25 kV/cm in the fundamental space harmonic at the design drive power of 0.5 MW. The desired electrons enter the buncher within a phase interval of 75° with an average velocity of $0.5c$ (79 keV). They leave the buncher within a phase interval of 30° and at a wave velocity of $0.75c$ (260 keV).

ACCELERATOR SECTION. The accelerator section in the injector is a standard constant-gradient section identical to all other sections except for external mechanical changes required to accommodate the buncher and the surrounding focusing coils. The 30° bunches are caused to enter the accelerator section around the phase stable field null, become bunched to less than a 5° width, and asympotically approach the crest of the wave as they are accelerated.

A simple analytic expression can be derived[7,9,11] for the asymptotic phase of an electron injected into a constant-gradient accelerator with the phase velocity equal to the velocity of light:

$$\cos \phi_\infty = \cos \phi_0 - \frac{2\pi}{\alpha} \left(\frac{1 - \beta_0}{1 + \beta_0} \right)^{1/2} \tag{8-12}$$

where ϕ_∞ is the asymptotic phase angle relative to the wave of an electron entering the accelerator with phase ϕ_0, and velocity $v_0 = c\beta_0$. The phase origin is taken at the field null, 90° ahead of the crest. The electric field parameter α is the energy in units of rest mass gained per free space wavelength λ by an electron on the crest of the wave:

$$\alpha = \frac{eE\lambda}{mc^2}$$

When $(2\pi/\alpha)[(1-\beta_0)/(1+\beta_0)]^{1/2} = 1$, an electron, entering the accelerator at $\phi_0 = 0$, asymptotically approaches the crest, $\phi_\infty = -\pi/2$. This condition produces optimum bunching of the electrons entering in the region of the null forward of the crest since

$$\left(\frac{d\phi_\infty}{d\phi_0}\right)_{\phi_0=0} = 0 \tag{8-13}$$

Expanding ϕ_∞ in a Taylor series about $\phi_0 = 0$, we get for this case

$$\phi_\infty \approx -\frac{\pi}{2} - \frac{\phi_0^2}{2} \tag{8-14}$$

For example, all electrons entering in the $\frac{1}{2}$ radian phase interval $-\frac{1}{4} \leq \phi_0 \leq +\frac{1}{4}$ have their asymptotic phase in the interval $-\pi/2 \geq \phi \geq -[(\pi/2) + (1/32)]$. Thus a phase compression factor of 16 is achieved in this example.

Bunch monitor

The function of the bunch monitor is to provide a signal which is simply related to bunch size and, hence, enables the operator to optimize bunching. Among the parameters that affect the energy spectrum of a long linear accelerator, one of the most basic is the bunch size. If the bunch length is θ radians and the phasing of the injector relative to the rest of the accelerator differs from the optimum by ϕ radians, the spectrum of the accelerator exclusive of other influences will be

$$\frac{\Delta E}{E} \approx \frac{1}{2}\left(\frac{\theta}{2} + \phi\right)^2 \qquad \text{for } \phi \leq \theta/2 \tag{8-15}$$

and

$$\frac{\Delta E}{E} \approx \theta\phi \qquad \text{for } \phi > \theta/2 \tag{8-16}$$

If $\theta = \phi = 5°$

$$\frac{\Delta E}{E} = 0.0085$$

Since the bunch forms in the first 10-ft accelerator section and remains substantially constant in size throughout the rest of the accelerator, it is meaningful to measure the bunch size at the output of the first section. This makes possible an evaluation of the bunching independent of the operation of the rest of the accelerator.

The bunch monitor consists of two RF induction cavities through which the beam passes, one resonant at 2856 MHz and one resonant at the fifth harmonic, 14280 MHz. The RF power from each cavity is detected with broadband detectors. The difference between the two detected signals is amplified and presented on an oscilloscope. It can be shown that this difference is proportional to the square of the bunch length.[12]

Measurement of bunching

The bunch monitor is intended to be an aid to optimizing bunching but is not intended to give an absolute measure of the bunch length. However, two absolute bunch length measurements have been made. The first, performed on a prototype of the injector, measured the bunch by sweeping the beam from the injector transversely with RF from the klystron which was feeding the injector.[13] Beyond the RF sweeper the electrons transverse position depends linearly on its phase relative to the RF at the sweeper. The bunch structure was measured by measuring the current through a slit as a function of the phase of the sweeper. The results shown in Fig. 8-16 indicate a bunch length of 2.7° full width at one-third maximum.

The second measurement of bunching was made after installation of the first sector of the accelerator. It was performed by measuring the increase in the width of the spectrum from the injector when a second 10-ft accelerator section was turned on 90° out of phase.[14] This measurement, which includes the effect of phase modulation present in the output of the injector 24-MW klystron relative to the phase modulation present in the output of the second 24-MW klystron, gave bunch widths ranging from 4° to 8° full width at half-maximum. The klystrons each have about 3° phase modulation.

Figure 8-16 Charge distribution in bunch.

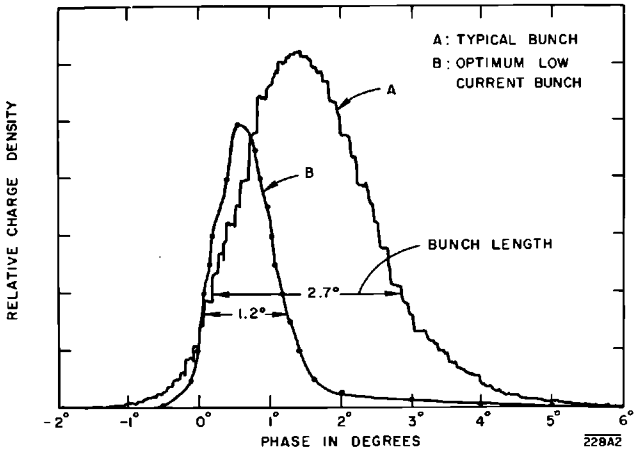

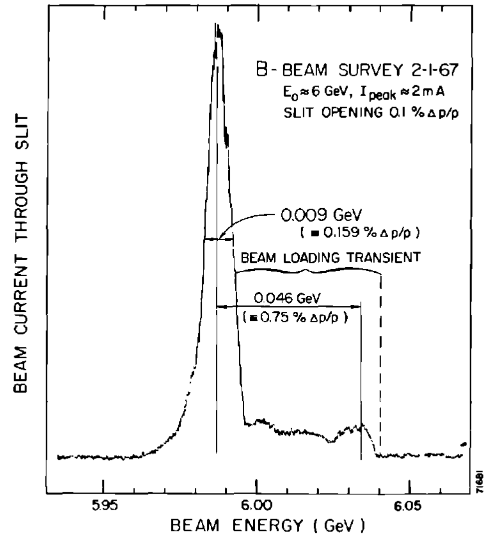

Figure 8-17 **Low-current energy spectrum at the end of the accelerator.**

Finally, the spectrum from the accelerator indicates the quality of the buncher. Figure 8-17 shows a typical spectrum for a low current beam immediately after phasing all klystrons and then adjusting the injector phase for best spectrum. This final adjustment of injector phase corrects for the average phase error resulting from small errors in the phasing of each klystron. Changing the injector phase by 1° or 2° from the optimum causes an obvious degradation of spectrum. The electrons on the high-energy side of the main peak are those accelerated during the beam-loading transient period. The energy of these electrons can be lowered by delaying the turn-on of an appropriate number of klystrons.

8-5 Beam transport (RHM)

Aside from the accelerating field, the electron beam from the gun is acted upon by its own space charge forces, by radial RF fields in the prebuncher, buncher, and accelerator, by the earth's magnetic field, and by stray magnetic fields caused by local currents and magnetic objects. For this reason it is necessary to incorporate steering, degaussing, and focusing devices into the design of the injector.

System description

In the region between the gun and the buncher, two magnetic thin lenses are used to focus the beam. The prebuncher gap is located at the beam waist (i.e., the point of minimum beam diameter) formed by the first lens. This location of the prebuncher minimizes the effects of the radial fields and the radial dependence of the longitudinal fields in the prebuncher. Use of a magnetic thin lens permits adjustment of the position of this first beam minimum and hence, permits relaxation of the gun fabrication tolerances and also allows for a variation of gun optics with a change in gun current. Since the lens is dc, whereas the gun current can be changed on a pulse-to-pulse basis, the lens must be set for the best compromise for the range of gun currents in use at a given time. Another magnetic thin lens is located 15 cm downstream from the prebuncher gap and produces a second waist at the entrance of the buncher.

Solenoid

At the second waist, a Brillouin focusing magnetic field is introduced. It is obtained by means of a focusing solenoid which encompasses the buncher and the first accelerator section. The confining field is terminated by shaping the field to produce a convergent magnetic lens at the end of the Brillouin field. By this method a slightly convergent beam can be emitted from the injector 10-ft accelerator section.

The solenoid is assembled from 34 3-in. thick, pancake coils. Each pancake consists of 540 turns of 2¾-in. wide, 0.0065-in. thick anodized aluminum foil interleaved with 0.00025-in. Mylar tape. This type of construction produces coils of which the mechanical and magnetic axes almost exactly coincide. The solenoid was assembled by sliding the pancakes onto the concentric stainless steel tube which supports the buncher and 3-meter accelerator section. The assembly is held together by four stringer bolts. Compression forces are applied through a stack of conical washers on each bolt. The pancakes are edge cooled by conduction through a thin layer of loaded epoxy to water-cooled plates between each pair.

At the beginning of the solenoid, where the electrons are not very energetic, the pancakes are individually driven by separate power supplies. In the down-beam half of the solenoid, the pancake coils are coupled together in sets of four, each set being energized by one power supply. This arrangement permits the optimum magnetic field configuration to be found experimentally.

Radial phase space

The dominant feature of the injector optics is that there are strong phase-dependent radial forces which act on the electrons, as seen in Eq. (8-10). Using an impulse approximation in which one assumes the radius ρ to be constant while the forces are applied, it is easy to integrate Eq. (8-10) through a prebuncher, buncher, or accelerator section.

For a prebuncher the answer is

$$\Delta p_\rho \approx \pi\rho\, \Delta\gamma\left(\frac{1-\beta^2}{\beta^2}\right) \cos \phi_m \tag{8-17}$$

where $\Delta\gamma$ is the peak cavity voltage in units m_0c^2/e, and ϕ_m is the phase when the electron reaches the middle of the cavity. For a short buncher with the phase velocity of the wave equal to $\beta_w c$, one obtains

$$\Delta p_\rho \approx \frac{\alpha\rho}{2}\frac{\beta_w(1-\beta^2)}{\beta(\beta_w-\beta)}(\sin\phi_0-\sin\phi_1) \tag{8-18}$$

where ϕ_0 and ϕ_1 are the phases of the electron entering and leaving the structure. Finally, for the capture region of an accelerator with $\beta_w = 1$ and initial electron velocity $\beta_0 c$, the radial impulse is

$$\Delta p_\rho \approx \frac{\alpha\rho_0}{2}\left\{1+\left(1+\frac{1}{\beta}\right)\sin\phi_0\right\} \tag{8-19}$$

For the accelerator section the radial impulse produced by the fringing fields at the output end is not included since the radius has probably changed and the electrons are tightly bunched into a short phase interval so the output has very little effect on the emittance. Since the radial impulses are phase dependent and the electrons enter the prebuncher, buncher, and accelerator with phase spreads of about 4, 1.2, and 0.5 rad, respectively, it is clear that these effects increase the area occupied by the beam in radial phase space. Furthermore, since the radial impulse depends linearly on the radius ρ, the radial emittance $\pi p_\rho \rho$ will vary as the square of the radius of the beam if these dominate. Because of the nonlinear property of the bunching action, electrons entering a bunching element at several different phases and undergoing differing radial forces leave the element at the same phase. As a result the increases in the radial momentum spread are not removed by subsequent RF elements but are cumulative.

Inserting a beam radius of 1 mm into Eqs. (8-17), (8-18), and (8-19) and using phase intervals of 4, 1.2, and 0.5 rad, respectively, for the prebuncher, buncher, and accelerator, one obtains the following values for the range of momentum impulse received:

prebuncher $(\Delta p_\rho) \approx 1 \times 10^{-3}$ MeV/c
buncher $(\Delta p_\rho) \approx 7 \times 10^{-3}$ MeV/c
accelerator $(\Delta p_\rho) \approx 8 \times 10^{-3}$ MeV/c

This produces an estimated injector emittance of the order of $1.6\pi \times 10^{-3}$ (MeV/c)(cm).

The radial emittance of the injector has been measured.[14] About 90% of the current from the injector is contained in an area of $4\pi \times 10^{-3}$ (MeV/c)(cm) in radial phase space for beam currents of 13.2 and 153 mA.

Acknowledgments

The authors wish to acknowledge the contributions of a number of persons who assisted in the design, fabrication, and installation of the injector. The klystrons, klystron modulators, microwave drive components, and 10-ft

disk-loaded waveguide were substantially identical to those used throughout the two-mile accelerator, and the responsible groups handled their procurement and installation in the injector. D. D. Tsang designed and supervised installation of most of the microwave system and special vacuum components. T. O. McKinney, J. Crew, W. P. Schulz, and J. Zink all made vital contributions to the gun development and testing program. R. A. Leeman supervised the installing of the electronics and cabling. E. F. Roskowski and R. R. Cochran did most of the mechanical engineering.

References

1 W. B. Herrmannsfeldt, "Poisson Equation Solving Program," Rept. No. SLAC-51, Stanford Linear Accelerator Center, Stanford University, Stanford, California (September 1965).

2 R. H. Miller, J. Berk, and T. O. McKinney, *IEEE Trans. Nucl. Sci. NS-14*, No. 3, p. 98 (June 1967).

3 G. A. Haas, "Thermionic Electron Sources," Rept. No. NRL-5657 (AD 266 039), Naval Research Laboratories, Washington, D.C. (October 1961), Fig. 1, p. 5.

4 J. Haimson and I. Brodie, *Nature* **199**, 795–797 (August 24, 1963).

5 A. J. Lichtenberg, Ph.D. Thesis, Oxford University, Oxford, England, 1961.

6 A. J. Lichtenberg, "The Application of Phase Space Concepts to the Design of an Electron Linac Buncher," Engineering Design Laboratory, Oxford University, Oxford, England (no date).

7 J. C. Slater, *Rev. Mod. Phys.* **20**, 473 (1948).

8 M. Chodorow *et al.*, *Rev. Sci. Instr.* **26**, 134 (1955).

9 E. L. Chu, "The Theory of Linear Electron Accelerators," Rept. No. ML-140, Microwave Laboratory, Stanford University, Stanford, California (May 1951).

10 W. J. Gallagher, "Measurement Techniques for Periodic Structures," Rept. No. ML-767, Microwave Laboratory, Stanford University, Stanford, California (November 1960), Appendix B, p. 55.

11 G. Dôme, "Electron Bunching by Uniform Sections of Disk-Loaded Waveguide. Part A: General Study," Rept. No. ML-780-A, Microwave Laboratory, Stanford University, Stanford, California (December 1960).

12 R. H. Miller, "Proposed Bunch Monitor," Tech. Note SLAC-TN-63-65, Stanford Linear Accelerator Center, Stanford University, Stanford, California (August 1963).

13 R. H. Miller, R. F. Koontz, and D. D. Tsang, "The SLAC Injector," *IEEE Trans. Nucl. Sci. NS-12* (No. 3), 804 (1965).

14 R. H. Miller, "Measurements of the SLAC Injector Emittance," *Proc. 1966 Linear Accelerator Conf.*, Rept. No. LA-3609, Los Alamos Scientific Laboratory, Los Alamos, New Mexico (1966), p. 65.